Transverse emittance measurement at REGAE via a solenoid scan

Diploma thesis
by
Max Hachmann

Institut Experimentalphysik
Universität Hamburg
1. November 2012

Gutachter: Prof. Dr. Florian Grüner
Zweitgutachter: Prof. Dr. Dwayne Miller

Abstract

The linear accelerator REGAE at DESY produces short and low charged electron bunches, on the one hand to resolve the excitation transitions of atoms temporally by pump probe electron diffraction experiments and on the other hand to investigate principal mechanisms of laser plasma acceleration. For both cases a high quality electron beam is required. A quantity to rate the beam quality is the beam emittance. In the course of this thesis transverse emittance measurements by a solenoid scan could be realized and beyond that an improved theoretical description of a solenoid was successful.
The foundation of emittance measurements are constituted by theoretical models which describe the envelope of a beam. Two different models were derived. The first is an often used model to determine the transverse beam emittance without considering space charge effects. More interesting and challenging was the development of an envelope model taking space charge effects into account. It is introduced and cross checked with measurements and simulations.

Zusammenfassung

Der linear Beschleuniger REGAE am DESY erzeugt kurze geladene Elektronenpakete mit einer geringen Ladung, um einerseits Anregungsübergänge von Atomen mit Hilfe von "pump-probe"Diffraktionsexperimenten zeitlich aufzulösen und andererseits grundsätzliche Mechanismen der Laser-Plasma-Beschleunigung zu erforschen. Für beide Fälle ist ein hochqualitativer Elektronenstrahl von Nöten. Eine Eigenschaft, um die Strahlqualität zu beurteilen, ist die Strahlemittanz. Im Zuge dieser Diplomarbeit konnten Messungen zur transversalen Emittanz durch Scannen eines Solenoiden realisiert werden und darüber hinaus war eine verbesserte theoretische Beschreibung eines Solenoiden erfolgreich.
Den Ursprung dieser Emittanzmessungen bilden theoretische Modelle, die die Einhüllende eines Strahls beschreiben. Zwei unterschiedliche Modelle wurden beschrieben. Das erste ist ein oft genutztes Modell, das Raumladungseffekte nicht berücksichtigt. Interessanter und herausfordernder war die Entwicklung eines Modells, welches Raumladungseffekte einbezieht. Es wird vorgestellt und mit Messungen und Simulationen abgeglichen.

Contents

List of Figures

List of Tables

1

Introduction

In the course of this diploma thesis theoretical and practical aspects of a transversal beam emittance measurement for low charged electron bunches at a linear accelerator, called REAGE[1], are presented. REGAE is a newly built machine at DESY[2]. The first beam has been produced in November 2011 since then the machine is being commissioned. Synchronization, overall stability as well as diagnostics development were central aspects of the first year at REGAE.
The emittance is a basic quantity to characterize the beam quality. Emittance models as well as the beam based alignment considerations introduced in this work represent basic procedures for high quality emittance measurements. First results are presented, a detailed characterization or optimization of the emittance is however beyond the scope of this thesis.
REGAE is designed to resolve the excitation transitions of atoms temporally by a pump probe electron diffraction experiment with a $\sim 10\,\mathrm{fs}$ electron bunch length [DHE+06]. This project is headed by Dwayne Miller.
In contrast to investigations with short photon pulses an electron bunch has a higher cross section related to solid state bodies and because of the smaller intensity this method is non-destructive for the target. The effort to reach such short and low charged electron bunches is indeed challenging but compared to photon sources (e.g. FEL[3]) a shorter machine with a lower mean beam energy is sufficient. The disadvantage is the electron-electron interactions which decrease beam

[1] **R**elativistic **E**lectron **G**un for **A**tomic **E**xploration
[2] **D**eutsches **E**lektronen-**Sy**nchrotron
[3] **F**ree **E**lectron **L**asers

qualities like the bunch length, beam size or the coherence length. Fig. 1.1 shows on the left-hand side one of the first diffraction patterns of a 50 nm thick gold target which was taken with a 4.1 MeV electron bunch at REGAE. The right-hand side shows the angular integrated intensity distribution of the pattern. In order to achieve high quality diffraction pattern there are different parameters which have to be controlled and improved. The low bunch charge is a very challenging subject for the beam diagnostics itself but in addition it is in the same order or smaller as the dark current which is produced by the gun cavity of REGAE. That is a reason why the gun gradient is limited so that the signal-to-noise-ratio is acceptable. Besides the short bunch length, which is required to reach a temporal resolution of atomic transition excitations (order of ~ 100 fs), the RF stability is a crucial parameter. A synchronization well below 100 fs is required for the electron bunch and the laser pulse at the target position in order to realize a pump probe experiment.
But the parameter which is directly connected to the emittance is the transverse coherence length L_c. It is proportional to the ratio of the beam size and the emittance:

$$L_c \sim \frac{\sigma_x}{\epsilon_{n,x}}$$

with σ_x as the transverse beam size and $\epsilon_{n,x}$ as the normalized transverse emittance. Generally the low charge has to be chosen to reduce space charge effects, which would decrease the emittance. But at the target position a sufficiently high electron density is needed to improve the contrast of the diffraction pattern. Consequentially the beam size has to be small so that the emittance has to be even smaller to reach a coherence length of 10-30 nm. The aimed transverse emittance is about 0.02 mm mrad. Magnitudes smaller than the emittance at a linear accelerator like FLASH[4].

In addition to the diffraction experiment another interesting experiment is placed at REGAE which requires comparable bunch parameters. It is one project of the LAOLA[5] collaboration, which attends to laser and particle driven plasma wakefield acceleration studies. This upcoming new accelerator scheme comes upon great conditions at REGAE to investigate the principal mechanisms of laser plasma acceleration. At REGAE it is intended to inject an electron bunch into a laser driven plasma wakefield. The injected electron bunches can be taken as probes of

[4] **F**ree Electron **Las**er in **H**amburg
[5] **La**boratory f**or** **L**aser- and beam-driven plasma **A**cceleration

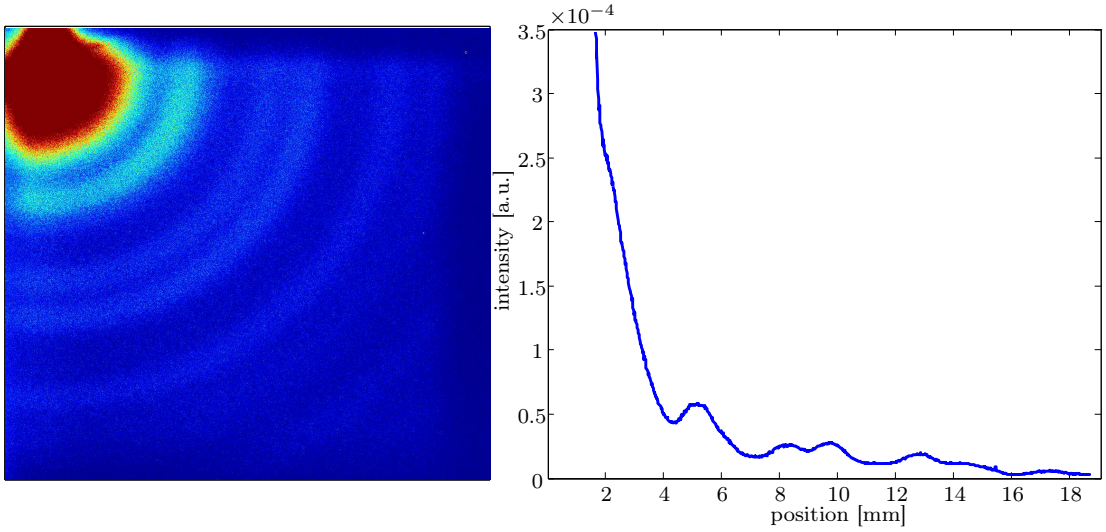

Figure 1.1: Electron diffraction pattern at REGAE and the relative angular integrated intensity distribution [figure by courtesy of S. Manz].

the plasma wakefield. The utilized high-power laser system necessitates a shot-to-shot beam diagnostic. At REGAE mostly multiple-shot diagnostics are in use. In order to compare the initial beam parameters with the final beam parameters an extremely stable incoming beam is required which parameters, among others the emittance, have to be well known.

A schematic plot of a quasi linear plasma wakefield is illustrated in fig. 1.2. Only a small area (shaded) can be applied for acceleration and focusing an electron bunch at the same time. This region is particularly interesting for a table-top FELs or staging schemes of plasma targets in order to reach higher energies for high energy particle physics.

To probe a plasma wakefield it is necessary to focus the bunch down to 5.0 μm transverse and 10 fs longitudinal which, at MeV energies, is only possible for a low charge beam like at REGAE. In addition the arrival time of the laser pulse and the electron bunch has to be synchronized to less than 20 fs. What is comparable with the requirements for the diffraction experiment.

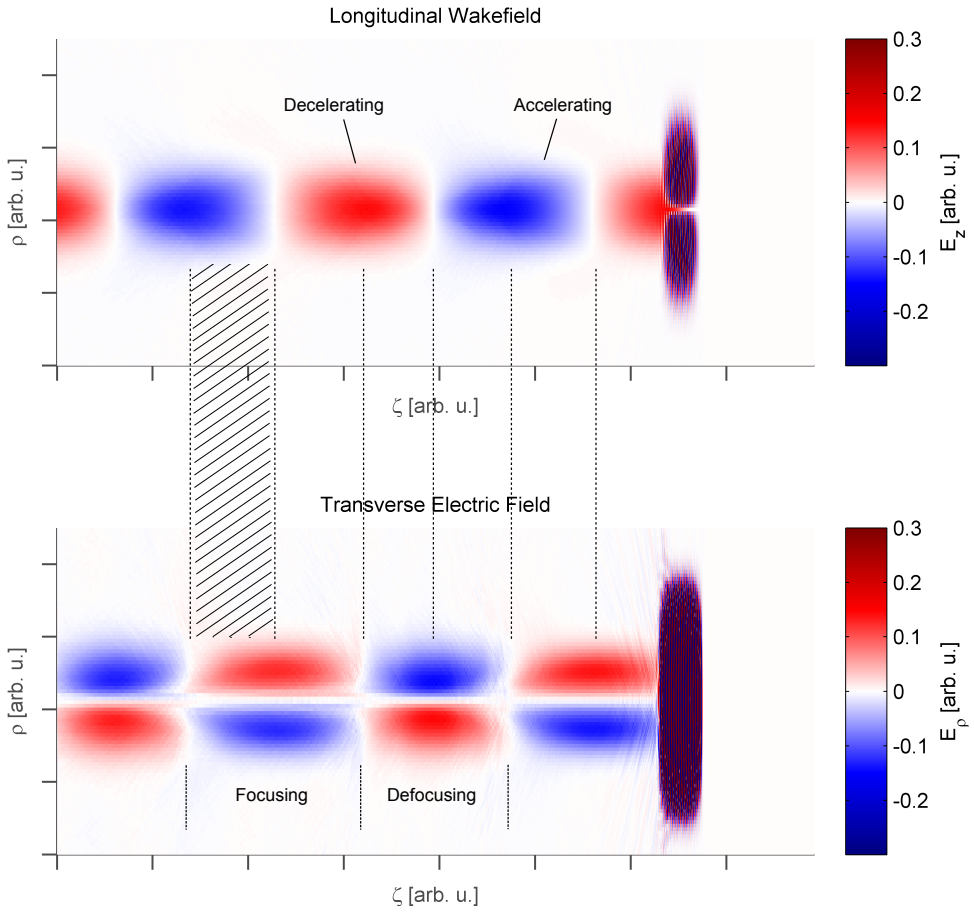

Figure 1.2: Simulation of a quasi linear plasma wakefield [figure by courtesy of B. Zeitler]. The regions (dashed) depicts different combination of acceleration/deceleration and focusing/defocusing phases.

2

Beam dynamics and optics

The topic of this chapter is the motion of charged particles and their interactions with external fields. I will introduce the phase space, the equation of motion for a linear accelerator and the resulting matrix formalism which allows us to describe beam dynamical elements like magnetic lenses. In particular I will explain the thin lens approximation of a solenoid and an analytical approximation for the equation of motion of a solenoid. The first is important for the emittance measurements and the second for the beam based alignment.

2.1 The phase space

The phase space combines the three dimensional position space (x, y, z) with the three dimensional momentum space (p_x, p_y, p_z). The positions as well as the velocities of all electrons describe the electron distribution physically complete in this 6-dimensional phase space. Focusing magnets or accelerating elements are able to shape the phase space distribution. But the taken volume V in phase space is a constant of time if one excludes interactions between electrons:

$$\frac{\mathrm{d}V}{\mathrm{d}t} = 0.$$

This phenomenon is described by Liouville's theorem [Lio38]. If correlations between the two dimensional phase spaces (x, p_x), (y, p_y) and (z, p_z) are excluded, this holds for each subspace in addition.
But how are these volumes accessible? A possibility to describe two dimensional

distributions is the second moment. This second moment, also called Root Mean Square (*rms*) value, is in case of a Gaussian distribution equal to its standard deviation σ. But in general it describes the averaged width of a distribution. Distributions described in this way can always be depicted as an ellipse in phase space [Flö11b, sec.1.2]. If non-linear forces are excluded, the area of the ellipse is a constant of time just as the mentioned phase space volume by Liouville. This behavior is shown in fig. 2.1 for a 2-dimensional phase space. The bunch keeps its elliptical shape and the phase space volume from the beginning up to the end.

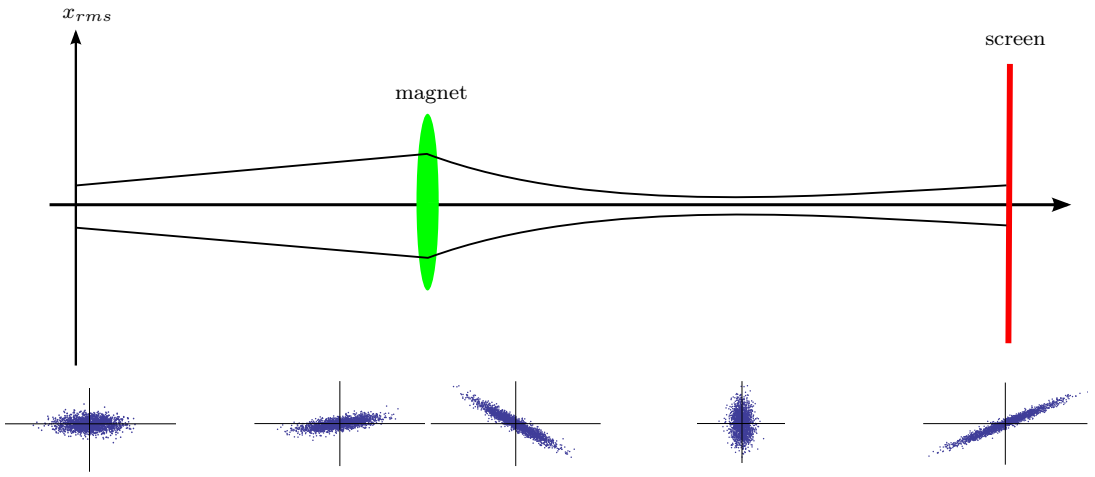

Figure 2.1: Development of the phase space distribution through a drift and a focusing element.

In the course of this thesis the spatial directions of a linear accelerator are defined as follows:

x :	horizontal transverse
y :	vertical transverse
z :	acceleration direction

In the following the horizontal direction is considered. Equivalent relations are valid for the vertical and the longitudinal direction. The constant area of an ellipse suggests to introduce a new quantity - the normalized rms emittance $\epsilon_{n,x}$. It can be calculated for an ellipse with its principal axes parallel to the coordinate axes as

$$\epsilon_{n,x} = \frac{1}{m_0\, c} \sqrt{\langle x^2 \rangle \langle {p_x}^2 \rangle} \tag{2.1}$$

with the rest mass m_0, the speed of light c and

$$\begin{aligned} \langle x^2 \rangle &= \frac{\sum_{i=1}^{N} x^2}{N} - \left(\frac{\sum_{i=1}^{N} x}{N} \right)^2 \\ \langle {p_x}^2 \rangle &= \frac{\sum_{i=1}^{N} {p_x}^2}{N} - \left(\frac{\sum_{i=1}^{N} p_x}{N} \right)^2 \end{aligned} \tag{2.2}$$

for a discrete distribution or with

$$\begin{aligned} \langle x^2 \rangle &= \frac{\int x^2 \varrho(x, p_x) \mathrm{d}x \mathrm{d}p_x}{\int \varrho(x, p_x) \mathrm{d}x \mathrm{d}p_x} - \left(\frac{\int x \varrho(x, p_x) \mathrm{d}x \mathrm{d}p_x}{\int \varrho(x, p_x) \mathrm{d}x \mathrm{d}p_x} \right)^2 \\ \langle {p_x}^2 \rangle &= \frac{\int {p_x}^2 \varrho(x, p_x) \mathrm{d}x \mathrm{d}p_x}{\int \varrho(x, p_x) \mathrm{d}x \mathrm{d}p_x} - \left(\frac{\int p_x \varrho(x, p_x) \mathrm{d}x \mathrm{d}p_x}{\int \varrho(x, p_x) \mathrm{d}x \mathrm{d}p_x} \right)^2 \end{aligned} \tag{2.3}$$

for a continuous distribution $\varrho(x, y)$. 2.2 as well as 2.3 are the definitions of the second central moments or rms values. If the center of a distribution does not coincide with the center of the coordinates system, the second sum or integral on the right-hand side corrects this offset. In the following it is assumed that the distribution is centered, i.e. $\bar{x} = \bar{p}_x = 0$. This is possible without loss of generality. As mentioned before the emittance is a constant of time in the two dimensional phase space as long as no correlations between the different subspaces exist. An example of correlated subspaces follows in section 6.3.2.
In case of a tilted phase space ellipse the rms values are not identical with the principal axes of the ellipse. They are the maximum elongation of the ellipse in Cartesian coordinates (see fig. 2.2) thus 2.1 cannot be applied directly. There are two ways to obtain the real emittance. Shearing the phase space ellipse conserves the area of it but changes the length of the principal axes while rotating the whole phase space ellipse conserves both values. The conservation of the length of the principal axes is important for future calculations of rms beam sizes and therefore this method is chosen here.

The second moment of an arbitrary distribution in a phase space like (x, p_x) can be described by the distance d_i of every particle to a rotated axis $\tilde{x}$ [Buo90], see fig. 2.2. The rotation angle will be denoted as θ. Then d_i is defined as

$$d_i = |p_{x,i} \cos\theta - x_i \sin\theta| \tag{2.4}$$

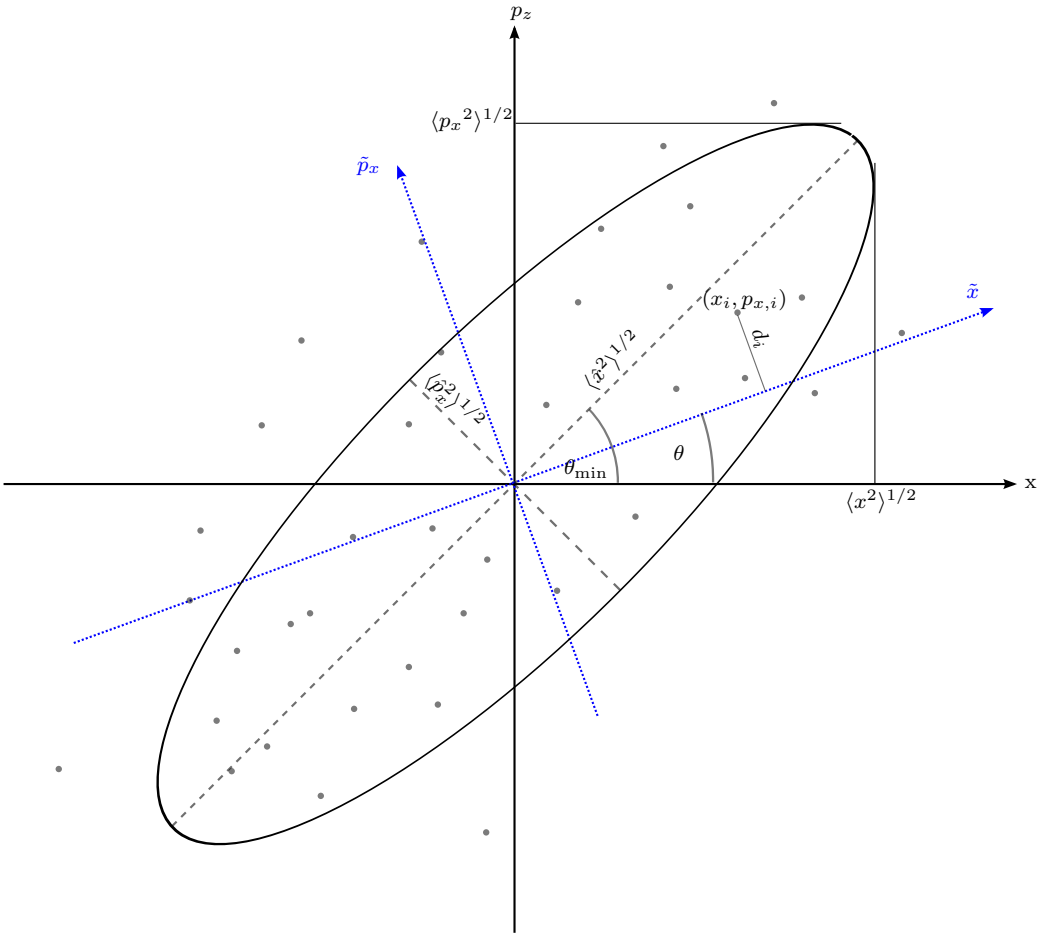

Figure 2.2: Phase space ellipse

and the mean square distance writes as

$$\begin{aligned}\langle d^2 \rangle &= \frac{\sum_{i=1}^{N} {d_i}^2}{N} \\ &= \cos\theta^2 \frac{\sum_{i=1}^{N} {p_{x,i}}^2}{N} + \sin\theta^2 \frac{\sum_{i=1}^{N} {x_i}^2}{N} - 2\,\sin\theta\,\cos\theta \frac{\sum_{i=1}^{N} p_{x,i}\,x_i}{N} \\ &= \langle {p_x}^2 \rangle\,\cos^2\theta + \langle x^2 \rangle\,\sin^2\theta - 2\langle x\,p_x \rangle\,\sin\theta\,\cos\theta. \end{aligned} \tag{2.5}$$

The rotation angle $\theta_{\min}$ which minimizes $\langle d^2 \rangle$ can be obtained as a function of the second moments and the correlation between x and p_x

$$\frac{\mathrm{d}\langle d^2 \rangle}{\mathrm{d}\theta} = 0 \quad \Rightarrow \quad \tan 2\theta_{\min} = \frac{2\langle x\,p_x \rangle}{\langle x^2 \rangle - \langle {p_x}^2 \rangle} \tag{2.6}$$

Furthermore, if $\theta = \theta_{\min}$ is $\langle d^2 \rangle = \langle \hat{p}_x^2 \rangle$. With some trigonometric identities 2.5 can be rewritten in case of $\theta = \theta_{\min}$ as:

$$\begin{aligned}
\langle \hat{p}_x^2 \rangle &= \frac{1}{2}\langle x^2 \rangle + \frac{1}{2}\langle {p_x}^2 \rangle + \frac{1}{2}\cos\left(2\,\theta_{\min}\right)\left(\langle {p_x}^2 \rangle - \langle x^2 \rangle\right) - \langle x\,p_x \rangle \sin\left(2\,\theta_{\min}\right) \\
&= \frac{1}{2}\langle x^2 \rangle + \frac{1}{2}\langle {p_x}^2 \rangle + \langle x\,p_x \rangle \left[\underbrace{\frac{\langle {p_x}^2 \rangle - \langle x^2 \rangle}{2\,\langle x\,p_x \rangle}}_{=-\tan^{-1}(2\theta_{\min})} \cos\left(2\theta_{\min}\right) - \sin\left(2\theta_{\min}\right) \right] \\
&= \frac{1}{2}\left(\langle x^2 \rangle + \langle {p_x}^2 \rangle - 2\,\frac{\langle x\,p_x \rangle}{\sin\left(2\theta_{\min}\right)} \left[\cos^2\left(2\theta_{\min}\right) + \sin^2\left(2\theta_{\min}\right) \right] \right) \\
&= \frac{1}{2}\left(\langle x^2 \rangle + \langle {p_x}^2 \rangle - 2\,\frac{\langle x\,p_x \rangle}{\sin\left(2\theta_{\min}\right)} \right).
\end{aligned} \tag{2.7}$$

With the same considerations $\langle \hat{x}^2 \rangle$ looks like

$$\langle \hat{x}^2 \rangle = \frac{1}{2}\left(\langle x^2 \rangle + \langle {p_x}^2 \rangle + 2\,\frac{\langle x\,p_x \rangle}{\sin\left(2\theta_{\min}\right)} \right). \tag{2.8}$$

2.8 and 2.7 can be used to determine the transverse emittance of a tilted ellipse in phase space. For the transverse emittance holds

$$\begin{aligned}
\epsilon_{n,x} &= \frac{1}{m_0\,c}\sqrt{\langle \hat{x}^2 \rangle \langle \hat{p}_x^2 \rangle} \\
&= \frac{1}{2\,m_0\,c}\left[\left(\langle x^2 \rangle + \langle {p_x}^2 \rangle \right)^2 - 4\,\frac{\langle x\,p_x \rangle^2}{\sin^2\left(2\theta_{\min}\right)} \right]^{1/2}.
\end{aligned} \tag{2.9}$$

The identity $\sin\left(\arctan\left(x\right)\right) = x/\sqrt{1+x^2}$ and 2.6 lead to

$$\epsilon_{n,x} = \frac{1}{m_0\,c}\sqrt{\langle x^2 \rangle \langle {p_x}^2 \rangle - \langle x\,p_x \rangle^2} \tag{2.10}$$

Besides the normalized rms emittance the geometrical emittance can be introduced. It is defined as

$$\epsilon_{rms} = \frac{m_0\,c}{\bar{p}_z}\,\epsilon_{n,rms} \tag{2.11}$$

In case of a small energy spread the averaged longitudinal momentum $\bar{p}_z$ can be drag into the square root of the geometrical emittance in order to define the often used trace space emittance:

$$\epsilon_{tr,rms} = \sqrt{\langle x^2 \rangle \langle x'^2 \rangle - \langle x\, x' \rangle^2} \tag{2.12}$$

with the beam divergence x' instead of the transverse momentum. While the trace space emittance is the relevant quantity for the following calculations of transfer matrices, the normalized rms emittance is the principal quantity which is comparable for different beam energies or other accelerators and hence it will be denoted as the final result of emittance measurements.

2.2 Beam transfer matrices

A practical way to describe the trajectory of a charged particle is the matrix formalism. It can be derived from the equation of motion of a charged particle in a longitudinal curvilinear and transverse Cartesian coordinate system [RS92].

$$x'' + K(z)\, x = \frac{1}{\varrho(z)} \frac{\Delta p}{p_0} \qquad \text{with} \quad K(z) = -k(z) + \frac{1}{\varrho^2(z)}. \tag{2.13}$$

k describes the focusing strength of an element. ϱ is the bending radius of a charged particle inside a homogeneous magnetic field like dipoles which are called dispersive beam line elements. The z axis depicts the so called design trajectory. A particle with no transverse offset and momentum and the longitudinal design momentum moves on this design trajectory. If the longitudinal momentum slightly differs from the design momentum p_0 it will move off the design trajectory in a dispersive section. 2.13 holds only for Δp much smaller than p_0.
The general solution of 2.13 contains a homogeneous and an inhomogeneous solution

$$x(z) = x_h(z) + x_i(z).$$

A linear accelerator does not have dispersive sections, so that the homogeneous part of the equation of motion describes a linear accelerator. For it the following ansatz is chosen

$$x_h(z) = C\, e^{\lambda z}. \tag{2.14}$$

In case of $K(z)$ is constant, which holds inside a magnet or along a drift, the homogeneous equation

$$x_h''(z) + K\, x_h(z) = 0$$

yields for λ

$$\begin{aligned} C\,\lambda^2 + K\,C = 0 \quad \Rightarrow \quad \lambda &= \pm\sqrt{-K} \\ &= \pm \mathrm{i}\sqrt{K}. \end{aligned} \tag{2.15}$$

Because the inhomogeneity is a constant it is sufficient to add a further constant to reach the complete solution of 2.13

$$x(z) = C_1\, e^{\mathrm{i}\sqrt{K}\,z} + C_2\, e^{-\mathrm{i}\sqrt{K}\,z} + C_3. \tag{2.16}$$

C_3 can be determined by inserting 2.16 into 2.13

$$C_3 = \frac{1}{\varrho\, K}\,\frac{\Delta p}{p_0}. \tag{2.17}$$

With x_0 and x_0' as the initial values at $z = z_0$ C_1 and C_2 can be determined from 2.13, so that the solution for $x(z)$ is given as

$$x_h(z) = x_0 \underbrace{\cos\left(\sqrt{K}\,z\right)}_{C(z)} + x_0' \underbrace{\frac{1}{\sqrt{K}}\,\sin\left(\sqrt{K}\,z\right)}_{S(z)} + \underbrace{\frac{1}{\varrho\, K}\,\left(1 - \cos\left(\sqrt{K}\,z\right)\right)}_{D(z)}\,\frac{\Delta p}{p_0}. \tag{2.18}$$

As one can see the initial beam parameters $(x_0, x_0', \Delta p/p_0)$ at $z = z_0$ are related to $(x(z), x'(z), \Delta p/p_0)$ by a linear transformation which can consequently be expressed by a matrix

$$\begin{pmatrix} x \\ x' \\ \frac{\Delta p}{p_0} \end{pmatrix} = \begin{pmatrix} C(z) & S(z) & D(z) \\ C'(z) & S'(z) & D'(z) \\ 0 & 0 & 1 \end{pmatrix} \begin{pmatrix} x_0 \\ x_0' \\ \frac{\Delta p}{p_0} \end{pmatrix}. \tag{2.19}$$

Every linear beam line element can be described by a so called transfer matrix. As examples and for further application I will introduce the transfer matrices of a drift and a thin lens approximation for magnetic lenses.

In a drift are no dispersive sections and no focusing elements hence k as well as $1/\varrho$ are equal to zero that yields K to be equal to zero. If $\sqrt{K}$ tend to zero, it is possible to simplify sine and cosine of the matrix of 2.19

$$\begin{aligned} \lim_{\sqrt{K}\to 0} \frac{\sin\left(\sqrt{K}\, z\right)}{\sqrt{K}} &= z \\ \lim_{\sqrt{K}\to 0} \cos\left(\sqrt{K}\, z\right) &= 1 \end{aligned} \tag{2.20}$$

With this results the transfer matrix of a drift section can be written as

$$\begin{pmatrix} \cos\left(\sqrt{K}\, l\right) & \frac{1}{\sqrt{K}} \sin\left(\sqrt{K}\, l\right) & \frac{1}{\varrho K}\left(1-\cos\left(\sqrt{K}\, l\right)\right) \\ -\sqrt{K} \sin\left(\sqrt{K}\, l\right) & \cos\left(\sqrt{K}\, l\right) & \frac{1}{\varrho} \sin\left(\sqrt{K}\, l\right) \\ 0 & 0 & 1 \end{pmatrix} = \begin{pmatrix} 1 & l & 0 \\ 0 & 1 & 0 \\ 0 & 0 & 1 \end{pmatrix} \tag{2.21}$$

with l as the length of the drift.
The thin lens approximation takes the position of a particle inside a focusing magnet as constant hence the transfer matrix can be approximated as

$$\begin{aligned} &\begin{pmatrix} \cos\left(\sqrt{K}\, l\right) & \frac{1}{\sqrt{K}} \sin\left(\sqrt{K}\, l\right) & \frac{1}{\varrho K}\left(1-\cos\left(\sqrt{K}\, l\right)\right) \\ -\sqrt{K} \sin\left(\sqrt{K}\, l\right) & \cos\left(\sqrt{K}\, l\right) & \frac{1}{\varrho} \sin\left(\sqrt{K}\, l\right) \\ 0 & 0 & 1 \end{pmatrix} \\ &= \begin{pmatrix} 1 & 0 & 0 \\ -\frac{1}{f} & 1 & 0 \\ 0 & 0 & 1 \end{pmatrix}. \end{aligned} \tag{2.22}$$

$K\, l = 1/f$ defines the focal length of a focusing magnet. Replacing it in 2.22 and afterwards let l tend to zero yields the following matrix for the thin lens approximation

$$\mathbf{M}_{\mathrm{tl}} = \begin{pmatrix} 1 & l & 0 \\ -K\, l & 1 & 0 \\ 0 & 0 & 1 \end{pmatrix}. \tag{2.23}$$

Because the upper examples are independent of a momentum deviation the transfer matrices can be reduced to 2×2 matrices like

$$\begin{pmatrix} 1 & l \\ 0 & 1 \end{pmatrix} \qquad \text{and} \qquad \begin{pmatrix} 1 & 0 \\ -\frac{1}{f} & 1 \end{pmatrix}. \tag{2.24}$$

The principal conclusion of this formalism is: it allows to find transfer matrices for all sections of a beam line. And furthermore the combination of n consecutive elements can mathematically expressed as the product of all n transfer matrices:

$$\begin{pmatrix} x \\ x' \\ \frac{\Delta p}{p_0} \end{pmatrix} = \underbrace{\mathbf{M}_1 \, \mathbf{M}_2 \ldots \mathbf{M}_{n-1} \, \mathbf{M}_n}_{\mathbf{M}_{\text{transfer}}} \begin{pmatrix} x_0 \\ x'_0 \\ \frac{\Delta p}{p_0} \end{pmatrix}. \tag{2.25}$$

This powerful tool is able to describe a whole accelerator beam line analytically. And in addition it can be used to simulate the development of an arbitrary particle distribution through a beam line. Besides the spatial distribution the phase space distribution is accessible as well. So that the distribution is physically complete described at every position z.

2.3 Beam dynamics of a single solenoid

At REGAE only solenoids for focusing the beam are in use. A sketch of a solenoid and its field is shown in fig. 2.3. In addition to the magnetic field B_z along the beam line a radial field B_r exists. The rotationally symmetric fields can be expanded in a polynomial series [WR88]:

$$\begin{aligned} B_z(z,r) &= B_{z,0} - \frac{r^2}{4}\frac{\mathrm{d}^2}{\mathrm{d}z^2}B_z(z) + \frac{r^4}{64}\frac{\mathrm{d}^4}{\mathrm{d}z^4}B_z(z)\ldots \\ B_r(z,r) &= -\frac{r}{2}\frac{\mathrm{d}}{\mathrm{d}z}B_z(z) + \frac{r^3}{16}\frac{\mathrm{d}^3}{\mathrm{d}z^3}B_z(z) - \frac{r^5}{384}\frac{\mathrm{d}^5}{\mathrm{d}z^5}B_z(z)\ldots \end{aligned} \tag{2.26}$$

with z as the principal axis of the accelerator, r as the transverse distance from z and $B_{z,0}$ as the on-axis magnetic field in z-direction.

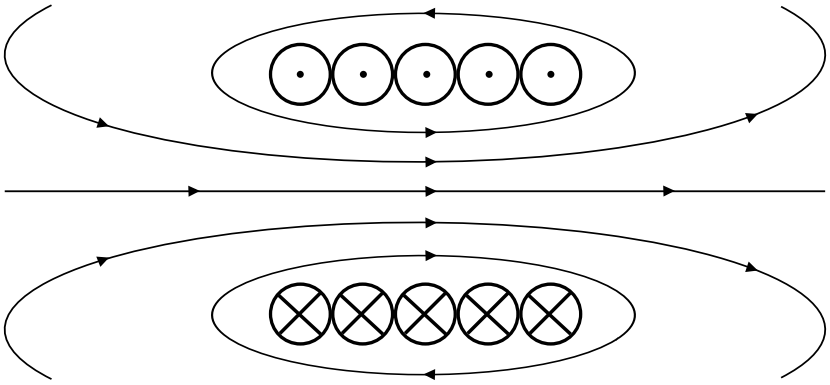

Figure 2.3: Magnetic field lines of a solenoid (short coil)

The equations of motion of a charged particle inside a solenoid field are coupled differential equations. For a co-rotating frame it is possible to decouple them (see 2.3.2).

2.3.1 Characteristic parameters

The important parameters of a solenoid are the focusing strength $1/f$ where f is the focal length and the rotation angle θ_L, called Larmor angle. They can be determined for a single charged particle with the help of the Lorentz force:

$$\mathbf{F} = q\,\mathbf{v} \times \mathbf{B}. \tag{2.27}$$

Because of the geometry of a solenoid it is useful to choose cylindrical coordinates [Jol05]. In a cylindrical frame these considerations are very descriptive as shown in the following. The correspondence between cylindrical and Cartesian coordinates is defined as:

$$\mathbf{r} = \begin{pmatrix} r\,\cos\theta \\ r\,\sin\theta \\ z \end{pmatrix}. \tag{2.28}$$

The unit vectors are defined as

$$\hat{\mathbf{r}} = \begin{pmatrix} \cos\theta \\ \sin\theta \\ 0 \end{pmatrix} \qquad \hat{\theta} = \begin{pmatrix} -\sin\theta \\ \cos\theta \\ 0 \end{pmatrix} \qquad \hat{\mathbf{z}} = \begin{pmatrix} 0 \\ 0 \\ 1 \end{pmatrix}. \tag{2.29}$$

So that the vector $\mathbf{r}$ can be read as

$$\mathbf{r} = r\,\hat{\mathbf{r}} + z\,\hat{\mathbf{z}}. \tag{2.30}$$

Two other important identities are the first and second time derivatives, denoted with a dot:

$$\frac{\mathrm{d}\mathbf{r}}{\mathrm{d}t} = \dot{r}\,\hat{\mathbf{r}} + r\,\dot{\theta}\begin{pmatrix}-\sin\theta\\ \cos\theta\\ 0\end{pmatrix} + \dot{z}\,\hat{\mathbf{z}} = \dot{r}\,\hat{\mathbf{r}} + r\,\dot{\theta}\,\hat{\theta} + \dot{z}\,\hat{\mathbf{z}} \tag{2.31}$$

$$\begin{aligned}\frac{\mathrm{d}^2\mathbf{r}}{\mathrm{d}t^2} &= \ddot{r}\,\hat{\mathbf{r}} + \dot{r}\,\dot{\theta}\,\hat{\theta} + \dot{r}\,\dot{\theta}\,\hat{\theta} + r\,\ddot{\theta}\,\hat{\theta} + r\,\dot{\theta}^2\underbrace{\begin{pmatrix}-\cos\theta\\ -\sin\theta\\ 0\end{pmatrix}}_{=-\hat{\mathbf{r}}} + \ddot{z}\,\hat{\mathbf{z}}\\ &= \left(\ddot{r} - r\,\dot{\theta}^2\right)\hat{\mathbf{r}} + \left(2\,\dot{r}\,\dot{\theta} + r\,\ddot{\theta}\right)\hat{\theta} + \ddot{z}\,\hat{\mathbf{z}}.\end{aligned} \tag{2.32}$$

For the right-hand side of 2.27 follows with 2.31

$$\begin{aligned}\gamma\,m_0\,\ddot{\mathbf{r}} &= q\,\dot{\mathbf{r}}\times\mathbf{B}\\ &= q\,\left[\left(r\,\dot{\theta}\,B_z - \dot{z}\,B_\theta\right)\hat{\mathbf{r}} + \left(\dot{z}\,B_r - \dot{r}\,B_z\right)\hat{\theta} + \left(\dot{r}\,B_\theta - r\,\dot{\theta}\,B_r\right)\hat{\mathbf{z}}\right].\end{aligned} \tag{2.33}$$

$\mathbf{F}$ has been replaced by the relativistic expression of an arbitrary force.
Now it is possible to formulate the equations of motion for the three spatial directions (r, θ, z) with 2.32, 2.33 and $B_\theta = 0$. To reduce the dependency of these equations on the different magnetic field components, $B_r(z, r)$ can be approximated by the linear part of the second equation of 2.26 and the following equations are obtained:

Focusing:

$$\gamma\,m_0\,\left(\ddot{r} - r\,\dot{\theta}^2\right) = q\,r\,\dot{\theta}\,B_z \tag{2.34}$$

Rotation:

$$\gamma\,m_0\,\left(2\,\dot{r}\,\dot{\theta} + r\,\ddot{\theta}\right) = -q\left(\frac{r\,\dot{z}}{2}\,B_z{}' + \dot{r}\,B_z\right) \tag{2.35}$$

Acceleration:

$$\gamma\, m_0\, \ddot{z} = \frac{1}{2} q\, r^2\, \dot{\theta}\, {B_z}' \tag{2.36}$$

The right-hand sides of 2.34 to 2.36 describes the sources of the different forces while the left-hand sides describes the absolute value of the force. These identities are linear approximations which only hold for electrons near the z-axis of the solenoid. In case of solenoids at REGAE the maximum offset r_{off} of a particle should be less than 3 mm. Then the relative field error is less than 10 %.
To determine the Larmor angle θ_L only the equation for the rotation is needed. With

$$\begin{aligned} \frac{\mathrm{d}}{\mathrm{d}t}\left(r^2\,\dot{\theta}\right) &= r^2\,\ddot{\theta} + 2\,r\,\dot{r}\,\dot{\theta} \\ \frac{\mathrm{d}}{\mathrm{d}t}\left(r^2\,B_z\right) &= r^2\,\dot{B}_z + 2\,r\,\dot{r}\,B_z \\ \dot{B}_z = \frac{\mathrm{d}B_z}{\mathrm{d}t} &= \frac{\mathrm{d}B_z}{\mathrm{d}z}\frac{\mathrm{d}z}{\mathrm{d}t} = {B_z}'\,\dot{z} \end{aligned} \tag{2.37}$$

it follows

$$\begin{aligned} \frac{\gamma\, m_0}{r}\,\left(2\,r\,\dot{r}\,\dot{\theta} + r^2\,\ddot{\theta}\right) &= -\frac{q}{2\,r}\left(r^2\,\dot{z}\,{B_z}' + 2\,r\,\dot{r}\,B_z\right) \\ \frac{\gamma\, m_0}{r}\,\frac{\mathrm{d}}{\mathrm{d}t}\left(r^2\,\dot{\theta}\right) &= -\frac{q}{2\,r}\,\frac{\mathrm{d}}{\mathrm{d}t}\left(r^2\,B_z\right) \\ r^2\,\dot{\theta} &= -\frac{q}{2\,\gamma\, m_0}\,r^2\,B_z \\ \theta &= -\frac{q}{2\,\gamma\, m_0}\int B_z\,\mathrm{d}t. \end{aligned} \tag{2.38}$$

For the last two steps both sides of the equation were integrated. It is common praxis in accelerator physics to replace time derivatives by derivatives of z thus

$$\mathrm{d}t = \frac{\mathrm{d}t}{\mathrm{d}z}\mathrm{d}z = \frac{\mathrm{d}z}{\dot{z}}. \tag{2.39}$$

Using this result and taking p_z as constant yields a more common form of 2.38

$$\theta = -\int \frac{q\,B_z}{2\,p_z}\,\mathrm{d}z. \tag{2.40}$$

The focusing strength can be calculated by combining 2.38 and the focusing equation of motion 2.34:

$$\begin{aligned}
\gamma\, m_0 \left(\ddot{r} - r\,\dot{\theta}^2\right) &= q\, r\, \dot{\theta}\, {B_z} \\
\Rightarrow \ddot{r} &= -\frac{q^2\, r}{2\,(\gamma\, m_0)^2}\, {B_z}^2 + \frac{q^2\, r}{4\,(\gamma\, m_0)^2}\, {B_z}^2 \\
&= -\frac{q^2\, r}{4\,(\gamma\, m_0)^2}\, {B_z}^2 \\
\Rightarrow \dot{r} &= -\frac{q^2}{4\,(\gamma\, m_0)^2} \int r\, {B_z}^2\, \mathrm{d}t \\
r' &= -\frac{q^2}{4} \int \underbrace{\frac{r\, {B_z}^2}{(\gamma\, m_0\, \dot{z})^2}}_{{p_z}^2}\, \mathrm{d}z.
\end{aligned} \tag{2.41}$$

If r is assumed to be constant in the vicinity of the solenoid a thin lens approximation is possible. The focusing strength is given as

$$\frac{1}{f} = -\frac{r'}{r}.$$

Replacing r' yields

$$\frac{1}{f} = \int \left(\frac{q\, {B_z}^2}{2\, p_z}\right)^2 \mathrm{d}z. \tag{2.42}$$

As long as the energy spread is small the replacement of the particle momentum p_z by the averaged momentum $\bar{p}_z$ in 2.40 and 2.42 is a good approximation to determine the Larmor angle and the focusing strength of a solenoid.

2.3.2 Trajectory of a charged particle

For the determination of the characteristic solenoid parameters a thin lens approximation was sufficient but in case of a misaligned solenoid and its consequence for the beam alignment it is necessary to investigate the trajectory of a charged particle in detail which means we need to consider the transverse beam offset as a function of z. It is a fact that the solenoid introduces a rotation with respect to the symmetry axis to a charged particle. Therefore it is useful to transform

from the laboratory frame to a co-rotating frame. Starting again with the Lorentz force, but in this case in Cartesian coordinates, yields

$$\begin{aligned} \frac{\mathrm{d}p_x}{dt} &= q\,c(\beta_y\,B_z - \beta_z\,B_y) \\ \frac{\mathrm{d}p_y}{dt} &= q\,c(\beta_z\,B_x - \beta_x\,B_z). \end{aligned} \tag{2.43}$$

The transformed coordinates inside the solenoid look like

$$\begin{aligned} \tilde{x}(z) &= x\,\cos\theta_L(z) - y\,\sin\theta_L(z) \\ \tilde{y}(z) &= x\,\sin\theta_L(z) + y\,\cos\theta_L(z). \end{aligned} \tag{2.44}$$

From this definition follows

$$\begin{aligned} \tilde{y} = r \quad \beta_{\tilde{y}} = \beta_r \quad B_{\tilde{y}} = B_r \\ \tilde{x} = 0 \quad \beta_{\tilde{x}} = -\beta_\theta \quad B_{\tilde{x}} = 0. \end{aligned} \tag{2.45}$$

Notice that r does not denote the radius as in cylindrical coordinates. It is just a definition for the transformed Cartesian y and therefore it can be negative. Another important fact is the opposite algebraic sign of $\beta_{\tilde{x}}$ in comparison with β_θ. It is a consequence of the rotation direction of the new frame.
Now it is possible to transform 2.43 into the new coordinate system. In an accelerated rotating frame like this appears beside the Lorentz force three pseudo forces - the centrifugal, Coriolis and Euler force. 2.43 can now be transformed into the co-rotating frame:

$$\begin{aligned} \frac{\mathrm{d}p_{\tilde{y}}}{\mathrm{d}t} &= q\,c(-\beta_\theta\,B_z) + F_{\mathrm{centr}} \\ \frac{\mathrm{d}p_{\tilde{x}}}{\mathrm{d}t} &= -q\,c(\beta_r\,B_z - \beta_z\,B_r) + F_{\mathrm{Cor}} + F_{\mathrm{Euler}}. \end{aligned} \tag{2.46}$$

The additional forces are given as:

$$\begin{aligned} F_{\mathrm{centr}} &= \gamma\,m\,\dot{\theta}^2\,r \\ F_{\mathrm{Cor}} &= -2\gamma\,m\,\dot{\theta}\,c\,\beta_r \\ F_{\mathrm{Euler}} &= -\gamma\,m_0\,\ddot{\theta}\,r. \end{aligned} \tag{2.47}$$

The angular velocity $\dot{\theta}$ and acceleration $\ddot{\theta}$ can be obtained by the derivations of 2.38 and the approximated relation $\dot{z} = \beta_z\, c$ where β_z is taken as constant.

$$\dot{\theta} = -\frac{q\, B_z}{2\,\gamma\, m_0} \tag{2.48}$$

$$\begin{aligned} \ddot{\theta} &= -\frac{q\, \dot{B}_z}{2\,\gamma\, m_0} \\ &= -\frac{q\,\beta_z\, c\, {B_z}'}{2\,\gamma\, m_0} \end{aligned} \tag{2.49}$$

Inserting 2.47 into 2.46, substituting $\mathrm{d}t$ with $\mathrm{d}z/(\beta_z\, c)$ and keeping in mind that $\beta_\theta = \dot{\theta}\, r/c$ yields two differential equations

$$\begin{aligned} \frac{\mathrm{d}p_{\tilde{y}}}{\mathrm{d}z} &= -r\,\frac{(q\, B_z)^2}{4\, p_z} \\ \frac{\mathrm{d}p_{\tilde{x}}}{\mathrm{d}z} &= 0. \end{aligned} \tag{2.50}$$

The first equation of 2.50 is the equation of motion in r direction. Because the frame is rotated by $\theta(z)$, $\mathrm{d}p_{\tilde{x}}/\mathrm{d}z$ has to be equal to zero.
If it is possible to solve the differential equation for r the trajectory of a charged particle through a solenoid is determined. In a reformulated way the equation of motion looks like

$$\begin{aligned} \frac{\mathrm{d}p_{\tilde{y}}}{\mathrm{d}z} = \frac{\mathrm{d}p_r}{\mathrm{d}z} &= \gamma\, m_0\,\frac{\mathrm{d}^2 r}{\mathrm{d}z\,\mathrm{d}t} = \underbrace{\gamma\, m_0\,\beta_z\, c}_{=p_z}\,\frac{\mathrm{d}^2 r}{\mathrm{d}z^2} \\ \Rightarrow \quad \frac{\mathrm{d}^2 r(z)}{\mathrm{d}z^2} &+ \left(\frac{q\, B_z(z)}{2\, p_z}\right)^2 r(z) = 0. \end{aligned} \tag{2.51}$$

To solve this differential equation it is important to recognize the dependence of the magnetic field B_z on z. This makes it difficult to find a solution for 2.51.
At REGAE the solenoid fields have pretty much the same shape as the field of a short coil. The fields are just increased by an iron yoke which does not change the magnetic field shape. In 1951 F. Lenz used an analytical approximation for the magnetic field B_z of a short coil [Len51, HK96]. He described the field by a hyperbolic secant

$$B_z(z) = B_0\ \mathrm{sech}\left(1.32\,\frac{z}{a}\right). \tag{2.52}$$

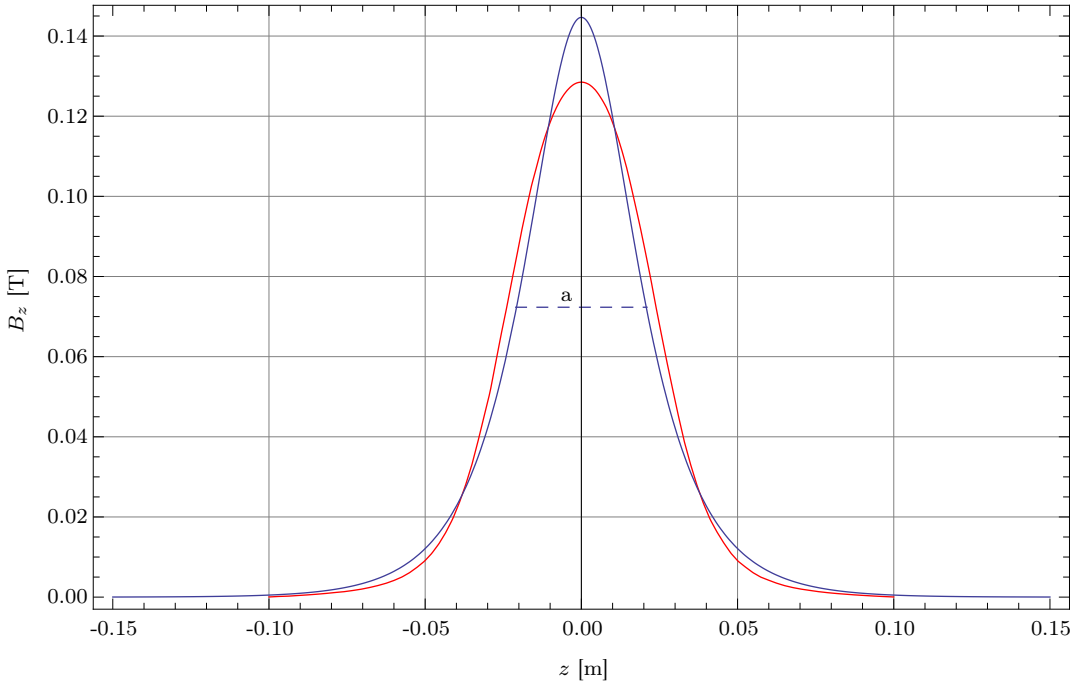

Figure 2.4: Comparison between the real $B_z(z)$ (red) of a single solenoid at REGAE and the Lenz approximation (blue). a is the FWHM of the Lenz field.

Instead of fitting the real field with 2.52 both parameters in the Lenz approximation have to be adapted to the real field to create a magnetic field with the same physical properties. These properties are the focusing strength and the Larmor angle introduced in the former section. The Full Width at Half Maximum (FWHM) a of the field and the field amplitude B_0 are connected to the characteristic parameters by the first and second field integrals of B_z:

$$\begin{aligned} F_1 = \int_{-\infty}^{\infty} B_{z,\mathrm{Sol}}(z)\,\mathrm{d}z &= \int_{-\infty}^{\infty} B_{z,\mathrm{Lenz}}(z)\,\mathrm{d}z \\ &= \int_{-\infty}^{\infty} B_0\ \mathrm{sech}\left(1.32\,\frac{z}{a}\right)\mathrm{d}z = \frac{\pi\,a\,B_0}{1.32} \end{aligned} \tag{2.53}$$

$$F_2 = \int_{-\infty}^{\infty} {B_{z,\mathrm{Sol}}}^2(z)\,\mathrm{d}z = \int_{-\infty}^{\infty} {B_{z,\mathrm{Lenz}}}^2(z)\,\mathrm{d}z$$
$$= \int_{-\infty}^{\infty} {B_0}^2\,\mathrm{sech}^2\left(1.32\,\frac{z}{a}\right)\mathrm{d}z = \frac{2\,a\,{B_0}^2}{1.32}. \tag{2.54}$$

An example of the magnetic field of a REGAE single solenoid is shown in fig. 2.4 with

$$B_0 = 1.13 \cdot B_{z,max} \qquad \text{and} \qquad a = 0.0157\,\mathrm{m}.$$

Replacing the magnetic field in 2.51 by the Lenz field makes it possible to solve the differential equation. With

$$u = -\tanh\left(1.32\frac{z}{a}\right)$$

and

$$\nu(\nu+1) = \left(\frac{q\,B_0}{2\,p_z}\right)^2$$

the equation of motion (2.51) simplifies to

$$(1-u^2)\,\frac{\mathrm{d}^2 r}{\mathrm{d}u^2} - 2u\,\frac{\mathrm{d}r}{\mathrm{d}u} + \nu(\nu+1)\,r = 0. \tag{2.55}$$

This is Legendre's differential equation and its general solution is

$$r(z) = C_1\,P_\nu\left(-\tanh\left(1.32\,\frac{z}{a}\right)\right) + C_2\,Q_\nu\left(-\tanh\left(1.32\,\frac{z}{a}\right)\right). \tag{2.56}$$

$P_\nu(u)$ and $Q_\nu(u)$ are the first and second kind of the Legendre polynomials. It is important to notice that ν does not have to be an integer. If ν is an integer the polynomials however are well defined.
F. Lenz was only able to solve 2.56 in case of a parallel incoming beam ($C_2 = 0$) by combining certain magnetic field and beam parameters which yields integers or half integers for ν. But all this only gave him an idea of the beam dynamics

of a charged particle in electron microscopes. A description of a trajectory for arbitrary parameters was not possible.
To determine the coefficients C_1 and C_2 it is a standard approach to set boundary conditions. For a infinitely long magnetic field the boundary conditions has to be

$$r(-\infty) = r_0 \qquad r'(-\infty) = {r_0}'.$$

But in this case these boundary conditions are not suitable. For a non-zero ${r_0}'$ the source size r_0 has to be infinitely large to get a finite $r(z)$ in the vicinity of the solenoid. So the initial conditions have to be chosen near by the solenoid with the consequence of accepting calculation errors for the focusing strength and the Larmor angle. z has to be large enough in order to reach a small field amplitude, so that the errors keep small. The fraction of the maximum field B_0 at position z is

$$\frac{B_0 \operatorname{sech}\left(\frac{10\,a}{a}\right)}{B_0 \operatorname{sech}\left(\frac{0}{a}\right)} = \operatorname{sech} 10 = 9.1 \cdot 10^{-5} \qquad \text{for} \quad z = 10 \cdot a.$$

So, the error is small enough to yield a precise description of the trajectory of a charged particle through a solenoid.
The results for C_1 and C_2 are very complex expressions (see. 2.A). They depend, as expected, on the initial conditions as well as on ν which depends itself on the field amplitude B_0 and the beam momentum p_z.

$$C_1 = C_1(r_0, r_0', B_0, p_z)$$
$$C_2 = C_2(r_0, r_0', B_0, p_z)$$

The whole solution of 2.56 is illustrated for a particular parameter set in fig. 2.5 for a single solenoid at REGAE.

2.3.3 Transformation from a co-rotating frame to laboratory system

The equation of motion (2.56) is defined in a co-rotating frame. To evaluate an alignment measurement of a solenoid it is necessary to find a transformation from the co-rotating frame back to the laboratory system. The following matrices describe this kind transformations [RSW82].

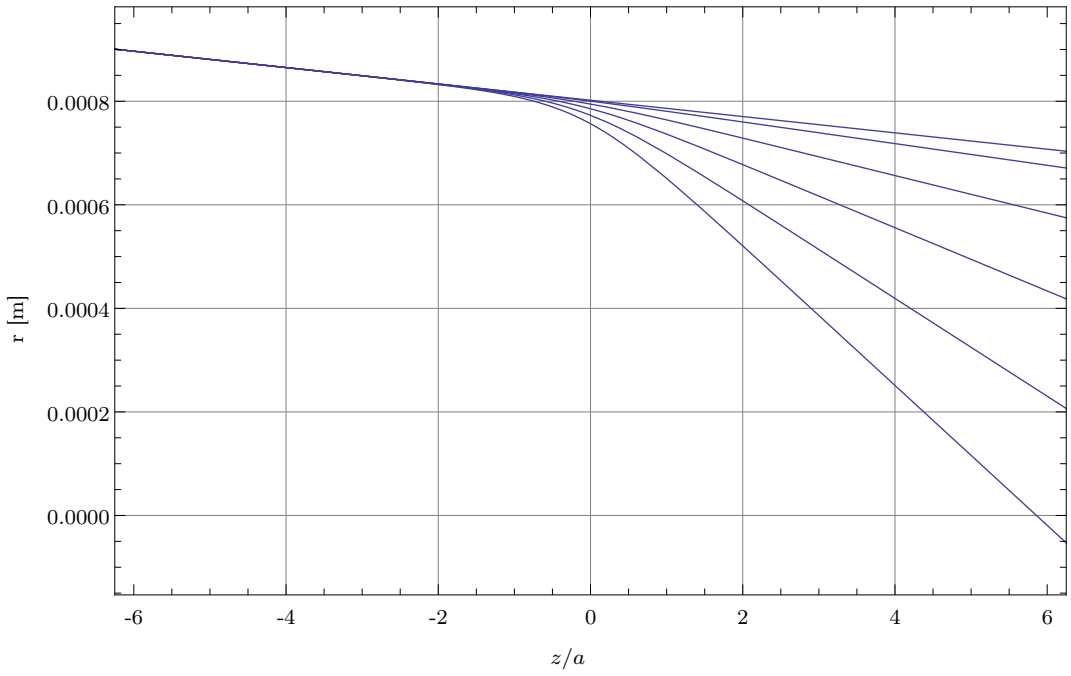

Figure 2.5: Trajectory of an electron in the co-rotating frame for field amplitudes from 0 T to 0.64 T. $r_0 = 10^{-3}$ m, $r_0' = 10^{-3}$ rad and $E_{\text{kin}} = 5$ MeV. The solenoid center is at $z/a = 0$. a is the FWHM of the Lenz field for the approximation of a REGAE single solenoid.

First of all a transfer matrix E has to be found which describes the transfer from the initial to the final particle parameters inside the co-rotating frame:

$$\begin{pmatrix} \tilde{y} \\ p_{\tilde{y}} \end{pmatrix}_{\text{out}} = \mathbf{E} \begin{pmatrix} \tilde{y} \\ p_{\tilde{y}} \end{pmatrix}_{\text{in}} . \tag{2.57}$$

$\tilde{x}$ and $\tilde{y}$ are decoupled so that the transformation can be executed separately. Furthermore the transfer matrix $\mathbf{E}$ does not differ for $\tilde{x}$ and $\tilde{y}$ due to the rotationally symmetric magnetic field. So a 4×4 matrix with the transfer matrix $\mathbf{E}$ included looks like

$$\mathbf{F} = \begin{bmatrix} \mathbf{E} & 0 \\ 0 & \mathbf{E} \end{bmatrix} . \tag{2.58}$$

In addition to the transfer matrix $\mathbf{E}$ a transfer matrix for the induced rotation angle θ_L has to be introduced and looks like

$$\mathbf{M} = \begin{bmatrix} \cos\theta_L & 0 & -\sin\theta_L & 0 \\ 0 & \cos\theta_L & 0 & -\sin\theta_L \\ \sin\theta_L & 0 & \cos\theta_L & 0 \\ 0 & \sin\theta_L & 0 & \cos\theta_L \end{bmatrix}. \tag{2.59}$$

Together $\mathbf{E}$ and $\mathbf{M}$ form the transfer matrix $\mathbf{N}$ in the laboratory system through a solenoid

$$\mathbf{N} = \mathbf{M} \cdot \mathbf{F} = \mathbf{F} \cdot \mathbf{M}. \tag{2.60}$$

At the entrance of a solenoid the co-rotating frame and laboratory system coincide. Therefore x and $\tilde{x}$ are equal and the transformation can be formulated as

$$\begin{pmatrix} x \\ p_x \\ y \\ p_y \end{pmatrix}_{\text{out}} = \mathbf{N} \begin{pmatrix} x \\ p_x \\ y \\ p_y \end{pmatrix}_{\text{in}}. \tag{2.61}$$

In case of the solution of Legendre's differential equation (2.56) it is not possible to find a transfer matrix $\mathbf{E}$. But $r(z)$ is equal to $E_{11}\,\tilde{y}_{in} + E_{12}\,p_{\tilde{y},in}$ and $r'(z) = E_{21}\,\tilde{y}_{in} + E_{22}\,p_{\tilde{y},in}$, so that 2.61 can be expressed as

$$\begin{pmatrix} x \\ p_x \\ y \\ p_y \end{pmatrix}_{\text{out}} = \mathbf{N} \begin{pmatrix} x \\ p_x \\ y \\ p_y \end{pmatrix}_{\text{in}} = \mathbf{M} \begin{pmatrix} r(z, x_0, {x_0}') \\ r'(z, x_0, {x_0}') \\ r(z, y_0, {y_0}') \\ r'(z, y_0, {y_0}') \end{pmatrix}_{\text{in}} \tag{2.62}$$

where p_x and p_y has been replaced by the particle divergence x' and y'.
The trajectory of an electron for different solenoid fields in the laboratory system is depicted in fig. 2.6. The red dots can be measured on a beam detecting screen and be used for the beam based alignment of a single solenoid to fit its transverse offset and tilt towards the principal axis of an accelerator (see section 6.4.1).

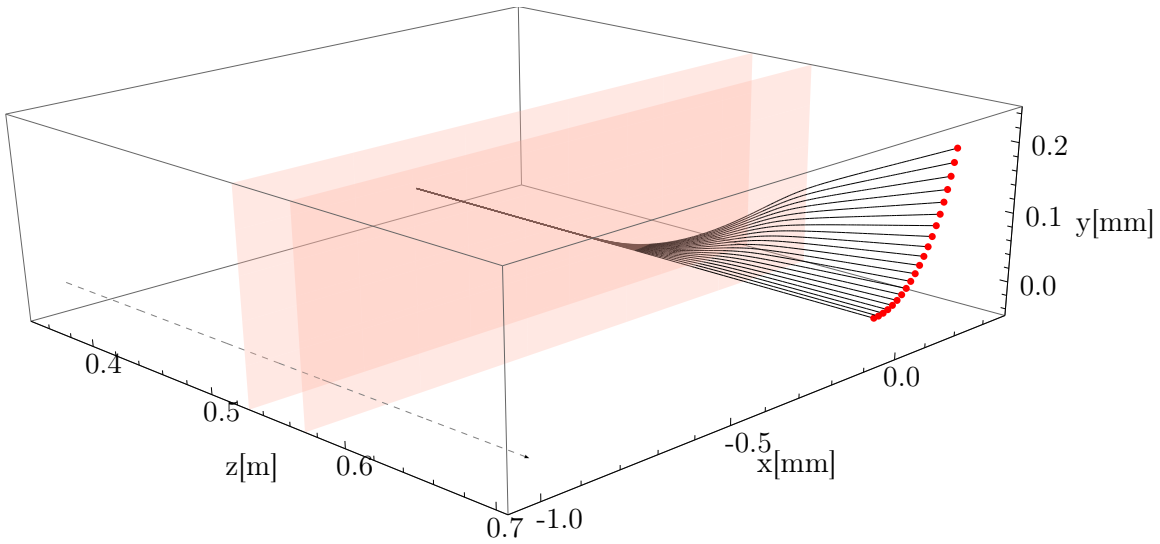

Figure 2.6: Trajectory of an electron in Cartesian coordinates for different field amplitudes. Red transparent rectangles denote the edges of the solenoid. The gray dashed line is the solenoid axis. Beam has an offset of $x_0 = 1\,\mathrm{mm}$. Solenoid center is at $z = 0.55\,\mathrm{m}$. The red dots lie in a x-y-plane at $z = 0.7\,\mathrm{m}$

2.4 Improved beam dynamics of a double solenoid

A double solenoid consist of two connected single solenoid with opposite sign of current. Therefore the magnetic field is the superposition of two single solenoid fields. An example for the magnetic field of a double solenoid at REGAE is shown in fig. 2.7. In contrast to a single solenoid the introduced Larmor angle is equal to zero due to the fact that the second half compensates the introduced rotation of the first half of the double solenoid. This can be expressed mathematically as the integral of B_z

$$\theta_L \sim \int_{-\infty}^{\infty} B_z \, \mathrm{d}z = 0.$$

The focusing strength instead is increased because it depends on the square of the magnetic field B_z. In principal it is possible to approximate this field as a thin lens. But a better approximation is the double thin lens. Both parts of the double solenoid are approximated by a thin lens which are connected by a short drift section. The transfer matrix is given as

$$\begin{aligned}
\mathbf{M}_{\mathrm{DS}} &= \mathbf{M}_{\mathrm{SS}} \cdot \mathbf{M}_{\mathrm{Drift}} \cdot \mathbf{M}_{\mathrm{SS}} \\
&= \begin{pmatrix} 1 & 0 \\ -\frac{1}{\frac{1}{2} f_{\mathrm{DS}}} & 1 \end{pmatrix} \cdot \begin{pmatrix} 1 & l_{\mathrm{Drift}} \\ 0 & 1 \end{pmatrix} \cdot \begin{pmatrix} 1 & 0 \\ -\frac{1}{\frac{1}{2} f_{\mathrm{DS}}} & 1 \end{pmatrix} \\
&= \begin{pmatrix} 1 - 2\,(l_{\mathrm{Drift}}/f_{\mathrm{DS}}) & l_{\mathrm{Drift}} \\ 4\,(l_{\mathrm{Drift}} - f_{\mathrm{DS}})/f_{\mathrm{DS}}^2 & 1 - 2\,(l_{\mathrm{Drift}}/f_{\mathrm{DS}}) \end{pmatrix}.
\end{aligned} \tag{2.63}$$

The focusing strength can be calculated as presented in 2.42. Both halves contain half of the focusing strength of a double solenoid. This matrix will be used for the beam envelope model in order to fit the transverse emittance.

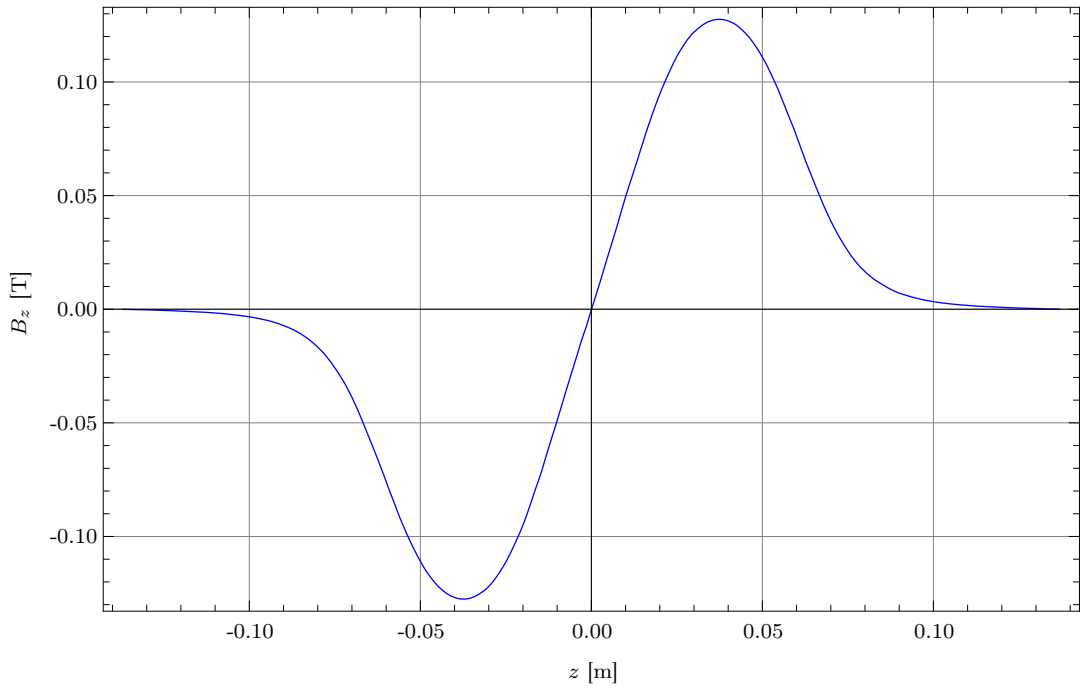

Figure 2.7: Magnetic field B_z in longitudinal direction of a double solenoid at REGAE.

2.A Explicit coefficients of Legendre's differential equation

```
Out[1437]= {((63.43830778472278` + 63.43830778472278` nu) r0
      LegendreQ[1.` + nu, 0, 2.`, -1.` Tanh[63.43830778472279` dstc$94763]] +
    LegendreQ[nu, 0, 2.`, -1.` Tanh[63.43830778472279` dstc$94763]]
     (-1.` r0dz Cosh[63.43830778472278` dstc$94763]^2 +
       1.` r0dz Sinh[63.43830778472278` dstc$94763]^2 + (63.43830778472278` +
          63.43830778472278` nu) r0 Tanh[63.43830778472278` dstc$94763])) /
   ((-63.43830778472278` - 63.43830778472278` nu) LegendreP[1.` + nu,
      -1.` Tanh[63.43830778472279` dstc$94763]]
     LegendreQ[nu, 0, 2.`, -1.` Tanh[63.43830778472279` dstc$94763]] +
    (63.43830778472278` + 63.43830778472278` nu)
     LegendreP[nu, -1.` Tanh[63.43830778472279` dstc$94763]]
     LegendreQ[1.` + nu, 0, 2.`, -1.` Tanh[63.43830778472279` dstc$94763]]),
  ((-63.43830778472278` - 63.43830778472278` nu) r0
      LegendreP[1.` + nu, -1.` Tanh[63.43830778472279` dstc$94763]] +
    LegendreP[nu, -1.` Tanh[63.43830778472279` dstc$94763]]
     (1.` r0dz Cosh[63.43830778472278` dstc$94763]^2 -
       1.` r0dz Sinh[63.43830778472278` dstc$94763]^2 + (-63.43830778472278` -
          63.43830778472278` nu) r0 Tanh[63.43830778472278` dstc$94763])) /
   ((-63.43830778472278` - 63.43830778472278` nu) LegendreP[1.` + nu,
      -1.` Tanh[63.43830778472279` dstc$94763]]
     LegendreQ[nu, 0, 2.`, -1.` Tanh[63.43830778472279` dstc$94763]] +
    (63.43830778472278` + 63.43830778472278` nu)
     LegendreP[nu, -1.` Tanh[63.43830778472279` dstc$94763]]
     LegendreQ[1.` + nu, 0, 2.`, -1.` Tanh[63.43830778472279` dstc$94763]])}
```

Figure 2.8: The red marked term is the complete expression of C_1 from Legendre's differential equation. In contrast the blue marked term expresses C_2. r0 and r0dz represent the initial condition (r_0, r_0') at $z = z_0$. dstc$94763 is equal to the distance between z_0 and $z = 0$ if $z = 0$ is the center of the solenoid. dstc$94763 is in the range of 10 times the FWHM a of the Lenz field.

3

Transverse emittance

In the following chapter two models which describe the envelope of a beam with and without space charge effects are presented. Then a analytical and numerical fit procedure for emittance measurements will be introduced.

3.1 Transverse envelope equation

There are different ways to measure the emittance of a beam. A standard way is the "quad-scan" method - in case of the REGAE experiment it should be called "sol-scan" method. Thereby the transversal beam size is measured while the solenoid focusing is changed. This method suggests a model which describes the development of the beam envelope in dependence of the focusing strength. In case of neglecting space charge effects the envelope of a bunch is well known and often used, but the space charge effects can strongly contribute to the evolution of the beam size so that it is preferable to take them into account for beam dynamical issues. An analytically approximated envelope equation, which includes space charge effects, will be presented in this chapter.

3.1.1 Envelope equation without space charge

The trajectory of an charged particle can be described with the mentioned matrix formalism in section 2.2. The chaining of all beam dynamical sections which a charged particle passes describes its transversal motion. Mathematically it can be

expressed with the matrices product (2.25):

$$\begin{aligned} \begin{pmatrix} x \\ x' \end{pmatrix} &= \mathbf{M}_{\text{trans}} \begin{pmatrix} x_0 \\ x'_0 \end{pmatrix} \\ \mathbf{M}_{\text{trans}} &= \begin{pmatrix} C_{11} & C_{12} \\ C_{21} & C_{22} \end{pmatrix}. \end{aligned} \tag{3.1}$$

This results in the transversal equation of motion

$$x = C_{11}\, x_0 + C_{12}\, x'_0. \tag{3.2}$$

Only the rms beam size is an accessible value by measurements. Therefore this equation of motion has to be transformed into an rms envelope equation which depicts the dynamics of the whole beam [Flö11b, chap.1.6]. Calculating the second moment yields

$$\begin{aligned} {x_{rms}}^2 = \langle x^2 \rangle &= \langle (C_{11}\, x_0)^2 \rangle + \langle 2\, C_{11}\, C_{12}\, x_0\, x'_0 \rangle + \langle (C_{12}\, x'_0)^2 \rangle \\ &= {C_{11}}^2\, \langle {x_0}^2 \rangle + 2\, C_{11}\, C_{12}\, \langle x_0\, x'_0 \rangle + {C_{12}}^2\, \langle {x'_0}^2 \rangle. \end{aligned} \tag{3.3}$$

The three unknown identities can be determined in the following way:

1. the source size is written as $\langle {x_0}^2 \rangle = {x_{0,rms}}^2$
2. determination of the envelope slope $(x_{rms})'$:

$$(x_{rms})' = \frac{\partial}{\partial z} \langle x^2 \rangle^{1/2} = \frac{\langle x\, x' \rangle}{\langle x^2 \rangle^{1/2}} \quad \Rightarrow \quad \langle x\, x' \rangle = x_{rms}\ (x_{rms})' \tag{3.4}$$

3. denoting $\epsilon_{rms} = \epsilon_{tr,rms}$ and 2.12 yields for $\langle {x'}^2 \rangle$

$$\langle {x'}^2 \rangle = \frac{{\epsilon_{rms}}^2}{\langle x^2 \rangle} + \frac{\langle x\, x' \rangle^2}{\langle x^2 \rangle} = \frac{{\epsilon_{rms}}^2}{{x_{rms}}^2} + (x_{rms})'^2 \tag{3.5}$$

With the upper identities 3.3 can be expressed as

$${x_{rms}}^2 = {C_{11}}^2\, {x_{0,rms}}^2 + 2\, C_{11}\, C_{12}\, x_{0,rms}\ (x_{0,rms})' + {C_{12}}^2 \left(\frac{{\epsilon_{rms}}^2}{{x_{0,rms}}^2} + (x_{0,rms})'^2 \right). \tag{3.6}$$

$x_{0,rms}$, $(x_{0,rms})'$ and ϵ_{rms} are the free parameters of this model and have to be determined.
The matrix elements C_{11} and C_{12} depend on the geometry of the experiment and the solenoid focusing strength. As long as the geometry, meaning the distance between the solenoid and a screen or detector, is known the beam size can be measured with respect to the magnetic field. A plot which demonstrates a principal measurement by the "sol-scan" method is shown in fig. 3.1. The black dots illustrate a possible measurement whereas the red curve is a fit developed from the envelope model. If the emittance slightly changes for the fitted curve mainly the depth of the minimum changes. This indicates that this method is most sensitive to beam size right at the minimum and hence it has to be the aim to determine the minimum very well for a emittance measurement by the "sol-scan" method.

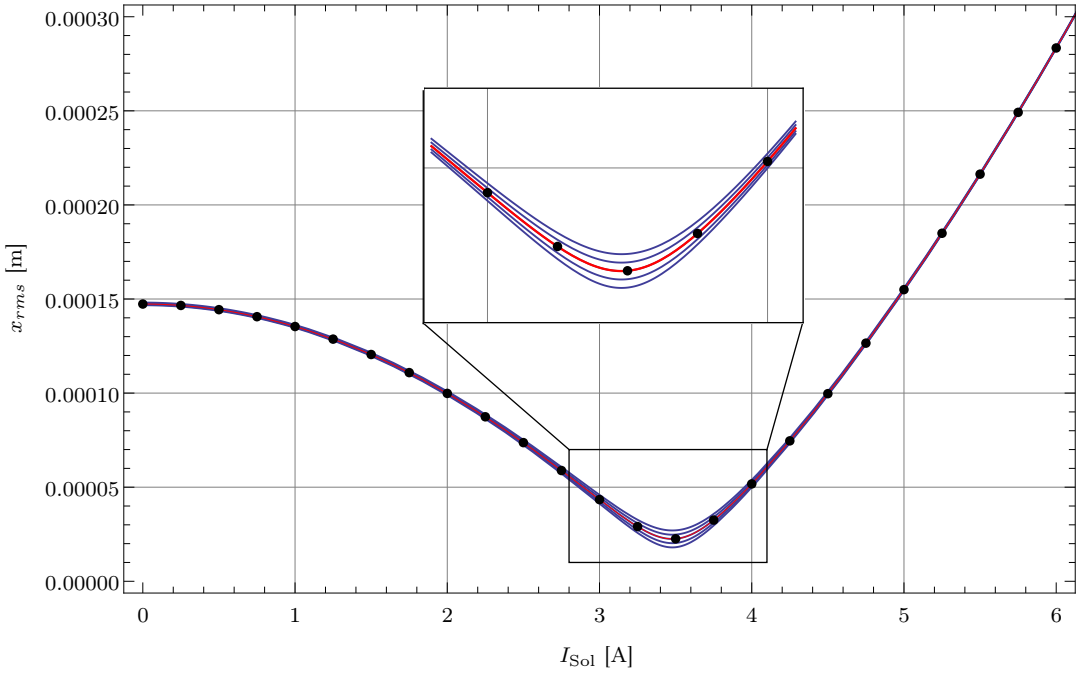

Figure 3.1: Beam size x_{rms} against solenoid current I_{sol} for a slightly varied emittance.

For later considerations the envelope model of a drift is needed. The matrix elements are following as

$$C_{11} = 1$$
$$C_{12} = l_{\mathrm{drift}} \qquad \text{or more general} \qquad C_{12} = z$$

and hence ${x_{rms}}^2$ is obtained as

$$ {x_{rms}}^2(z) = {x_{0,rms}}^2 + 2\, x_{0,rms}\ (x_{0,rms})'\ z + \left(\frac{{\epsilon_{rms}}^2}{{x_{0,rms}}^2} + (x_{0,rms})'^2 \right) z^2. \tag{3.7} $$

The envelope equation without space charge effects are often used to fit "quad-scan"/"sol-scan" measurements and to determine the transversal emittances. And indeed, for a low charge bunch it should be a good estimation. But to get a more accurate result it is necessary to include space charge effects into the envelope equation.

3.1.2 Envelope equation with space charge

Space charge effects appear as an additional defocusing force [Sac70]. In the context of this thesis only transversal space charge effects are taken into account. The following model takes a bunch as a homogeneous charged cylinder which does not change its longitudinal length. Furthermore the space charge force is taken as approximatively linear. So that the additional force can be written as [Flö11b, chap.6]

$$ F_x = \frac{e\,Q}{2\,\pi\,\epsilon_0\,L_{\text{lab}}}\,\frac{1}{\gamma^2}\,\frac{x}{4\,{x_{rms}}^2} \tag{3.8} $$

with L_{lab} as the bunch length in the laboratory frame and x_{rms} as the transversal rms beam size.
The largest influence of the space charge force can be noticed at drifts. So the aim is to describe these effects for drift sections. First of all, to include the defocusing force the rms envelope equation has to be found. Starting with 3.4 and differentiate it a second time with respect to the longitudinal direction yields

$$
\begin{aligned}
(x_{rms})'' &= \frac{\partial}{\partial z}\,(x_{rms})' \\
&= \frac{\partial}{\partial z}\left(\frac{\langle x\,x'\rangle}{\langle x^2\rangle^{1/2}}\right) \\
&= \frac{\langle x'^2\rangle}{\langle x^2\rangle^{1/2}} + \frac{\langle x x''\rangle}{\langle x^2\rangle^{1/2}} - \frac{\langle x x'\rangle^2}{\langle x^2\rangle^{3/2}} \\
&\overset{3.5}{=} \frac{{\epsilon_{rms}}^2}{\langle x^2\rangle^{3/2}} + \cancel{\frac{\langle x x'\rangle^2}{\langle x^2\rangle^{3/2}}} - \cancel{\frac{\langle x x'\rangle^2}{\langle x^2\rangle^{3/2}}}^{\,0} + \frac{\langle x x''\rangle}{\langle x^2\rangle^{3/2}} \\
(x_{rms})'' &= \frac{{\epsilon_{rms}}^2}{\langle x^2\rangle^{3/2}} + \frac{\langle x x''\rangle}{\langle x^2\rangle^{3/2}}.
\end{aligned}
\tag{3.9}
$$

A connection to insert the space charge force into the envelope equation can be easily found

$$
x'' = \frac{\ddot{x}}{\beta^2\,c^2} = \frac{F_x}{m_0\,\gamma\,\beta^2\,c^2}. \tag{3.10}
$$

The combination of 3.9 and 3.10 leads directly to the envelope equation for a space charged influenced particle distribution in a drift section:

$$
(x_{rms})'' - \frac{P}{4\,x_{rms}} - \frac{\epsilon^2}{x_{rms}^3} = 0. \tag{3.11}
$$

P is called the generalized perveance and depends on the particle distribution. In case of a homogeneous charged cylinder it writes as

$$
P = \frac{e\,Q}{2\,\pi\,\epsilon_0\,m_e\,c^2\,L_{lab}\,\beta^2\,\gamma^3}.
$$

But nevertheless the envelope equation 3.11 holds independently from the distribution and for a simplified case it has been already solved by K. Flöttmann [Flö11b, chap.6]. He assumed a beam starting with the focus at $z = 0$. This simplifies the whole consideration. This solution will be mentioned again at the end of this section.
If P tends to zero the envelope equation without space charge has to be obtained. Therefore a simple polynomial ansatz, which is similar to the solution without space charge effects (see 3.7), is chosen in order to solve 3.11:

$$x_{rms}(z) = \left(\sum_{n=0}^{N} a_n \, z^n \right)^{1/2} . \tag{3.12}$$

To fulfill the upper condition every a_n for $n > 2$ has to be equal to zero if P tends to zero. That this is fulfilled will be shown in the following.
The first two coefficients can be determined from the initial conditions at $z = 0$:

$$\begin{aligned} x_{rms}(0) &= x_{0,rms} \\ &= \sqrt{a_0} \qquad \Rightarrow \qquad a_0 = {x_{0,rms}}^2 \end{aligned} \tag{3.13}$$

$$\begin{aligned} {x_{rms}}'(0) &= {x_{0,rms}}' \\ &= \frac{\mathrm{d}}{\mathrm{d}z} \left(\sum_{n=0}^{N} a_n \, z^n \right)^{1/2} \Bigg|_{z=0} \\ &= \frac{1}{2} \frac{a_1}{\sqrt{a_0}} \qquad \Rightarrow \qquad a_1 = 2 \, x_{0,rms} \, {x_{0,rms}}'. \end{aligned} \tag{3.14}$$

To determine all other coefficients it is necessary to replace $x_{rms}(z)$ in 3.11 by the chosen ansatz and hence the second derivative of $x_{rms}(z)$ has to be determined

$$\begin{aligned} (x_{rms})'(z) &= \frac{1}{2} \left(\sum_{n=0}^{N} a_n \, z^n \right)^{-1/2} \frac{\mathrm{d}}{\mathrm{d}z} \left(\sum_{n=0}^{N} a_n \, z^n \right) \\ (x_{rms})''(z) &= \frac{1}{2} \underbrace{\left(\sum_{n=0}^{N} a_n \, z^n \right)^{-1/2}}_{{x_{rms}}^{-1}} \underbrace{\frac{\mathrm{d}^2}{\mathrm{d}z^2} \left(\sum_{n=0}^{N} a_n \, z^n \right)}_{({x_{rms}}^2)''} \\ &\quad - \frac{1}{4} \underbrace{\left(\sum_{n=0}^{N} a_n \, z^n \right)^{-3/2}}_{{x_{rms}}^{-3}} \left[\underbrace{\frac{\mathrm{d}}{\mathrm{d}z} \left(\sum_{n=0}^{N} a_n \, z^n \right)}_{({x_{rms}}^2)'} \right]^2 \\ &= \frac{({x_{rms}}^2)''}{2 \, x_{rms}} - \frac{({x_{rms}}^2)'^2}{4 \, {x_{rms}}^3}. \end{aligned} \tag{3.15}$$

With 3.15 the differential equation 3.11 yields

$$\frac{({x_{rms}}^2)''}{2\,x_{rms}} - \frac{({x_{rms}}^2)'^2}{4\,{x_{rms}}^3} - \frac{P}{4\,x_{rms}} - \frac{\epsilon^2}{x_{rms}^3} = 0$$

$$\frac{2\,({x_{rms}}^2)''\,{x_{rms}}^2 - ({x_{rms}}^2)'^2 - P\,{x_{rms}}^2 - 4\,{\epsilon_{x,rms}}^2}{4\,{x_{rms}}^3} = 0$$

$$2\,\left({x_{rms}}^2\right)''\,{x_{rms}}^2 - \left({x_{rms}}^2\right)'^2 - P\,{x_{rms}}^2 - 4\,{\epsilon_{x,rms}}^2 = 0 \tag{3.16}$$

The left-hand side describes a new polynomial with new coefficients b_m

$$\sum_{m=0}^{M} b_m\,z^m = 0 \quad \forall\, z \quad \Rightarrow \quad b_m = 0.$$

At this point it is worthwhile to take a closer look at the terms $({x_{rms}}^2)'' \cdot {x_{rms}}^2$ and $({x_{rms}}^2)'^2$. The derivatives of the sums gain some informations about the degree of this new polynomial and how the coefficients b_m are connected to the original coefficients a_n.

$$\left({x_{rms}}^2\right)'' \cdot {x_{rms}}^2 = \sum_{n=2}^{N} (n-1)\,n\,a_n\,z^{n-2} \cdot \sum_{n=0}^{N} a_n\,z^n \tag{3.17}$$

$$\left({x_{rms}}^2\right)'^2 = \left(\sum_{n=1}^{N} n\,a_n\,z^{n-1}\right)^2 \tag{3.18}$$

The degree of theses two polynomials is

$$\deg\left(z^{N-2}\cdot z^N\right) = 2\,(N-1)$$

and

$$\deg\left(\left(z^{N-1}\right)^2\right) = 2\,(N-1).$$

That means the number of summands is $M = 2\,(N-1)$. Another important fact to know is - under the assumption that a_0 and a_1 are already known: In which b_m does the coefficient a_n arises the first time? In 3.17 a_n appears at $\deg\,(z^{n-2})$ on the other hand in 3.18 the first time at $\deg\,(z^{n-1})$. The consequence is that a_2 is contained in b_0 the first time, a_3 in b_1 and so on. Thus never two unknown coefficients like a_n and a_{n+1} are contained in the same b_m. Besides a_n all "lower" coefficients can appear of course. But this is not a problem. The crucial aspect is that every summand of degree m has to be equal to zero. And hence it is possible to determine the coefficients of the polynomial ansatz (3.12) iteratively.

Two simple examples how to determine a coefficient a_n are shown in the following. Expanding the sums in 3.16 yields the following expressions for b_0 and b_1:

$$\begin{aligned} b_0 &= 4\,{\epsilon_{x,rms}}^2 + 4\,a_2\,a_0 - P\,a_0 - {a_1}^2 \\ b_1 &= 12\,a_3\,a_0 - a_1\,P. \end{aligned}$$

These have to be equal to zero

$$\begin{aligned} & -4\,{\epsilon_{x,rms}}^2 + 4\,a_2\,a_0 - P\,a_0 - {a_1}^2 = 0 \\ \Rightarrow \quad & a_2 = \frac{{\epsilon_{x,rms}}^2}{a_0} + \frac{P}{4} + \frac{{a_1}^2}{4\,a_0} \\ & 12\,a_3\,a_0 - a_1\,P = 0 \\ \Rightarrow \quad & a_3 = \frac{a_1\,P}{12\,a_0}. \end{aligned}$$

Replacing a_0 and a_1 yields

$$\begin{aligned} a_2 &= \frac{{\epsilon_{x,rms}}^2}{{x_{0,rms}}^2} + {(x_{0,rms})'}^2 + \frac{P}{4} \\ a_3 &= \frac{(x_{0,rms})'\,P}{6\,x_{0,rms}}. \end{aligned}$$

As mentioned before, in case of P tends to 0 all coefficients higher than a_2 have to be equal to zero to obtain the envelope model without space charge. Furthermore a_0 to a_2 have to be equal to the corresponding one of 3.7:

$$\left.\begin{array}{rc} a_0 = & {x_{0,rms}}^2 \\ a_1 = & 2\,x_{0,rms}\,(x_{0,rms})' \\ a_2 = & \frac{{\epsilon_{rms}}^2}{{x_{0,rms}}^2} + {(x_{0,rms})'}^2 \\ a_3 = & 0 \\ \vdots & \vdots \\ a_N = & 0 \end{array}\right\} \text{for } P \to 0 \tag{3.19}$$

So the transition between both models is possible.
An essential question remains: Does the model converge? Fig. 3.2 shows a comparison between the two envelope models and an ASTRA[1] simulation. Besides

[1] ASTRA stands for **A** **S**pace Charge **Tr**acking **A**lgorithm [Flö11a] and is a simulation software for all kinds of free particle dynamics.

the analytical approximated model a numerical solution of the differential equation 3.11 is included. The polynomial ansatz for the space charge model is of order $N = 10$. At some point the model diverges from the simulation. Even for much higher order polynomials this happens. But for a "sol-scan" it is not such important. As already mentioned (section 3.1.1) is the envelope model most sensitive to beam size at the minimum which can be precisely described by the analytical model. Therefore the divergence for $z > z_{\min}$ is uncritical.
This model only describes the bunch envelope in a drift for certain initial bunch parameters. To use this model for a "sol-scan" the initial parameters have to be adapted for every solenoid setting. They can be received from the transfer matrix of a solenoid. For the emittance measurements a double solenoid was used. To get a better accordance with ASTRA simulations the double solenoid has been looked upon as a double thin lens (see section 2.4).
Another interesting consideration is the former mentioned simplified solution of 3.11. As well as for the presented analytical solution the same ansatz has been chosen. Under the assumption that the beam starts with the focus at $z = 0$ the envelope slope $(x_{0,rms})'$ is equal to zero. Furthermore it is necessary that the solution is symmetric. In order to fulfill this all terms of odd degree in the polynomial ansatz have to vanish. The solution is much more simple but it describes the problem just for special initial conditions. The analytical solution in this section is a general solution for arbitrary initial conditions but as well as the simple solution it should be symmetrically. In order to prove it the well fitting part of the analytical solution in fig. 3.2 (from $z = 0$ to $z = z_{\min}$) has been taken and flipped vertical at the minimum of the function. This solution is depicted in the figure as the orange curve and it coincides very well with the numerical solution. So the converging part of the analytical solution is symmetrical.

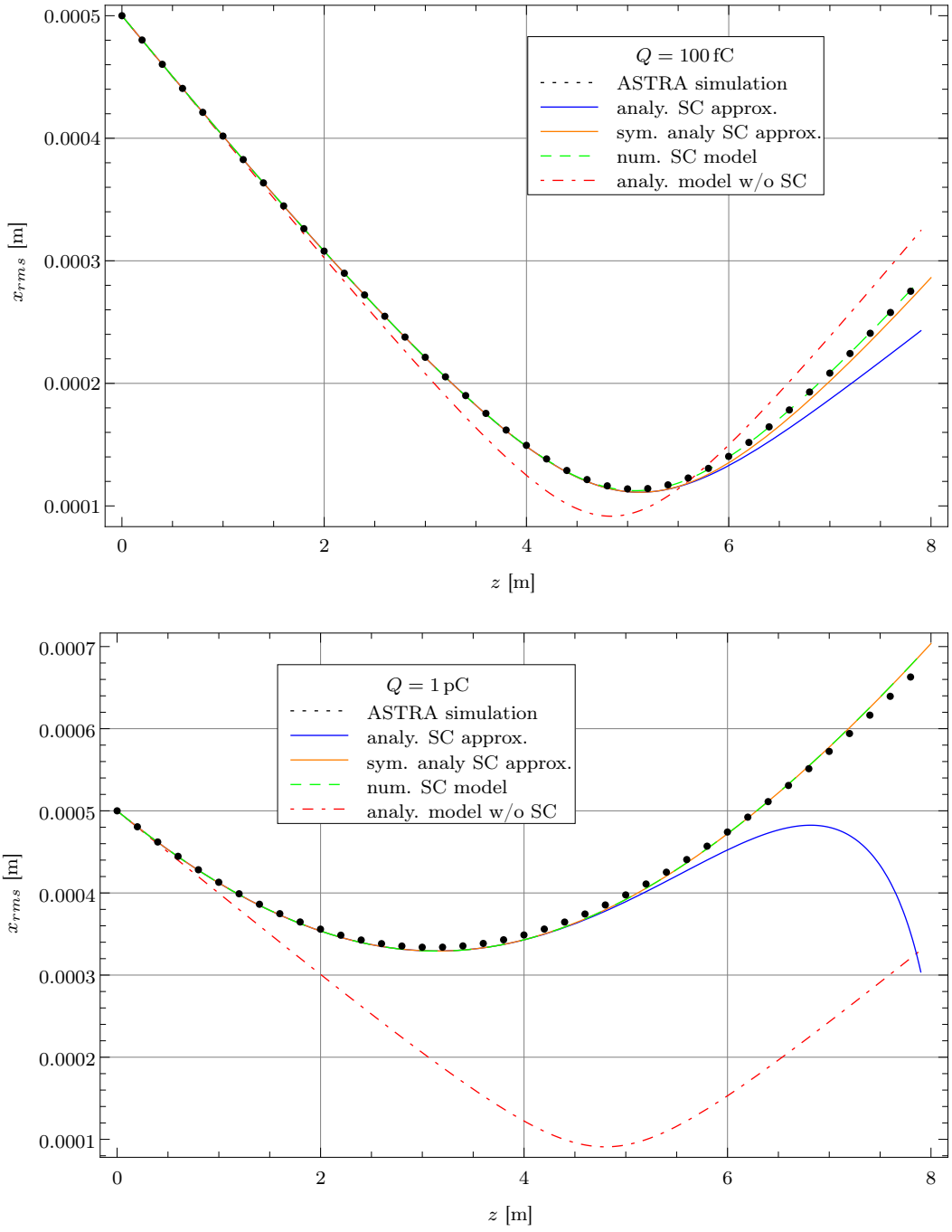

Figure 3.2: Both plots compare an ASTRA simulation with the two models (with (blue) and without (red dotdashed) space charge) of the envelope in a drift. Furthermore a numerical solution (green dashed) of the space charge model and a constructed symmetrical solution (orange) are illustrated. The plots depict the envelope for a 100 fC and 1 pC bunch.

3.1.3 Rotated coordinate system

To evaluate an arbitrary distribution it does not play a role which coordinate system has been chosen. In case of a Cartesian frame the transversal axes are usually horizontal and vertical orientated. But in principle the rotation with respect to the longitudinal axis is a degree of freedom which can be chosen freely.
What consequence does it have for the emittance calculation? As shown in section 2.1 the rotation angle θ changes the calculated rms values. For a spatial distribution like a beam image the change of the rms beam size causes a change of the corresponding emittance. It can be proved that there exists a minimum for the product of both transverse emittances [Flö11b, sec.1.4] and hence it exists a $\theta_{\min}$ which minimize the product of the emittances. Fig. 3.3 illustrates the dependence of the emittance product on the rotation angle θ. This plot is constructed from an emittance measurement from 12th of October at REGAE. 2.5 has been used in order to correct the obtained rms values with respect to all angles between zero and $2\,\pi$.
This minimization problem is 90 degree symmetric and therefore four minima appear. Two of them change the definition of the x- and y-axis. So there are two valid angles which yield the same results.

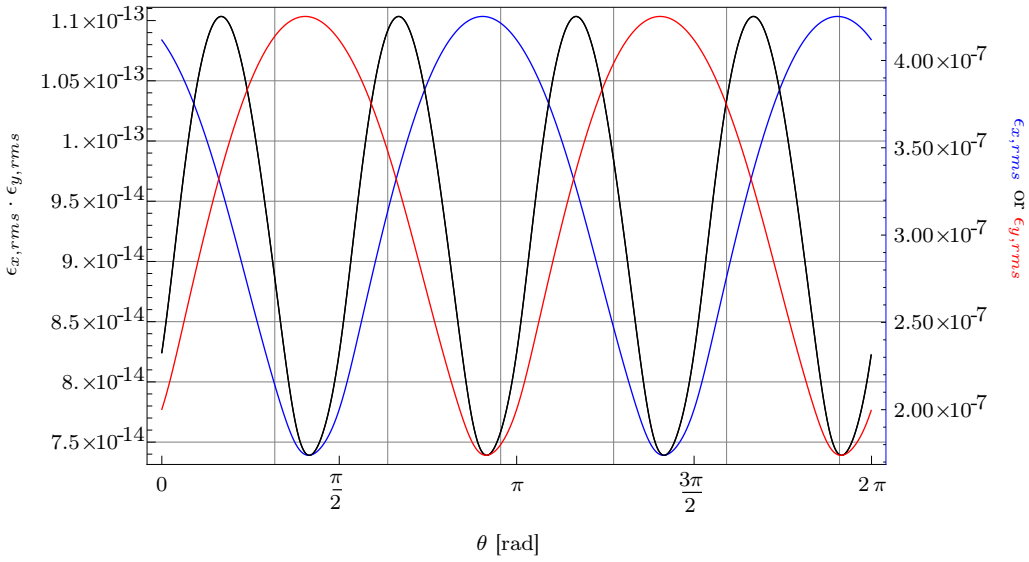

Figure 3.3: The product of the transverse emittances and the single emittances in dependence of the rotation angle θ.

An interesting fact is that the rotation angle of an elliptical shaped beam changes

in the vicinity of a focus. A corresponding simulation is shown in fig. 3.4 and 3.5. The rotation angle changes near the focus rapidly. The assumed rotation angle was 0.3 rad at $z = 0$. So for $z \gg z_{\text{focus}}$ or $z \ll z_{\text{focus}}$ the rotation angle tends to a constant and is in principal measurable at an experiment.

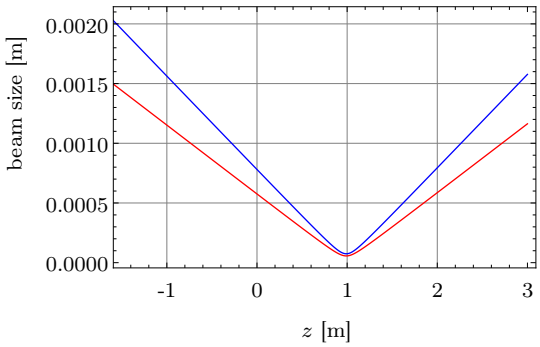

Figure 3.4: Simulation of the transversal beam size development for an elliptical beam profile. blue: x_{rms}, red: y_{rms}.

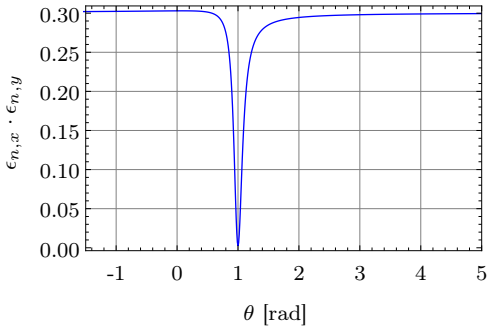

Figure 3.5: Simulation of the rotation angle of a tilted elliptical beam profile in dependence of z.

3.2 Fit methods

For the analyses of "sol-scan" measurements two fit routines have been developed. Both are based on the least-square method. The first is analytic while the second is a numerical algorithm.

3.2.1 Analytical fit method

For the least-square method the sum:

$$\chi^2 = \sum_i^N \left(\frac{f(x_i, \alpha) - y_i}{\sigma_{x,i}} \right)^2 \tag{3.20}$$

has to be minimized. Here, $f(x, \alpha)$ is the fit model, x_i are the measured set points and $\sigma_{x,i}$ is the estimated error of x_i. α stands for the free parameters of the fit model, N is the number of data points and y_i is the measured function value. It is useful to describe the fit routine in a matrix notation. First of all the fit model is written as a vector. Thus the emittance model 3.3 writes as

$$x_{rms}{}^2 = \begin{pmatrix} C_{11}{}^2 & 2\,C_{11}\,C_{12} & C_{12}{}^2 \end{pmatrix}^{\mathrm{T}} \begin{pmatrix} a_1 \\ a_2 \\ a_3 \end{pmatrix} \tag{3.21}$$

with

$$a_1 = x_{0,rms}{}^2 \qquad a_2 = x_{0,rms}\,(x_{0,rms})' \qquad a_3 = \frac{\epsilon_{x,rms}{}^2}{x_{0,rms}} + (x_{0,rms})'^2. \tag{3.22}$$

For a whole set of data points 3.21 results in the matrix equation

$$\begin{pmatrix} (x_{rms}^{(1)})^2 \\ (x_{rms}^{(2)})^2 \\ \dots \\ (x_{rms}^{(N-1)})^2 \\ (x_{rms}^{(N)})^2 \end{pmatrix} = \begin{pmatrix} (C_{11}^{(1)})^2 & 2\,(C_{11}^{(1)})\,(C_{12}^{(1)}) & (C_{12}^{(1)})^2 \\ (C_{11}^{(2)})^2 & 2\,(C_{11}^{(2)})\,(C_{12}^{(2)}) & (C_{12}^{(2)})^2 \\ & \dots & \\ (C_{11}^{(N-1)})^2 & 2\,(C_{11}^{(N-1)})\,(C_{12}^{(N-1)}) & (C_{12}^{(N-1)})^2 \\ (C_{11}^{(N)})^2 & 2\,(C_{11}^{(N)})\,(C_{12}^{(N)}) & (C_{12}^{(N)})^2 \end{pmatrix} \begin{pmatrix} a_1 \\ a_2 \\ a_3 \end{pmatrix}. \tag{3.23}$$

To simplify this equation the column vector on the right-hand side is denoted as $\mathbf{a}$. The $N \times 3$ matrix on the right-hand side is denoted as $\mathbf{B}$ and the column vector on the left-hand side as $\mathbf{\Sigma_x}$. This yields the following simplification:

$$\mathbf{\Sigma_x} = \mathbf{B} \cdot \mathbf{a}. \tag{3.24}$$

In order to get a more precise measurement it is common to average over several values of the same machine set point. The standard deviation σ_{Σ_x} of the measured function values of every set point can be taken into account as a weighting factor in 3.20. This results in

$$\chi^2 = \sum_i^N \frac{1}{\sigma_{\Sigma_x}{}^2} \left((\Sigma_x)_i - \sum_{j=1}^3 B_{ij}\,a_j \right)^2 \tag{3.25}$$

or in a shorter way

$$\chi^2 = \sum_i^N \left((\tilde{\Sigma}_x)_i - \sum_{j=1}^3 \tilde{B}_{ij}\,a_j \right)^2 \tag{3.26}$$

with

$$(\tilde{\Sigma}_x)_i = \frac{\Sigma_x}{\sigma_{\Sigma_x}} \qquad \text{and} \qquad \tilde{B}_{ij} = \frac{B_{ij}}{\sigma_{\Sigma_x}}.$$

Minimizing the derivatives of χ^2 with respect to $\mathbf{a}$ and set them equal to zero yields

$$\begin{aligned} \begin{pmatrix} \partial\chi^2/\partial a_1 \\ \partial\chi^2/\partial a_2 \\ \partial\chi^2/\partial a_3 \end{pmatrix} &= \begin{pmatrix} 2\sum_i^N \sum_j^3 \tilde{B}_{ij}\,\tilde{B}_{i1}\,a_j \\ 2\sum_i^N \sum_j^3 \tilde{B}_{ij}\,\tilde{B}_{i2}\,a_j \\ 2\sum_i^N \sum_j^3 \tilde{B}_{ij}\,\tilde{B}_{i3}\,a_j \end{pmatrix} - \begin{pmatrix} 2\sum_i^N (\tilde{\Sigma}_x)_i\,\tilde{B}_{i1} \\ 2\sum_i^N (\tilde{\Sigma}_x)_i\,\tilde{B}_{i2} \\ 2\sum_i^N (\tilde{\Sigma}_x)_i\,\tilde{B}_{i3} \end{pmatrix} \\ &= \begin{pmatrix} 0 \\ 0 \\ 0 \end{pmatrix}, \end{aligned} \tag{3.27}$$

which can be expressed in matrix notation as

$$\tilde{\mathbf{B}}^{\mathrm{T}}\,\tilde{\mathbf{\Sigma}}_{\mathbf{x}} = (\tilde{\mathbf{B}}^{\mathrm{T}}\tilde{\mathbf{B}})\,\mathbf{a} \tag{3.28}$$

and finally yields an expression for $\mathbf{a}$

$$\mathbf{a} = (\tilde{\mathbf{B}}^{\mathrm{T}}\tilde{\mathbf{B}})^{-1}\,\tilde{\mathbf{B}}^{\mathrm{T}}\,\tilde{\mathbf{\Sigma}}_{\mathbf{x}}. \tag{3.29}$$

If $\tilde{\mathbf{B}}$ and $\tilde{\mathbf{\Sigma}}_{\mathbf{x}}$ are constructed, the free parameters $\mathbf{a}$ are easily accessible.
The absolute value of χ^2 in dependence of $\mathbf{a}$ holds information about the goodness of the fit [Bev69, chap.10]. The reduced χ^2 should be close to one and is defined as

$$\tilde{\chi}^{\mathbf{2}} = \frac{\chi^2}{N-n-1} \tag{3.30}$$

with $N-n-1$ as the number of degrees of freedom where n is the number of free parameters. If $\tilde{\chi}^{\mathbf{2}}$ is larger than one, the fit model and the data points do not correspond well. The other case, $\tilde{\chi}^{\mathbf{2}} < 1$, suggests that the errors where overestimated. In addition to the goodness of the fit the errors of the fitted parameters are interesting. The propagation of errors is presented in the next subsection.

3.2.2 Error estimation for fitted parameters

In the following the propagation of the statistical and systematical errors is presented. In case of a "sol-scan" a spot size measurement over several images can be averaged for the same solenoid setting in order to reduce statistical errors. A fitting parameter g is described by the function $g(x_1, x_2, \ldots, x_n)$ which depends on the defective parameters $X = (x_1, x_2, \ldots, x_n)$. The deviation from the real value of g is given as [Nav06, sec.5.2]

$$\Delta g = \sum_{k=1}^{n} \frac{\partial g}{\partial x_k} \epsilon_k \tag{3.31}$$

with ϵ_k as the deviation of the kth defective parameter from the arithmetical average. Δg_{ij} describes the deviation of the ith solenoid setting and jth measurement at the ith solenoid setting from the real value. In the following is η equal to the number of solenoid settings and ν to the number of measurements per solenoid setting which is for reasons of simplicity equal for every solenoid setting. Thus the standard deviation of Δg_{ij} is defined as

$$\begin{aligned} {\sigma_g}^2 =& \frac{1}{(\eta - n)(\nu - 1)} \sum_{i=1}^{\eta} \sum_{j=1}^{\nu} {\Delta g_{ij}}^2 \\ =& \frac{1}{(\eta - n)(\nu - 1)} \sum_{i=1}^{\eta} \sum_{j=1}^{\nu} \sum_{k=1}^{n} \left(\frac{\partial g}{\partial x_k} \right)^2 {\epsilon_{kj}}^2 \\ &+ \frac{2}{(\eta - n)(\nu - 1)} \sum_{i=1}^{\eta} \sum_{j=1}^{\nu} \sum_{k,l=1, l \neq k}^{n} \frac{\partial g}{\partial x_k} \frac{\partial g}{\partial x_l} \epsilon_{kj}\, \epsilon_{lj} \end{aligned} \tag{3.32}$$

The first part on the right-hand side is the variance of the free parameter g, the second sum describes the correlation between the defective parameters and is called the covariance. $\eta - n$ is the number of degrees of freedom for the measurement of different solenoid settings. In contrast $\nu - 1$ is the number of degrees of freedom for the different measurements per solenoid setting. The sum over j can be exchanges with the sum over k, l. Combined with the ϵ it constructs the sample standard deviation of the measurement and consequently 3.32 simplifies to

$${\sigma_g}^2 = \frac{1}{(\eta - n)} \sum_{i=1}^{\eta} \sum_{k=1}^{n} \left(\frac{\partial g}{\partial x_k} \right)^2 {\sigma_k}^2 + \frac{2}{(\eta - n)} \sum_{i=1}^{\eta} \sum_{k,l=1, l \neq k}^{n} \frac{\partial g}{\partial x_k} \frac{\partial g}{\partial x_l} \sigma_{kl} \tag{3.33}$$

where σ_k and σ_{kl} are defined as

$$\begin{aligned} {\sigma_k}^2 =& \frac{1}{(\nu-1)} \sum_{j=1}^{\nu)} {\epsilon_{kj}}^2 \\ {\sigma_{kl}}^2 \underset{(k\neq l)}{=}& \frac{1}{(\nu-1)} \sum_{j=1}^{\nu} \epsilon_{kj}\epsilon_{lj}. \end{aligned} \tag{3.34}$$

A simpler expression for the propagation of uncertainties can be found with a matrix notation. The indices i, j, k and l are defined as before. The derivatives can be collected in a vector

$$\mathbf{g}^{\mathrm{T}} = \begin{pmatrix} \frac{\partial g}{\partial x_1} & \frac{\partial g}{\partial x_2} & \dots & \frac{\partial g}{\partial x_n} \end{pmatrix}. \tag{3.35}$$

With the definition of the covariance matrix

$$\mathbf{\Sigma}_{kl} = \begin{pmatrix} {\sigma_1}^2 & \sigma_{12} & \dots & \sigma_{1n} \\ \sigma_{21} & {\sigma_2}^2 & \dots & \sigma_{2n} \\ \vdots & \vdots & \ddots & \vdots \\ \sigma_{n1} & \sigma_{n2} & \dots & {\sigma_n}^2 \end{pmatrix} \tag{3.36}$$

follows for 3.33

$${\sigma_g}^2 = \frac{1}{(\eta-n)} \sum_{i=1}^{\eta} {\sigma_{g_i}}^2 = \frac{1}{(\eta-n)} \sum_{i=1}^{\eta} \mathbf{g}^{\mathrm{T}}\, \mathbf{\Sigma}_{kl}\, \mathbf{g}. \tag{3.37}$$

For more than one parameter 3.37 can be written as

$$\frac{1}{(\eta-n)} \sum_{i=1}^{\eta} {\mathbf{\Sigma}_{gg}}^2 = \frac{1}{(\eta-n)} \sum_{i=1}^{\eta} \mathbf{G}\, \mathbf{\Sigma}_{kl}\, \mathbf{G}^{\mathrm{T}}. \tag{3.38}$$

with

$$\mathbf{G} = \begin{pmatrix} \frac{\partial g_1}{\partial x_1} & \frac{\partial g_1}{\partial x_2} & \dots & \frac{\partial g_1}{\partial x_n} \\ \frac{\partial g_2}{\partial x_1} & \frac{\partial g_2}{\partial x_2} & \dots & \frac{\partial g_2}{\partial x_n} \\ \vdots & \vdots & \ddots & \vdots \\ \frac{\partial g_m}{\partial x_1} & \frac{\partial g_m}{\partial x_2} & \dots & \frac{\partial g_m}{\partial x_n} \end{pmatrix}. \tag{3.39}$$

The diagonal of 3.38 contains the standard deviation of the parameters $(g_1, g_2, \ldots, g_m)$. In order to find the error of the mean of g it is necessary to divide 3.38 by the root of $\eta - n$

$$s_g = \frac{\sigma_g}{\sqrt{(\eta - n)}}. \tag{3.40}$$

σ_g is the standard deviation of a parameter g which is constant for η tends to ∞. In contrast s_g describes the error of the mean which tends to zero for $\eta \to \infty$.

3.2.3 Numerical Fit

It is not always possible to fit data with the described analytical least-square method, especially in case of the envelope space charge model, for example when the roots of $\mathrm{d}\chi^2/\mathrm{d}\alpha_j$ are not analytically accessible (compare 3.27). For these cases I have written a numerical algorithm. It based like the analytical one on the least-square method (see 3.20).
The fit algorithm generates a set of parameters α_1 and calculates ${\chi^2}_1$ for a given function $f(x, \alpha)$. Then it slightly differs this setting and calculates ${\chi^2}_2$. If ${\chi^2}_2$ is smaller than ${\chi^2}_1$ the improved parameters are taken as α_1 and the routine is repeated. If ${\chi^2}_2$ is larger than ${\chi^2}_1$, the routine will be repeated with the old α_1 set. The algorithm ends if no smaller χ^2 can be obtained for a defined number of iterations.

Table 3.1: Comparison between the real free parameters and the fitted one. Fitted values are denoted with errors. $\tilde{\chi}^2$ describes the goodness of the fit and should be close to 1.

	f(x)	**fit**
a	0.35	0.3578 ± 0.0009
b	0.71	0.76 ± 0.04
c	0.38	0.38 ± 0.23
$\tilde{\chi}^2$	-	1.00

In order to test the fit algorithm a polynomial test function $f(x)$ has been generated:

$$f(x) = \sqrt{a\,x^2 - a\,b^2\,x + (a\,b - c^2)}. \tag{3.41}$$

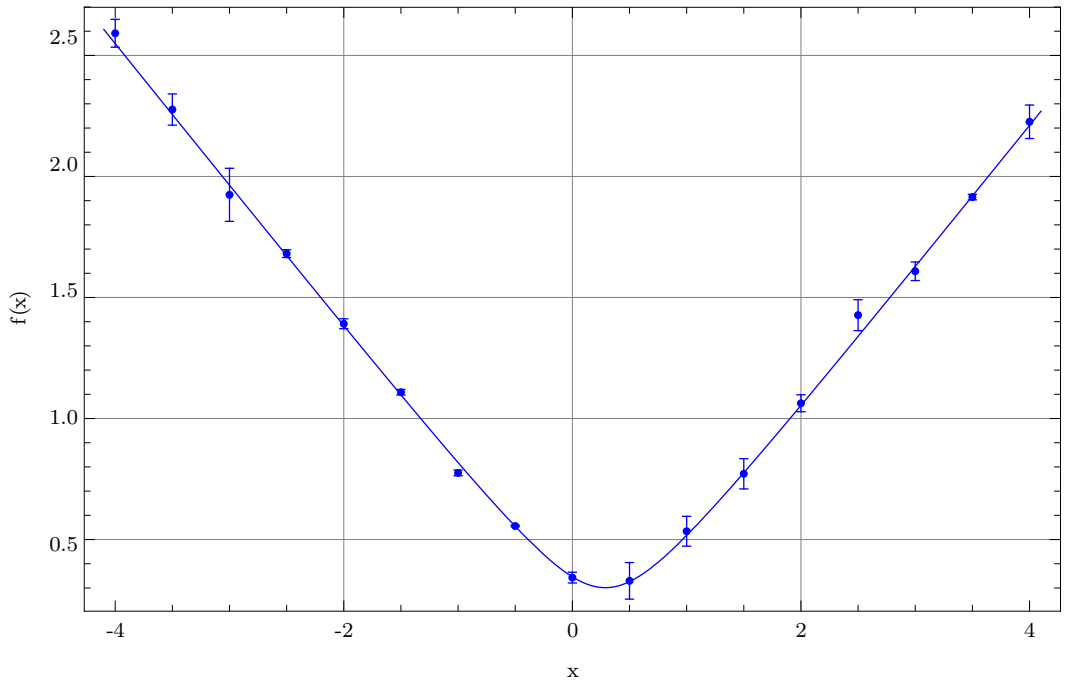

Figure 3.6: Generated data points and error bars of $f(x)$. The fit curve is calculated with the numerical fitting algorithm.

The data points simulate a measurement. For each set point x 10 randomly distributed data points were generated. The averaged values and standard deviation were calculated and illustrated in fig. 3.6. This simulated measurement is reminiscent of the procedure of an emittance measurement. The graphics in fig. 3.7 depict the convergence of (a, b, c) and the simultaneously development of χ^2. $f(x)$ allows to calculate errors for the fitted parameters (a, b, c) with the presented propagation of errors. Because there is only one defective parameter the covariance part of 3.33 can be neglected and the results presented in tab. 3.1 are received. $\tilde{\chi}^{\mathbf{2}}$ close to one suggests a good coincidence of the fit model and the data. A test of 100 runs of the numerical fit algorithm for this problem shows that the algorithm convergences stable to the same values. Fig. 3.8 illustrates an example for the free parameter a. The average over 100 runs yields:

$$\bar{a}_{100} = 0.35218 \pm 0.00001.$$

Thus the algorithm can be used for the emittance fit with space charge and the beam based alignment of a single solenoid (see section 6.4.1).

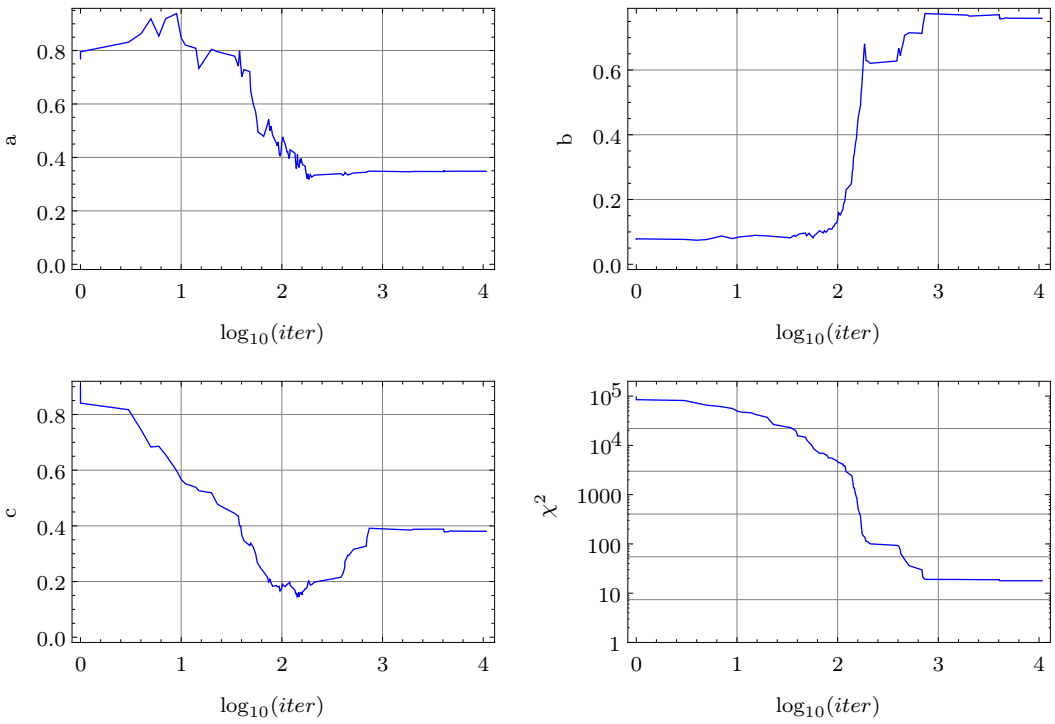

Figure 3.7: Convergence plots for all three parameters (a, b, c) of $f(x)$ and the development of χ^2 against the algorithm iteration number *iter*.

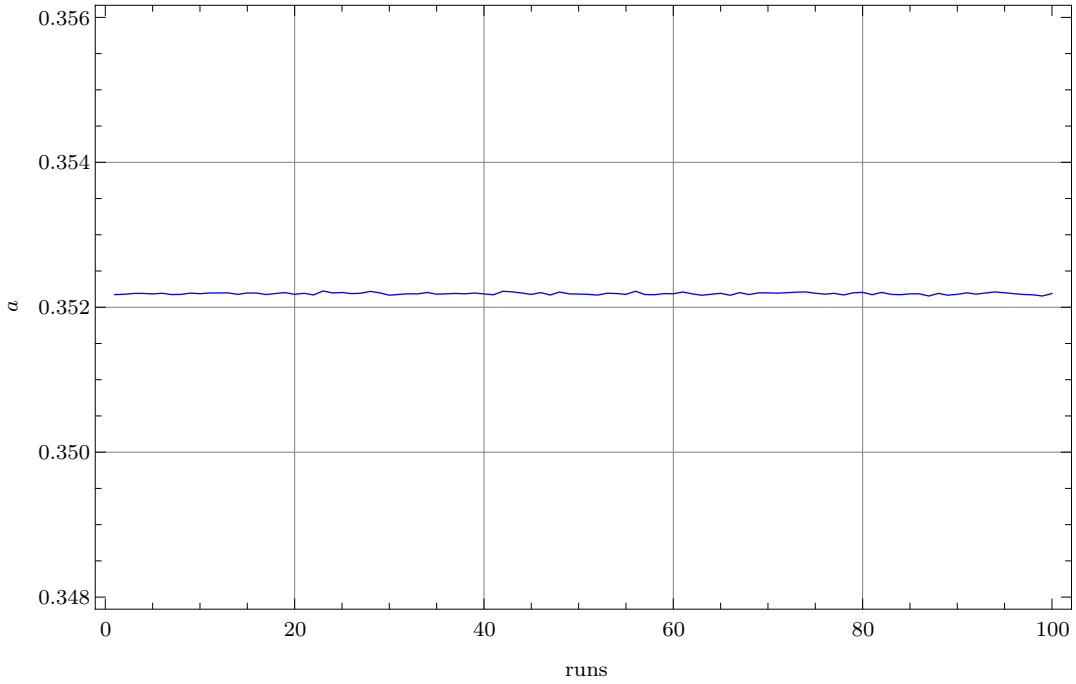

Figure 3.8: 100 runs of the numerical fit algorithm in order to fit the free parameter a. $\bar{a}_{100} = 0.35218 \pm 0.00001$

4

Signal analysis

In order to calculate the rms emittance it is essential to determine the rms beam size. The recorded beam images include in addition to the beam signal a dark current signal and electronic noise caused by the used camera. Both, dark current as well as noise, have to be minimized to evaluate the real beam signal. To handle the dark current background images have to be recorded, averaged and subtracted from a beam image. Besides the beam signal electronic noise remains.
Within the beam profile the beam signal and the noise are always mixed up. To approximate the noise it is necessary to take parts of the image where the beam signal is small. Therefore a region of interest (ROI) has to be defined around the beam spot. The area outside the ROI can be averaged to get a mean noise signal. The next step has to be the subtraction of the noise from the ROI of the image, so that a nearly pure beam signal is acquired and the rms beam sizes ($\langle x^2 \rangle, \langle y^2 \rangle$) and the center of mass positions ($\langle x \rangle, \langle y \rangle$) can be calculated. Without the ROI the rms values would be overestimated due to the noise. Because of the finite number of pixels the sum notation of the first and second moments are used:

$$\langle x^2 \rangle = \frac{\sum_i^N {x_i}^2}{N} - \left(\frac{\sum_i^N x_i}{N} \right)^2 \tag{4.1}$$

and

$$\langle x \rangle = \frac{1}{N} \sum_i^N x_i. \tag{4.2}$$

In case of a tilted elliptical beam shape the determined beam sizes have to be corrected. The true values can be obtained as described in chapter 2.1 and 3.1.3.

4.1 Signal evaluation algorithm for beam images

The upper description of the principal signal analyzing procedure begins with a rough estimate of the beam position. In order to do this a little routine has been developed. It tests the neighborhood of a pixel with the maximal achievable value. The sum of all pixels in the direct neighborhood have to exceed a defined threshold in order to identify this region as a possible beam candidate. If this is not the case this region of the image is set to zero and the routine starts again till a point is found which fulfills the condition. This coordinate is the starting point where the beam size algorithm starts.
The algorithm [Löh05] is divided in four parts:

1. Subtract the averaged background image from the beam image.

2. Start with a circular ROI with the former determined starting point as the center. Choose a small radius like $r = 10\,\text{pixel}$. Calculate the noise outside the ROI and subtract it from the ROI.

3. Determine the first and second moment inside the ROI (4.1/4.2).

4. Use the first moments to define the new center. Define the new half-axes of the ROI-ellipse (a_x and a_y) by the product the second moment and the enlargement factor c ($a_x = c \cdot \langle x^2 \rangle$ and $a_y = c \cdot \langle y^2 \rangle$).

Repeat step 1 to 4 till ($\langle x^2 \rangle$,$\langle y^2 \rangle$) converge. The final step is to correct the beam tilt. Besides the second moments the correlation between x and y is required to correct a possible tilt of the beam ellipse:

$$\langle x\, y \rangle = \frac{\sum_i^N x_i\, y_i}{N} - \frac{\sum_i^N x_i \sum_i^N y_i}{N^2}. \tag{4.3}$$

For the correction of a whole measurement the presented routine in section 3.1.3 is available. These received moments of the measured distribution can be used to determine the transversal emittance (second moment) or for all kinds of beam based alignment issues (first moment).

4.1.1 Signal evaluation algorithm test

In order to cross check the algorithm a beam image with well known rms beam sizes and a defined rotation angle has been generated (fig. 4.1). Furthermore some random noise is added. The results from the algorithm are tabled in tab. 4.1. The good agreement of the calculated and the real values proves that the algorithm works as expected.

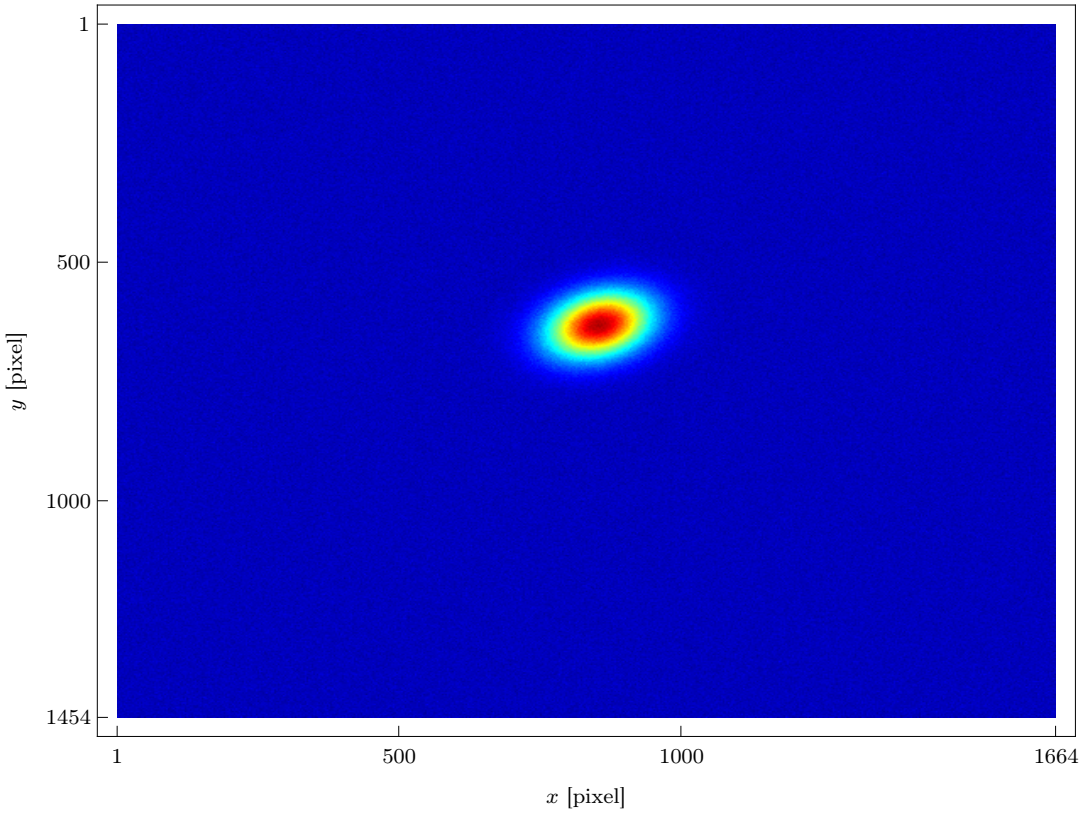

Figure 4.1: Simulated beam signal with random noise. $\sigma_x = 65\,\text{pixel}$, $\sigma_y = 45\,\text{pixel}$ and $\theta = 0.349\,\text{rad}$

.

Table 4.1: Test of the signal analyzing algorithm

	real values	**calc. values**
$\sigma_\mathbf{x}$ [pixel]	65	65.03
$\sigma_\mathbf{y}$ [pixel]	45	44.98
θ [rad]	0.349	0.342

4.2 *rms beam size* error due to the calculation algorithm

With the signal evaluation algorithm, it is necessary to define a ROI to calculate the rms beam size. In case of a distribution with long tails a part of the beam gets lost. But what is the deviation from the real rms beam size?
For an assumed Gaussian beam profile it is possible to determine this deviation. First of all the fraction P of the beam which lies inside the ROI has to be determined [Com94]. Therefore it is essential to switch to polar coordinates in order to calculate following integrals. The ROI is an ellipse so the integral limits have to be adapted. For polar coordinates the following ellipse's equation holds

$$\begin{aligned} \varrho(\theta) &= \frac{a_x \cdot a_y}{\sqrt{(a_y \cdot \cos\theta)^2 + (a_x \cdot \sin\theta)^2}} \\ &= \frac{c}{\sqrt{\frac{\cos^2\theta}{{\sigma_x}^2} + \frac{\sin^2\theta}{{\sigma_y}^2}}} \end{aligned} \tag{4.4}$$

with a_x and a_y as the half axes of the ellipse which are multiples of the standard deviation σ_s

$$a_x = c \cdot \sigma_x \qquad\qquad a_y = c \cdot \sigma_y.$$

c is the so called enlargement factor.
The normalized Gaussian distribution is a probability density function (PDF). Integrated from $-\infty$ to ∞ it is equal to one. So the integral of the PDF over the ROI is the fraction P of the beam that lies inside. The 2-dimensional PDF of a centered Gaussian profile is defined as

$$f(x,y) = \frac{1}{2\pi\sigma_x\sigma_y}\, e^{-\frac{x^2}{2{\sigma_x}^2}}\, e^{-\frac{y^2}{2{\sigma_y}^2}}. \tag{4.5}$$

In polar coordinates it can be written as

$$\begin{aligned} f(x,y) &= \frac{1}{2\pi\sigma_x\sigma_y}\, e^{-\frac{(r\cdot\cos\theta)^2}{2\sigma_x}}\, e^{-\frac{(r\cdot\sin\theta)^2}{2\sigma_y}} \\ &= \frac{1}{2\pi\sigma_x\sigma_y}\, e^{-\frac{r^2}{2}\left(\frac{\cos^2\theta}{\sigma_x^2}+\frac{\sin^2\theta}{\sigma_y^2}\right)} \\ &= \frac{1}{2\pi\sigma_x\sigma_y}\, e^{-\frac{c^2 r^2}{2\,\varrho(\theta)^2}}. \end{aligned} \tag{4.6}$$

With the results from 4.4 and 4.6 it is possible to find an expression for P:

$$\begin{aligned} P &= \frac{1}{2\pi\sigma_x\sigma_y} \int_0^{2\pi} \int_0^{\varrho(\theta)} r\, e^{-\frac{c^2 r^2}{2\,\varrho(\theta)^2}}\, \mathrm{d}\theta \\ &= \frac{1}{2\pi\sigma_x\sigma_y} \int_0^{2\pi} (1 - e^{-\frac{c^2}{2}})\, \frac{\varrho(\theta)^2}{c^2}\, \mathrm{d}\theta \\ &= 1 - e^{-\frac{c^2}{2}}. \end{aligned} \tag{4.7}$$

But P describes only the fraction of a bunch that lies inside the ROI. The next step is to find an expression for the relative error of the calculated rms beam size and the real one. The second moment simplifies for a centered distribution to

$$x_{rms}^2 = \frac{\int x^2\, f(x,y)\, \mathrm{d}x\, \mathrm{d}y}{\int f(x,y)\, \mathrm{d}x\, \mathrm{d}y}. \tag{4.8}$$

Hence the second moment inside a ROI can be expressed as

$$\begin{aligned} x_{rms}^2 =& \frac{1}{2\pi\, \sigma_x\sigma_y\, (1 - e^{-\frac{c^2}{2}})} \int_0^{2\pi} \int_0^{\varrho(\theta)} r^3\, \cos^2\theta\, e^{-\frac{c^2 r^2}{2\,\varrho(\theta)}}\, \mathrm{d}r\, \mathrm{d}\theta \\ =& \frac{1}{P} \frac{e^{-\frac{c^2}{2}} (2\, e^{\frac{c^2}{2} - 2 - c^2}) \sigma_x^2}{2} \\ =& \frac{1}{P} \left[\left(1 - e^{-\frac{c^2}{2}}\right) - \frac{c^2}{2}\, e^{-\frac{c^2}{2}} \right] \sigma_x^2 \\ =& \frac{1}{P} \left(P - \frac{c^2}{2}\, e^{-\frac{c^2}{2}} \right) \sigma_x^2. \end{aligned} \tag{4.9}$$

Based on this result the relative error of the real rms beam size and the measured one is

$$\frac{x_{rms}^2}{\sigma_x^2} = \frac{P - \frac{c^2}{2}\, e^{-\frac{c^2}{2}}}{P} \tag{4.10}$$

which is plotted in fig. 4.2.

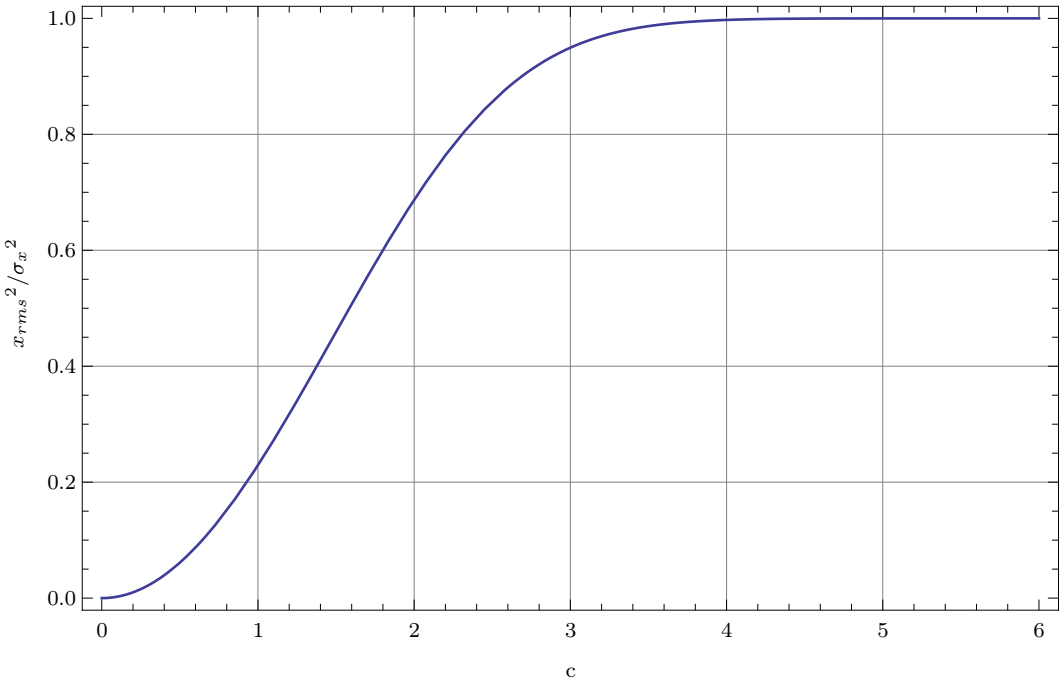

Figure 4.2: The relative error of the measured beam size and the real one against the enlargement factor c

.

Table 4.2: The relative error of a beam size measurement and the beam fraction inside the ROI for different enlargement factors c.

c	$\mathbf{x^2_{rms}/\sigma^2_x}$	**P**
1	0.2293	0.3935
2	0.6870	0.8647
3	0.9494	0.9889
4	0.9973	0.9996
5	1.0000	1.0000

The relative error x^2_{rms}/σ^2_x and the detected fraction of the beam P are compared in tab. 4.2. If c is too small most of the distribution tails get cut off what yields a huge error. Thus c should be greater than 4 to reach an acceptable coincidence between the real value and the measured one. For c equal to 5 the signal evaluation algorithm does not converge every time. So $c = 4$ has been used with an acceptable relative error of $\sim 0.3\,\%$.

5

Experimental setup

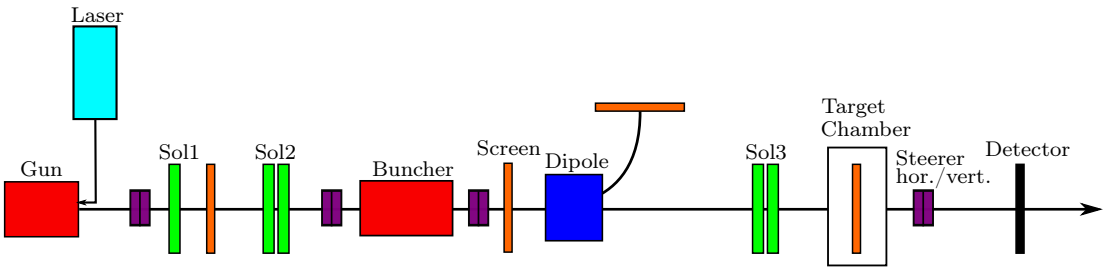

Figure 5.1: Sketch of beam optical elements of the REGAE accelerator.

5.1 Diagnostic at REGAE

This section is based on work of H. Delsim-Hashemi [DH12]. At REGAE indirect methods for the measurement of transversal particle distribution are in use. In fig. 5.1 the position of different screens are indicated. These screens are scintillators which emit fluorescence light when an electron bunch hit them. Instead of materials like YAG[1] they are made of a LYSO[2] crystal which has a higher luminosity that means more photons per electron are emitted. REGAE is designed to operate at a very low bunch charge ($\sim 100\,\mathrm{fC}$), therefore, in addition to normal CCD[3] cameras an ICCD[4] camera system is installed for every diagnostic station

[1] Cerium activated Yttrium Aluminum Garnet
[2] Cerium-doped Lutetium Yttrium Orthosilicate
[3] Charge-coupled device
[4] Intensified charge-coupled device

in order to detect the light emission of low charged electron bunches. The screens are installed under 45 degree towards the beam propagation and the CCD/ICCD camera systems. The exposure time is in the range of $\sim 70\,\mu$s. A short exposure time allows to reduce the detected noise in order to improve the signal-noise-ratio. In case of the CCD system a spatial resolution of $\sim 5\,\mu$m/pixel is accessible while for the ICCD system it is limited to $\sim 10\,\mu$m/pixel.
For the diffraction experiment a high charge sensitivity detector is installed which is able to detect single electrons. This detector has been also used for the emittance measurements presented in section 7. In contrast to the other diagnostic stations it contains a CsI-crystal-screen which is evaporated onto light guides (see 5.2) which indeed improve the spatial resolution but nevertheless it is limited to $\sim 20\,\mu$m/pixel. This is due to the setup of the detector. It is designed for a high sensitivity at cost of spatial resolution. The screen is called fiber optics scintillator (FOS). The schematic layout of the detector is shown in fig. 5.3. The FOS is orientated perpendicular to the beam propagation. To avoid γ-photons or electrons on the EMCCD[5] camera of the detector a mirror reflects the visible light emitted by the FOS under 90 degree in direction of the camera. In addition to this special geometry two Aluminum covers are installed in order to reduce the background signal and improve the detection sensitivity. One, directly layered on the FOS, reflects the emitted visible light back in direction of the mirror and improves the sensitivity. The second isolates the detector setup from the rest of the accelerator in order to reduce noise caused by diffuse light. The EMCCD is cooled down to -70° C to reduce electronic noise. All these factors increase the charge sensitivity by a factor in the order of 1000 compared with a standard CCD and LYSO combination.
The low charge sensitivity has been tested with a radioactive source ($^{137}_{55}$Cs). With the activity of $^{137}_{55}$Cs and a known exposure time the number of expected electrons can be estimated. Fig. 5.4 illustrates the FOS image for 5 s exposure of the EMCCD. About 10^6 electrons were expected to be emitted in forward direction. About $5 \cdot 10^5$ pixels had a signal. Assuming the coupling efficiency of the collecting optics and the distance between the FOS and source nearly every electron were detected. A former background measurement yielded only 10 pixel with a signal for 5 s exposure time. So the noise level is extremely low.
The advantage of this detector compared to the CCD and ICCD systems is the low noise level and the high charge sensitivity.

[5] Electron multiplying charge-coupled device

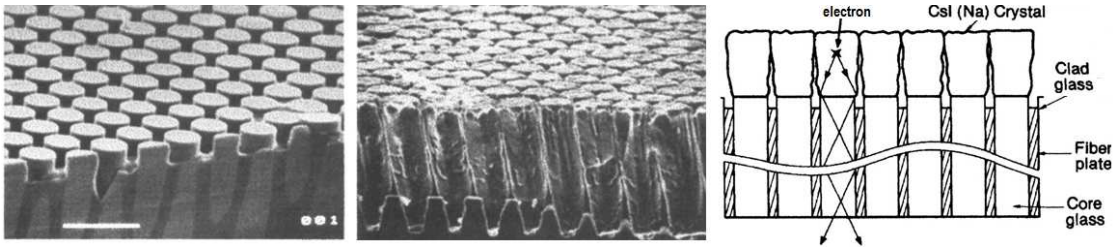

Figure 5.2: Fiber optics scintillator (FOS) [figure by courtesy of H. Delsim-Hashemi].

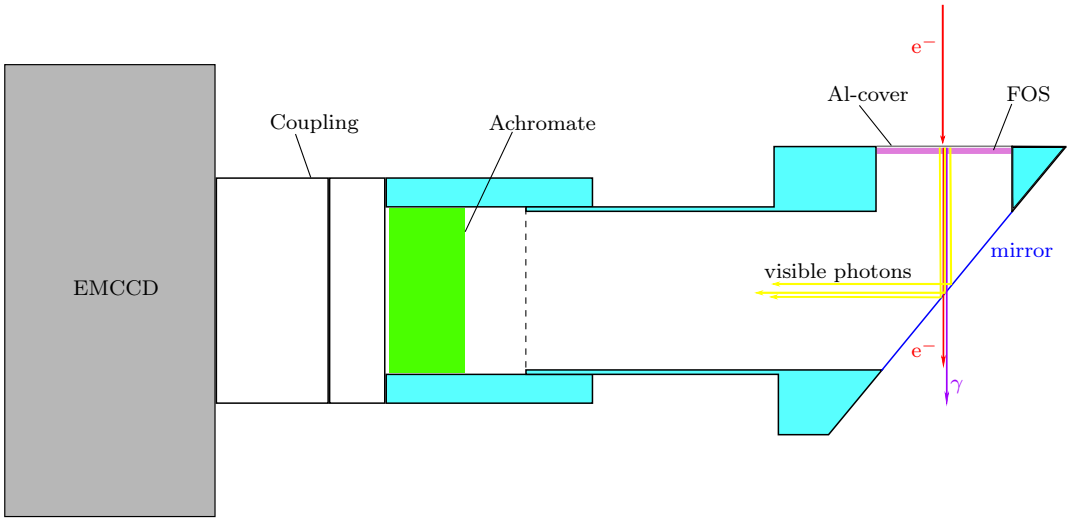

Figure 5.3: Layout of the REGAE detector.

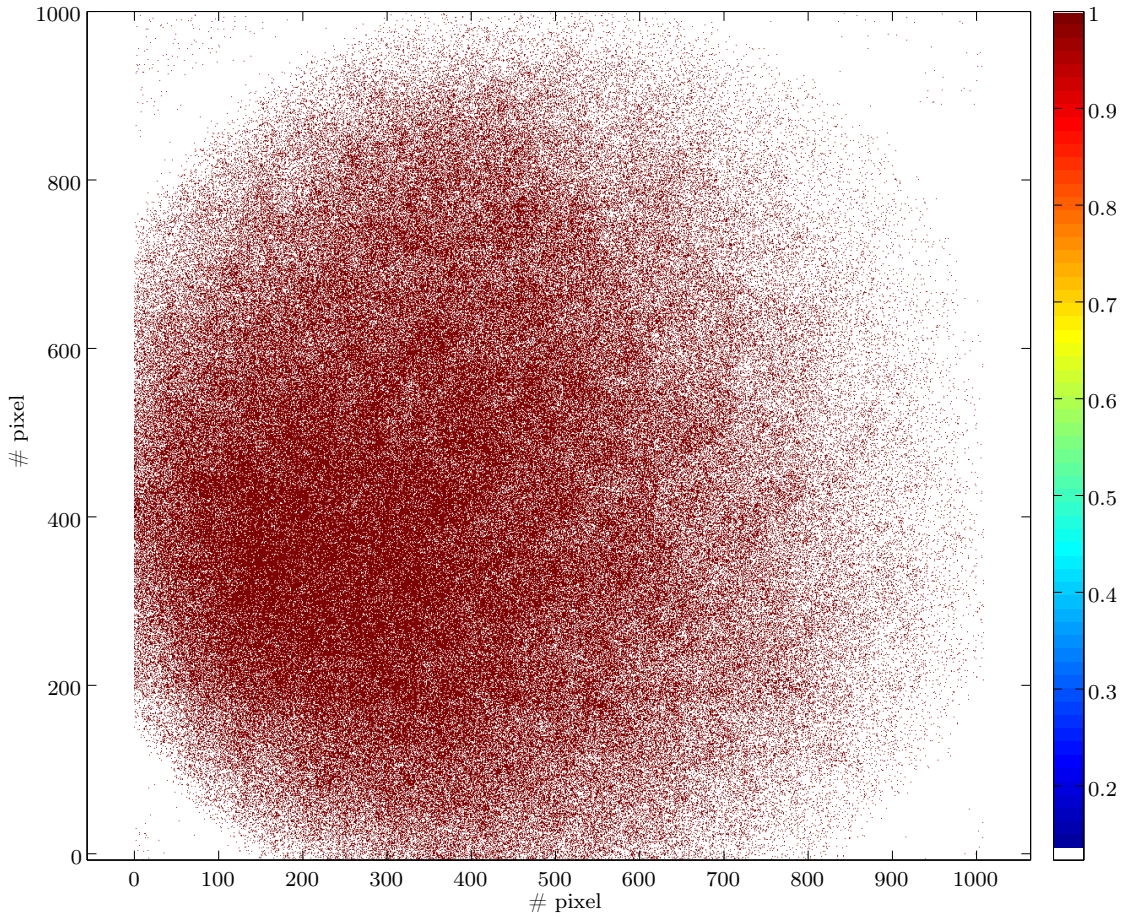

Figure 5.4: Calibration of the REGAE detector with a $^{137}_{55}$Cs source [figure by courtesy of H. Delsim-Hashemi].

5.2 Setup of an emittance measurement

For the emittance measurement a solenoid and a screen are required. Between those the beam should only drift and no other beam optical element should interfere with the beam to keep the fit model simple. Thus there are different combinations to do a "sol-scan" at REGAE. During this thesis it was not possible to adjust the buncher phase independently from the gun phase. To avoid unpredictable influences by the buncher it was detuned. Detuning means that the resonance condition is changed by heating up the buncher so that no RF signal can couple in.
Besides the emittance $\epsilon_{x,rms}$ two more initial beam parameters $(x_{0,rms}, (x_{0,rms})')$ appears in the envelope equation of 3.6. The control of these two values is very important to guarantee the feasibility of the emittance fit routine. The emittance contributes only in one term to the rms beam size calculation:

$$\left(\frac{{\epsilon_{rms}}^2}{{x_{0,rms}}^2} + {(x_{0,rms})'}^2 \right) z^2.$$

This suggests a mathematical criterion for the three free parameters of the envelope equation to make an emittance measurement possible:

$$\begin{aligned} \frac{{\epsilon_{rms}}^2}{{x_{0,rms}}^2} &\geq 0.01\, {(x_{0,rms})'}^2 \\ \frac{{\epsilon_{rms}}^2}{{x_{0,rms}}^2\, {(x_{0,rms})'}^2} &\geq 0.01. \end{aligned} \tag{5.1}$$

0.01 is a compromise and has been proven in simulations. If the fraction is too small it is difficult to get an exact result for the emittance because it is too small in comparison to the source size $x_{0,rms}$ and the envelope slope $(x_{0,rms})'$. So the initial beam parameters need some tuning to enable an emittance measurement.
Another important aspect is that it is required to focus the beam down onto the screen because the "sol-scan" method is really sensitive to the beam size at the minimum of the beam envelope (see end of sec. 3.1.1). This fact leads to two new criteria for the initial beam parameters. If the focus lies in front of the screen even when the solenoid is off, it is obvious that there is no way to get the focus on the screen. The question is: How small can the envelope slope $(x_{0,rms})'$ be so that the focus still lies behind the screen? The answer can be given by differentiating the envelope equation (3.7) with respect to z to find the focus position. The center of

the solenoid is at $z = 0$ and l_d is the distance between the center of the solenoid and the screen.

$$\frac{\mathrm{d}{x_{rms}}^2}{\mathrm{d}z} = 2\,x_{0,rms}\,(x_{0,rms})' + 2\,z\left(\frac{{\epsilon_{x,rms}}^2}{{x_{0,rms}}^2} + (x_{0,rms})'^2\right) \stackrel{!}{=} 0$$

$$\Rightarrow \qquad z = \frac{x_{0,rms}\,(x_{0,rms})'}{\frac{{\epsilon_{x,rms}}^2}{{x_{0,rms}}^2} + (x_{0,rms})'^2} \tag{5.2}$$

Depending on the initial slope of the envelope there is a maximum position for the focus. The derivative with respect to $(x_{0,rms})'$ yields z_{max}.

$$\frac{\mathrm{d}z}{\mathrm{d}(x_{0,rms})'} = -\frac{x_{0,rms}}{\frac{{\epsilon_{x,rms}}^2}{{x_{0,rms}}^2} + (x_{0,rms})'^2} + 2\,\frac{x_{0,rms}\,(x_{0,rms})'^2}{\left(\frac{{\epsilon_{x,rms}}^2}{{x_{0,rms}}^2} + (x_{0,rms})'^2\right)^2} \stackrel{!}{=} 0$$

$$-x_{0,rms}\left(\frac{{\epsilon_{x,rms}}^2}{{x_{0,rms}}^2} + (x_{0,rms})'^2\right) + 2\,x_{0,rms}\,(x_{0,rms})'^2 = 0$$

$$\Rightarrow \qquad (x_{0,rms})'^2 = \frac{{\epsilon_{x,rms}}^2}{{x_{0,rms}}^2}$$

$$(x_{0,rms})' = \pm\frac{\epsilon_{x,rms}}{x_{0,rms}} \tag{5.3}$$

The different signs for the result correspond to a focus position in front of the solenoid ($z < 0$) and behind the solenoid ($z > 0$). A focus position behind the solenoid is the only interesting case. Therefore, introducing 5.3 into 5.2 yields

$$z_{\max} = \frac{{x_{0,rms}}^2}{2\,\epsilon_{x,rms}} \tag{5.4}$$

The opposite case is a divergent incoming beam. If the divergence is too large, it is not possible to focus the beam down onto the screen. So the next criterion depends on the maximum focusing strength of the solenoid in use. Again starting with the envelope equation but instead of a simple drift a combination of a thin lens approximation for the solenoid and a drift can be used. The matrix elements C_{11} and C_{12}, which correspond to the transfer matrix, are functions of z. To find the focus position 3.6 has to be differentiated with respect to z and the resulting

equation has to be solved for z:

$$z = \frac{x_{0,rms}\left(\frac{x_{0,rms}}{f_{max}} - (x_{0,rms})'\right)}{{f_{max}}^2\left(\left(\frac{x_{0,rms}}{f_{max}} - (x_{0,rms})'\right)^2 + \frac{{\epsilon_{x,rms}}^2}{{x_{0,rms}}^2}\right)}. \tag{5.5}$$

The expression in the braces can be called the effective envelope slope right behind the solenoid:

$$(x_{\text{eff},rms})' = -\left(\frac{x_{0,rms}}{f_{max}} - (x_{0,rms})'\right)$$

which simplifies the upper equation and determine the minimum distance between a solenoid and a screen in order to perform an emittance measurement:

$$z_{\min} = -\frac{x_{0,rms}\,(x_{\text{eff},rms})'}{{f_{max}}^2\left((x_{\text{eff},rms})'^2 + \frac{{\epsilon_{x,rms}}^2}{{x_{0,rms}}^2}\right)}. \tag{5.6}$$

5.4 and 5.6 can be formulated as an upper and lower limit of the drift length l_d in dependence on the initial beam parameters and the maximum focusing strength:

$$-\frac{x_{0,rms}\,(x_{\text{eff},rms})'}{{f_{max}}^2\left((x_{\text{eff},rms})'^2 + \frac{{\epsilon_{x,rms}}^2}{{x_{0,rms}}^2}\right)} \leq l_d \leq \frac{{x_{0,rms}}^2}{2\,\epsilon_{x,rms}}. \tag{5.7}$$

This criterion defines conditions for the initial beam parameters and the experimental geometry. The criterion of 5.1 is an additional limit for the initial beam parameters and is based on the mathematical limits of an emittance fit. If both criteria are fulfilled, there is no obstacle to an emittance measurement.

6

Beam based alignment

Why is it important to align beam optical elements? There are several related reasons. First of all there is a very practical reason. It is much more easy to work with an accelerator when the beam does not move transversally if one changes the focusing strength of a solenoid. Another related reason follows from the necessity to detect the complete beam if the beam size is going to be determined as in case of an emittance measurement. If the beam moves during a solenoid scan towards the edge of the screen a fraction of the beam signal might get lost and the signal analysis as described in section 4 might be incorrect. In principle this could also be corrected by varying steerer settings during a scan but aligning the focusing elements is the most general solution.
If the beam is taken as a point charge which has an offset related to the solenoid symmetry axis, the whole beam gets deflected in accordance to the focusing strength. Even when the focusing strength of a solenoid is constant, the deflection of a solenoid depends on the beam energy as well. These reasons make it difficult to operate the machine for different settings while the focusing elements are not aligned.

6.1 Cathode laser alignment

Electrons at REGAE are emitted right inside the RF gun at a photo cathode. The gun cavity is a defocusing element, thus the electrons leave the cavity with an angle if they are not emitted at the electrical center. The exit angle depends on the field amplitude. Because the electron bunch itself defines the principal axis of

the whole machine the laser alignment on the cathode is a really crucial issue for the beam based alignment of the complete machine.

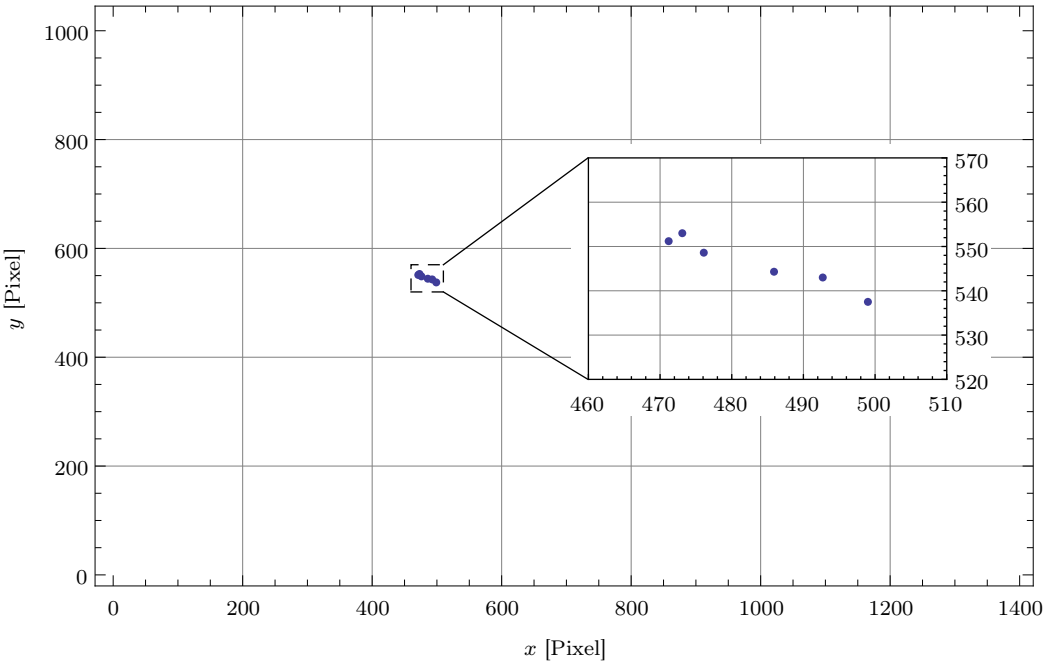

Figure 6.1: Beam position on DDC1 for different gun gradients after aligning the leaser beam onto the photo cathode.

If varying the gun amplitude causes a transversal beam motion, it easily indicates whether the laser is aligned or not. The laser position has to be corrected till the beam position on the screen becomes independent on the gun setting. Fig. 6.1 and 6.2 illustrate the beam position after the laser alignment. It is good enough to operate the machine for a large variation of the gun gradient. The variation of the beam position is well below the transverse beam size

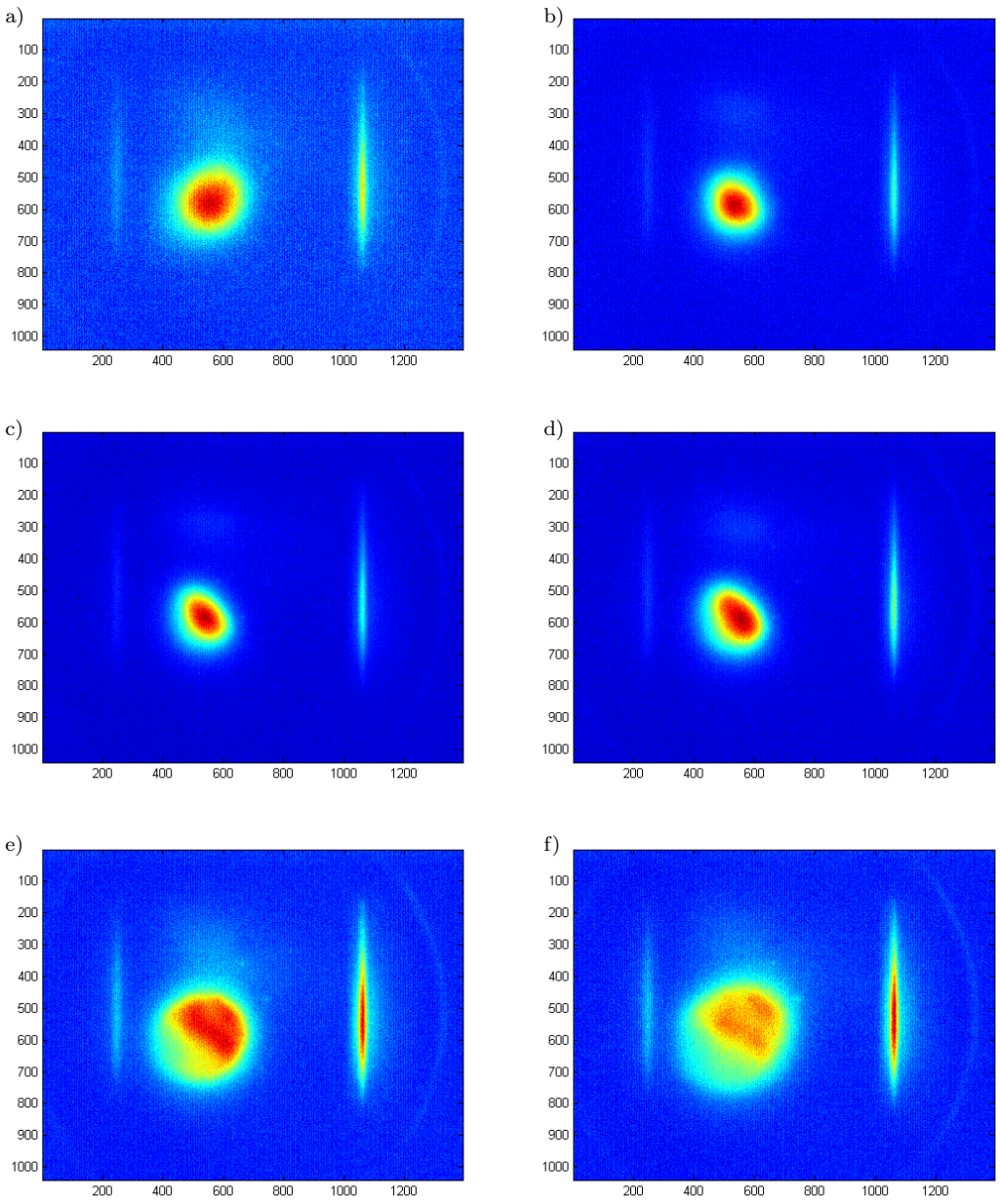

Figure 6.2: Beam position on DDC1 corresponding to different gun gradients.

6.2 Beam energy measurement

The mean beam energy is not only important for the following beam based alignment issues but also for the emittance measurements. As the measurements of the

beam size in the context of the emittance measurements will show (see chap. 7), its statistical error is really small and so the mean beam energy error is a crucial factor which can falsify the emittance determination if it is not measured with an acceptable accuracy. In the following two methods to measure the mean beam energy at REGAE are introduced.

6.2.1 Dipole spectrometer

For the measurement of the beam energy a dipole spectrometer is installed at REGAE. It is placed after the buncher cavity. Besides the normal statistical errors caused by RF instabilities, a not fully aligned beam can cause errors of the mean beam energy. If a bunch has an offset or tilt related to the design trajectory of the machine, it hits the spectrometer screen not at the center.
The procedure of a beam energy measurement is to deflect the beam onto the center of the screen and to calculate the energy in dependence of the dipole current. A misaligned beam is indeed deflected onto the center of the screen so that the measured dipole current yields a wrong beam energy. For an estimated maximum offset of 3 mm and a maximum correlated beam divergence of 3 mrad the relative error for the REGAE spectrometer is

$$\sigma_{rel,E_{kin}} = 0.0071 \cdot E_{kin}.$$

The contour plot of fig. 6.3 illustrates the relative error for the two dimensional parameter space (x_0, x_0'). The color code emphasizes the absolute value of the relative error in dependence on the transversal offset x_0 and divergence x_0'. Unfortunately it is not possible to measure these beam parameters accurately thus they have to be estimated and a systematical error of approximately 0.5 % has to be assumed.

6.2.2 Steerer scan method

Steerers are installed at every crucial positions along the beam line in order to correct the beam position. The steerers themselves create a short approximatively homogeneous magnetic field. In this way an additional transversal kick is introduced to a passing particle. While the transversal momentum is changed right at a steerer, the transversal particle position stays constant. The change of the transversal position is reached in the following drift section. The dependence of the transversal kick on the particle energy makes these elements interesting for a energy measurement. Therefore a simplified theoretical model to determine the mean beam energy by scanning the deflection of the beam with respect to the

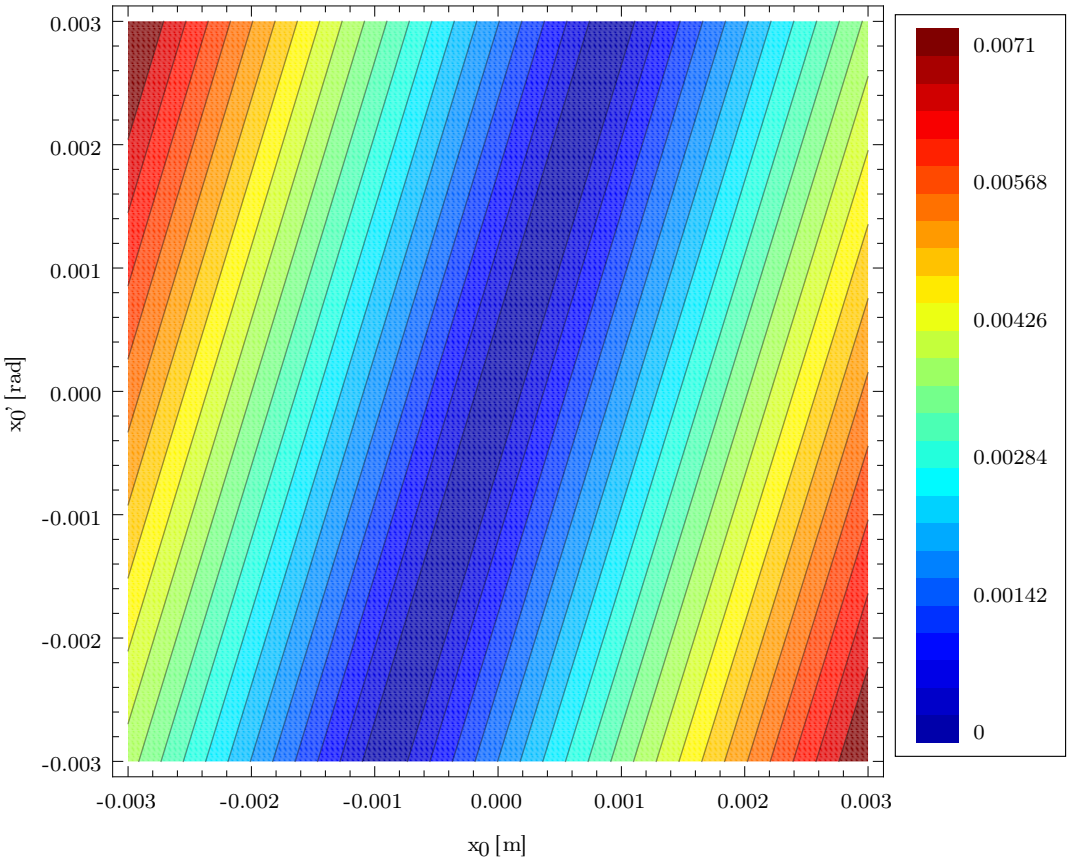

Figure 6.3: Beam energy error for non-zero transversal starting values $(x_0, x_0^{'})$. The color map indicates the relative error of the beam energy.

steerer current will be introduced.
Starting with the Lorentz force the relation between the induced deflection and

the steerer current is yielded:

$$\begin{aligned} \frac{dp_y}{dz} &= \frac{e\,p_z}{\gamma\,m_e\,\beta_z\,c}\,B_x(J) \\ \Rightarrow \qquad p_y &= \underbrace{\frac{e\,p_z}{\gamma\,m_e\,\beta_z\,c}}_{=p_z}\,\underbrace{\int B_x(J)\,dz}_{=Int_{St}(J)} \\ y' &= \frac{p_y}{p_z} = \frac{\Delta y}{l_D} \\ \Rightarrow \qquad \Delta y &= \frac{e\,l_D}{p_z}\,Int_{St}(J) \end{aligned} \tag{6.1}$$

with Δy as the transversal deflection, l_D as the drift length between the steerer center and the detection screen and J as the steerer current. The integrated magnetic field has been determined for the REGAE steerers to be $Int_{St}(J) = J \cdot 7.64 \cdot 10^{-6}\,\frac{Tm}{A}$ [Flö10].
A big advantage of this steerer method over the dipole spectrometer is that it is not relying on the initial transversal beam position (x_0, y_0) - under the assumption of an homogeneous magnetic field. It only depends on the transversal deflection and the initial transversal divergence (x_0', y_0'). With some simple geometrical considerations (x_0', y_0') can be taken into account for the upper fit model.

The law of sine for the geometry shown in fig. 6.4 is defined as

$$\frac{\Delta x}{\sin\delta} = \frac{\overline{\Delta x}}{\sin\bar{\delta}}. \tag{6.2}$$

For the relations between (x_0', x_{St}') and $(\delta, \bar{\delta})$ hold

$$\begin{aligned} \delta &= \frac{\pi}{2} - |x_{St}' + x_0'| - x_0' \\ \bar{\delta} &= \frac{\pi}{2} + |x_{St}' + x_0'|. \end{aligned}$$

This result and the addition and subtraction theorem of sine and cosine (called

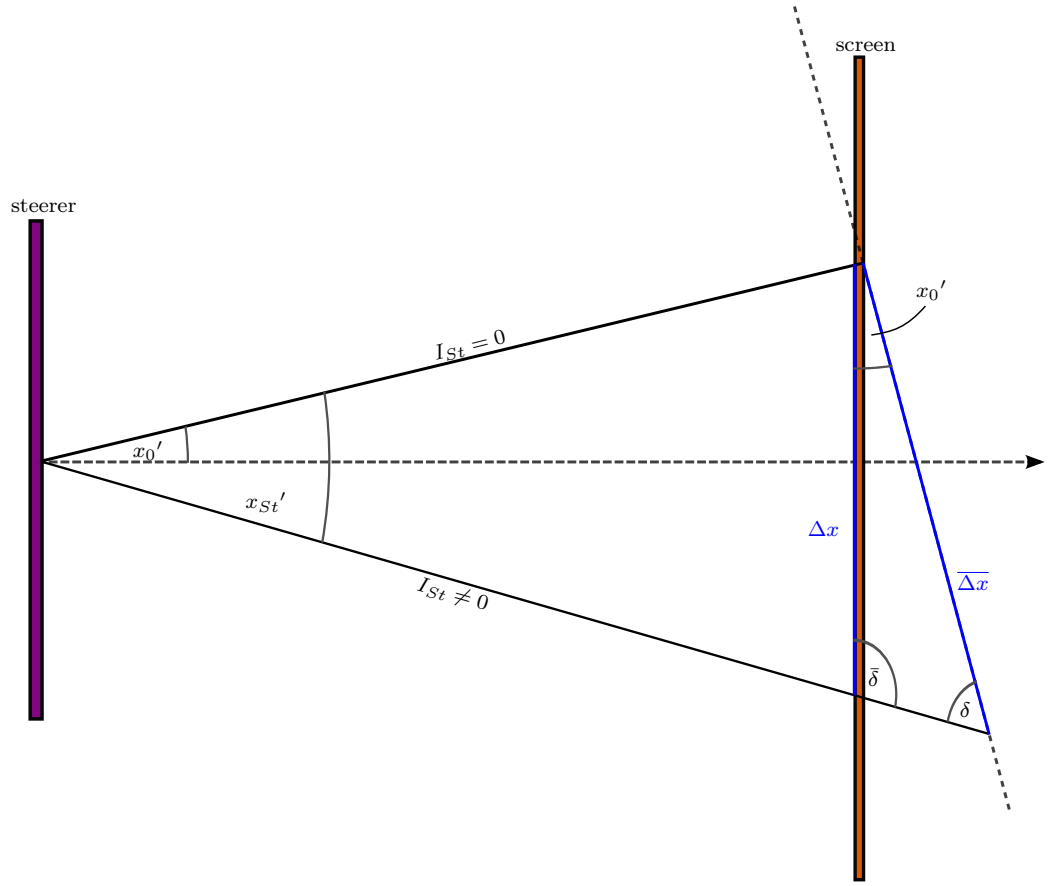

Figure 6.4: Geometry of the deflection of a bunch due to a steerer.

formulæ in the following) allows to find an expression for $\overline{\Delta x}$:

$$\begin{aligned}
\overline{\Delta x} &= \Delta x \frac{\sin \bar{\delta}}{\sin \delta} \\
&= \Delta x \frac{\sin\left(\frac{\pi}{2} + |x_{St}' + x_0'|\right)}{\sin\left(\frac{\pi}{2} - |x_{St}' + x_0'| - x_0'\right)} \\
&\overset{formulæ}{=} \Delta x \frac{\cos\left(|x_{St}' + x_0'|\right)}{\cos\left(|x_{St}' + x_0'|\right)\, \cos x_0' + \sin\left(|x_{St}' + x_0'|\right)\, \sin x_0'} \\
&= \Delta x \frac{1}{\cos x_0' + \tan\left(|x_{St}' + x_0'|\right)\, \sin x_0'}.
\end{aligned} \tag{6.3}$$

Introducing it into 6.1 yields

$$\overline{\Delta x} = \frac{e\, l_D}{p_z}\, Int_{St}(J)$$
$$\Delta x = \frac{e\, l_D}{p_z}\, \left(\cos {x_0}' + \tan\left(|{x_{St}}' + {x_0}'|\right)\, \sin {x_0}'\right)\, Int_{St}(J) \tag{6.4}$$

with ${x_{St}}' = e\, Int_{St}(J)/p_z$ derived from 6.1.
A steerer energy measurement is shown in fig. 6.5. The beam momentum p_z is determined by a linear fit of the steerer current in dependence of the transversal deflection (fig. 6.6). 6.1 has been used for the fitting. 6.4 yields the same result because ${x_0}'$ was too small and hence irrelevant. The steerer scan yields a mean beam energy of (3.202 ± 0.005) MeV. A energy measurement with the spectrometer for the same beam parameters yields 3.200 MeV.
The steerer method is presently limited by the accuracy of the steerer calibration [Flö10]. But in principal it could be a good alternative for the dipole spectrometer - of course just in case of a mean beam energy measurement since the energy spread is not approachable by this method. The dipole spectrometer in contrast is predestined for a energy spread measurement because of its highly dispersive beam dynamic. The energy spread is directly projected on a screen. So the combination of both measurement methods should yield accurate results for the mean beam energy and the beam energy spread.

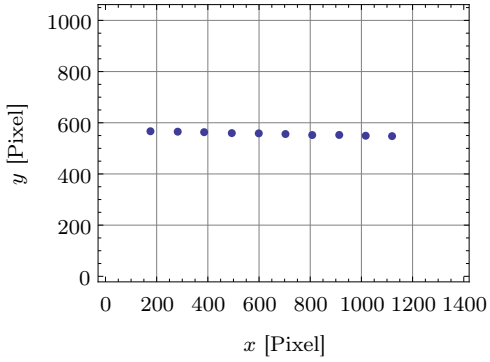

Figure 6.5: Transversal beam position for different steerer currents. For every data point 10 measurements were averaged.

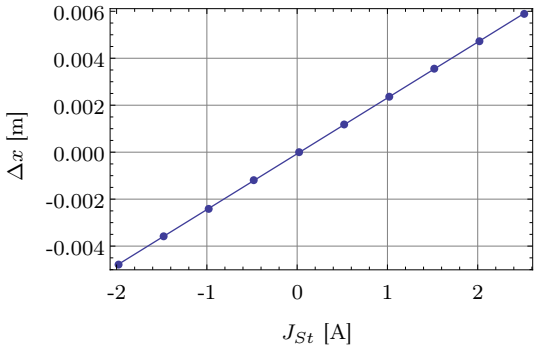

Figure 6.6: Linear fit for steerer current J_{St} against transversal beam deflection Δx.

6.3 Solenoid calibration and numerical tracking

To reflect the behavior of a solenoid its magnetic field map can be used to describe the focus strength, the induced rotation or for numerical tracking algorithms. The latter received better results if the integrated field map is close to the real solenoid field. So the use of measured field maps should be the common way to improve simulations. But the involving problems are much larger as the profit they bring. In the next section the problems of measured field maps and the requirements of theoretical field map improvements are discussed. But first of all the calibration of the REGAE solenoids for further calculations is determined.

6.3.1 Solenoid current calibration for the field integral and field amplitude

To express relations in dependence on the solenoid current it is necessary to find a calibration for the field amplitude and the second field integral F_2 which is proportional to the focusing strength (see sec. 2.3.2). The existing measurements of the magnetic field $B_z(z)$ for the single and double solenoid at REGAE were used for the calibration and are illustrated in fig. 6.7.

So the obtained calibrations for the field amplitudes are

Single solenoid

$$B_{z,max}(I_{sol})\,[\mathrm{T}] = 0.0005 + 0.0212\,I_{sol}\,[\mathrm{A}] \tag{6.5}$$

Double solenoid

$$B_{z,max}(I_{sol})\,[\mathrm{T}] = 0.0005 + 0.0211\,I_{sol}\,[\mathrm{A}] \tag{6.6}$$

This calibration is needed in the context of the single solenoid alignment. For the introduced model in section 2.3.2 the Lenz field parameter B_0 has to be determined. It is defined in dependence on the maximum field amplitude $B_{z,max}$.
The amplitude depends linearly on the current and hence the second field integral $\int {B_z}^2 \mathrm{d}z$ has to depend quadratically on the solenoid current:

Single solenoid

$$F_2(I_{sol})\,[\mathrm{T}^2\,\mathrm{m}] = 0.2 \cdot 10^{-5} + 1.9 \cdot 10^{-5}\,{I_{sol}}^2\,[\mathrm{A}^2] \tag{6.7}$$

Double solenoid

$$F_2(I_{sol})\,[\mathrm{T}^2\,\mathrm{m}] = 0.5 \cdot 10^{-5} + 3.6 \cdot 10^{-5}\,{I_{sol}}^2\,[\mathrm{A}^2] \tag{6.8}$$

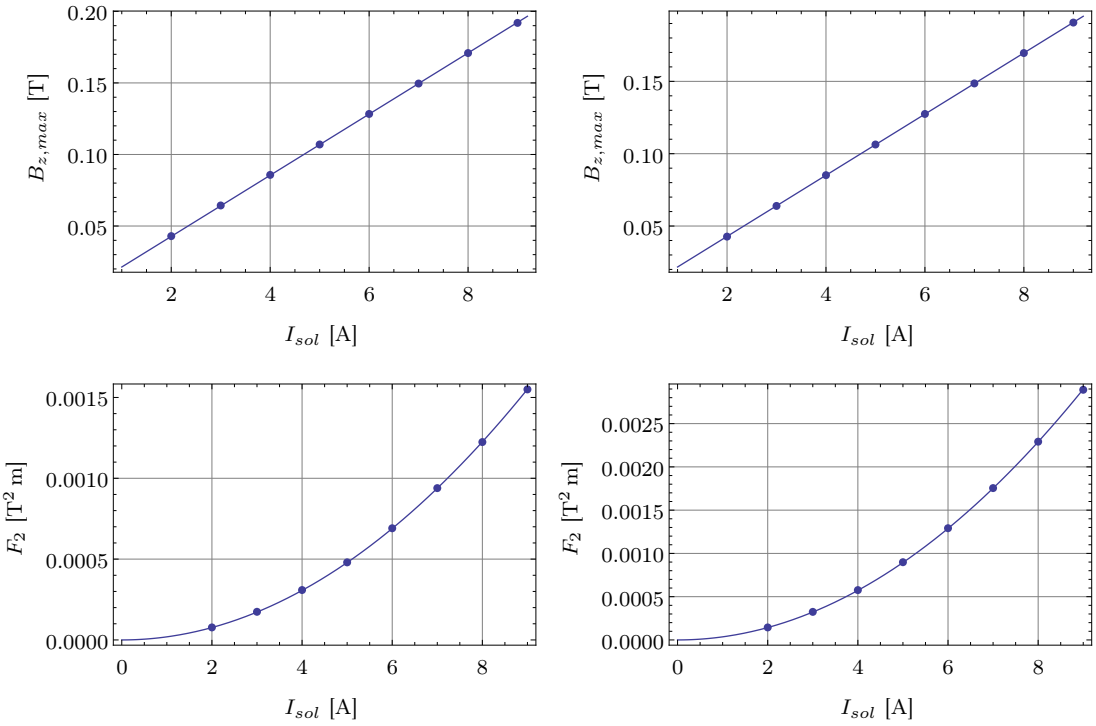

Figure 6.7: Calibration plots for single (left) and double (right) solenoids. Upper row: calibration of the magnetic field amplitude depending on the solenoid current. Lower row: calibration of the second magnetic field integral depending on the solenoid current

F_2 is proportional to the focusing strength of a solenoid which is included in the envelope model for the emittance measurement. This calibration creates the relation between the beam size and the solenoid current.

6.3.2 Numerical emittance growth due to a cut-off of the solenoid field map

In a numerical tracking software like ASTRA an unexpected emittance jump could appear passing a solenoid magnet. The reason for this could be the integrated field map of the solenoid. A "jump" of the magnetic field from zero to a value B_{edge} at the edges of the map results in a numerical emittance growth which has no physical reason. A helpful physical analogue is a cathode in a residual solenoid field. It describes the emitting of electrons inside a solenoid field which leads to an emittance growth as well.
Fig. 6.8 illustrates the problem. Shown is an ASTRA simulation which depicts the development of the emittance of a REGAE bunch with design parameters during its passage through the first solenoid. The emittance doubles for a measured field map and stays mainly constant for a calculated field map. In case of the calculated field map the grid is wider and has a smaller range hence this is no explanation for the observation.

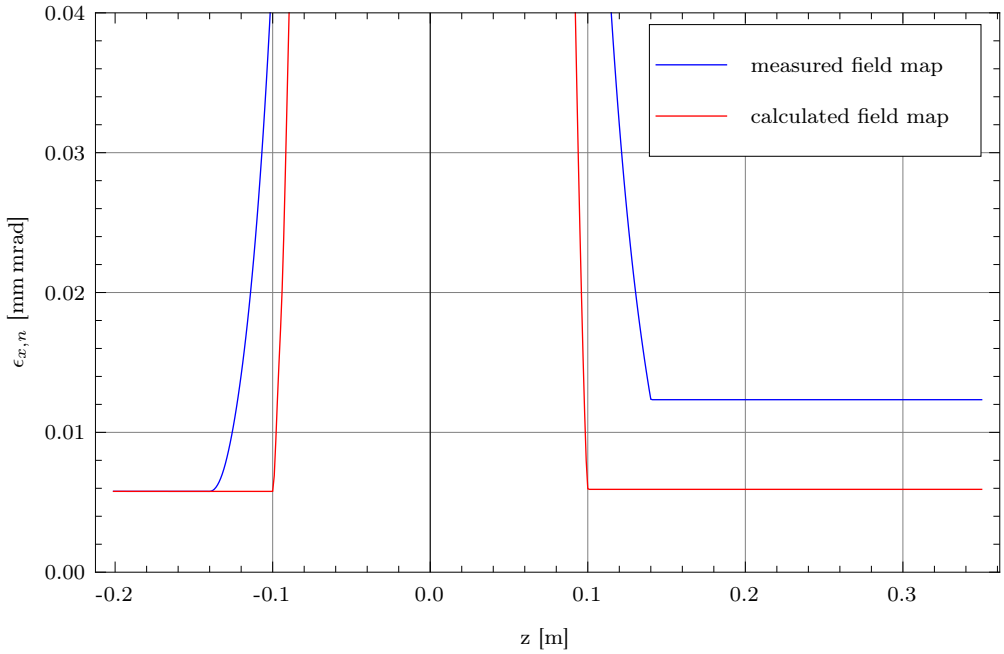

Figure 6.8: Emittance development due to different field maps for an ASTRA simulated 80 fC electron bunch with 5.1 MeV. The center of the solenoid is at $z = 0$. The different ranges of the field maps are reflected in the different starting and ending points of the emittance change.

Theoretical description

The emittance growth has its origin in the solenoid induced rotation. The magnet generates an additional momentum in θ-direction, so that p_x and y as well as p_y and x are coupled. In contrast to the correlation between x and p_x which can be compensated in a two dimensional phase space, it is not possible for a p_x-y correlation. In a 4-dimensional phase space (x, y, p_x, p_y) this would be possible.
Using the rotation equation of motion (2.35), the transformations 2.37 and considering the beam size r as constant, the remaining momentum Δp_θ occurs passing a solenoid with a cut-off of the magnetic field can be written as

$$\begin{aligned} F_\theta = \frac{\mathrm{d}p_\theta}{\mathrm{d}t} &= -q\left(\frac{r\,\dot{z}}{2}\,{B_z}' + \dot{r}\,B_z\right) \\ &= -\frac{q}{2\,r}\,\frac{\mathrm{d}}{\mathrm{d}t}\left(r^2\,B_z\right) \\ \Rightarrow \quad \Delta p_\theta &= -\frac{q}{2\,r}\int_{z_1}^{z_2} r^2\,B_z(z) \\ \Delta p_\theta &= -\frac{q\,r}{2}\left(B_z(z_2) - B_z(z_1)\right). \end{aligned} \tag{6.9}$$

The limits of the integral z_1 and z_2 are the cut-off positions of the field map. In case of a symmetric cut-off of a field map Δp_θ is equal to zero and no additional emittance growth can be observed, while for an asymmetric map $\Delta p_\theta \neq 0$ holds. The condition of a constant r is in general not fulfilled for low energy beams. For a varying radius the integral cannot be analytically solved and Δp_θ will not be equal to zero even in case of a symmetric cut-off.
In the presence of a solenoid field the transversal momentum $\tilde{p}_x$ consists of three components: the uncorrelated momentum $p_{x,0}$, a x-correlated momentum $p^x_{x,c}$ and the former mentioned y-correlated momentum $p^y_{x,c}$. The sum of all three builds up the transversal momentum

$$\tilde{p}_x = p^0_x + p^x_x + p^y_x. \tag{6.10}$$

Because only linear forces are assumed the correlated momenta can be expressed as

$$p^a_x = m^a\,a \qquad \text{with} \quad a = x, y \quad \text{and} \quad m = \text{const.} \tag{6.11}$$

This allows us to formulate correlation terms:

$$\begin{aligned}
\langle p_x^0\, b\rangle &= 0 \qquad \text{with} \quad b = x, y, p_x^x, p_x^y \\
\langle p_x^x\, p_x^y\rangle &= m^x\, m^y\, \langle x\, y\rangle = 0 \\
\langle x\, p_x^y\rangle &= m^y\, \langle x\, y\rangle = 0 \\
\langle x\, p_x^x\rangle^2 &= \langle x^2\rangle\, \langle (p_x^x)^2\rangle = (m^x)^2\, \langle x^2\rangle^2.
\end{aligned} \tag{6.12}$$

The additional emittance term can be obtained by inserting 6.10 into the emittance formula 2.10 what results in

$$\begin{aligned}
{\epsilon_x}^2 &= \frac{1}{(m_0\, c)^2}\left[\langle x^2\rangle\, \langle \tilde{p}_x^2\rangle - \langle x\, \tilde{p}_x\rangle^2\right] \\
&= \frac{1}{(m_0\, c)^2}\left[\langle x^2\rangle\, \langle (p_x^0 + p_x^x + p_x^y)^2\rangle - \langle x\, (p_x^0 + p_x^x + p_x^y)\rangle^2\right] \\
&\overset{6.12}{=} \frac{1}{(m_0\, c)^2}\left[\langle x^2\rangle\, \langle (p_x^0)^2\rangle + \langle x^2\rangle\, \langle (p_x^y)^2\rangle\right] \\
&= {\epsilon_{0,x}}^2 + {\Delta\epsilon_x}^2 \qquad (6.13) \\
\Rightarrow {\Delta\epsilon_x}^2 &= \frac{1}{(m_0\, c)^2}\, \langle x^2\rangle\, \langle (p_x^y)^2\rangle. \qquad (6.14)
\end{aligned}$$

p_x^y can be replaced by Δp_θ which can be split up into Cartesian components

$$\begin{aligned}
p_x &= -\Delta p_\theta\, \sin\theta = -\Delta p_\theta\, \frac{y}{r} \\
p_y &= -\Delta p_\theta\, \cos\theta = -\Delta p_\theta\, \frac{x}{r}.
\end{aligned} \tag{6.15}$$

Therefore the correlated momentum p_x^y writes as

$$\begin{aligned}
p_x^y &= -\Delta p_\theta\, \frac{y}{r} \\
&= \frac{q\, (B_z(z_2) - B_z(z_1))}{2}\, y.
\end{aligned} \tag{6.16}$$

With the assumption of a round beam ($\langle x^2\rangle = \langle y^2\rangle$) the correlated emittance growth yields

$$\begin{aligned}
\Delta\epsilon_x &= \frac{q\, (B_z(z_2) - B_z(z_1))}{2\, m_0\, c}\, \langle x^2\rangle^2 \\
&= \frac{q\, (B_z(z_2) - B_z(z_1))}{2\, m_0\, c}\, {x_{rms}}^2.
\end{aligned} \tag{6.17}$$

As long as Δp_θ is equal to zero $\Delta\epsilon_x$ vanishes what describes the normal case of a charged particle passing a solenoid.

Single solenoid simulations

Fig. 6.9 shows an example for the emittance growth due to a cut-off of a field map. It illustrates a high energy bunch ($E_{kin} = 1\,\mathrm{GeV}$) passing a single solenoid (see section 6.4.1). The simulation is done with ASTRA. The incoming bunch has zero emittance and because of the high energy the beam size can be taken as constant so that 6.17 holds. The ASTRA readout yields an emittance growth of $\Delta\epsilon_{x,n} = 1.47 \cdot 10^{-2}\,\mathrm{mm\,mrad}$. The beam size is $x_{rms} = 0.2\,\mathrm{mm}$. That causes the following result for the theoretical calculation of $\Delta\epsilon_{n,x}$:

$$\Delta\epsilon_{n,x} = 1.48 \cdot 10^{-2}\,\mathrm{mm\,mrad}.$$

The simulation of a REGAE bunch with design parameters in ASTRA (fig. 6.8) yields an emittance growth from $5.8 \cdot 10^{-3}\,\mathrm{mm\,mrad}$ to $12.3 \cdot 10^{-3}\,\mathrm{mm\,mrad}$ which corresponds to $\Delta\epsilon_{n,x} = 0.0065\,\mathrm{mm\,mrad}$. In this case 6.17 yields only

$$\Delta\epsilon_{n,x} = 0.0047\,\mathrm{mm\,mrad}.$$

The difference is owed the fact of a non-constant beam size. Furthermore notice that this emittance growth even occurs for a longitudinal larger map with a smaller grid compared to the calculated field map (see fig. 6.8). Nevertheless it is possible to describe and understand the reasons for this kind of numerical emittance growth.

To avoid emittance growth in simulations theoretical field maps fulfilling the boundary conditions of the magnetic field should be included. The boundary conditions are

$$B_z(z_1) = B_z(z_2) = 0$$
$$B_z(z_1)' = B_z(z_2)' = 0.$$

A smaller grid width of the field map improves the numerical calculation of field integrals and derivations of the magnetic field.

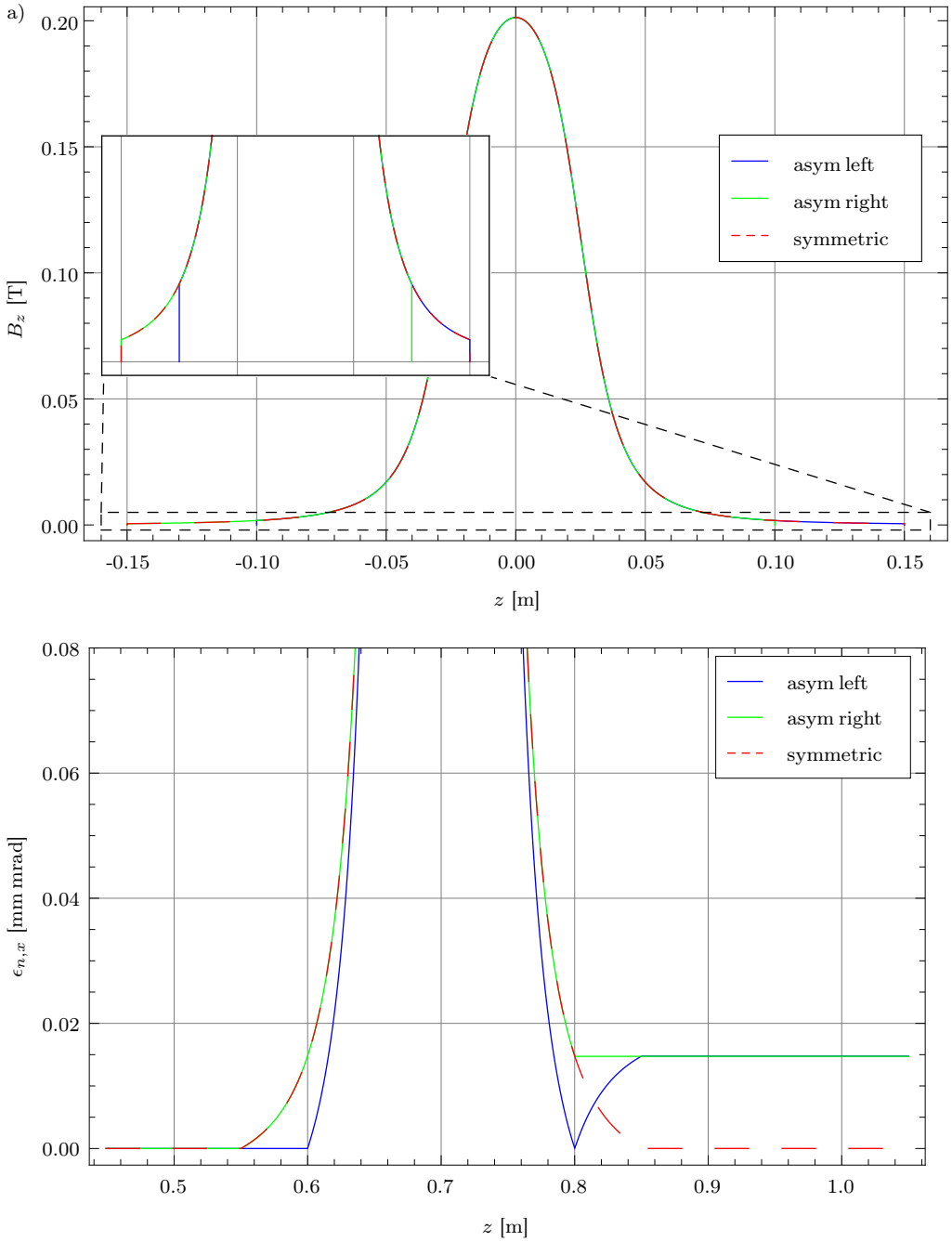

Figure 6.9: a) The asymmetric and symmetric field maps with zoom onto the field edges. b) Local emittance growth due to the upper field maps. For asymmetric field maps the emittance does not get back to zero.

6.4 Solenoid alignment

In the following only principal procedures for the alignment of the REGAE solenoids will be described. During the course of this diploma thesis the solenoid alignment itself was just in some parts possible due to lack of machine time.
At REGAE three solenoids are installed. All are prealigned by the DESY alignment group and should be adjusted with a precision of $100\,\mu m$.
A big challenge was the earth's magnetic field. The REGAE beam line is north-south aligned so in large part the horizontal magnetic field component coincides with the acceleration direction and hence it has no effect on the electron beam. But there is still a vertical field component in the range of $30\,\mu$T. This static field deflects the beam in dependence on the beam energy which has to be reduced in case of the single solenoid alignment in order to get the electron beam on the screen behind the single solenoid. But this results in an even larger deflection of the beam. The correction with steerers is only locally possible, thus a large compensation coil has had to be installed to reduce the effect of the earth's magnetic field [Geh12]. Its performance has been demonstrated so that a precise alignment of the solenoid is possible in nearest future.

6.4.1 Single solenoid

The first solenoid right downstream of the gun (fig. 5.1) is the only single solenoid. The analytical model of the solenoid has been derived in section 2.3. Equation 2.56 describes the trajectory through this kind of solenoid. With 2.62 an analytical model for the beam trajectory including offsets and tilts is given. The measurement itself follows the same scheme as the measurement for the beam energy estimation with a steerer: recording the beam position on a screen while changing the solenoid current. A different magnetic field results in a different beam trajectory which yields a different beam position. The illustrated measurement below (fig. 6.10) was recorded before the compensation coil has been installed. The measurement shows that the model for a misaligned solenoid works.
The misalignment parameters were determined as

$$x_{\text{off}} \approx y_{\text{off}} \approx 1\,\text{mm} \qquad\qquad x_{\text{tilt}} \approx y_{\text{tilt}} \approx 10\,\text{mrad}$$

as a consequence of the earth's magnetic field and the low beam energy which is required to align the single solenoid.
Because a calculation of uncertainties is very complicated for a complex model function like 2.62, the errors are estimated. Changing the fitted parameters slightly

an upper and lower limit for the errors is given. A plausible estimation is shown in fig. 6.11. The errors are estimated to be in the range of 100 μm and 200 μrad. The conclusion is: the misalignment parameters of a single solenoid can be determined by this method. It needs more investigation to confirm and improve the accuracy of the procedure.

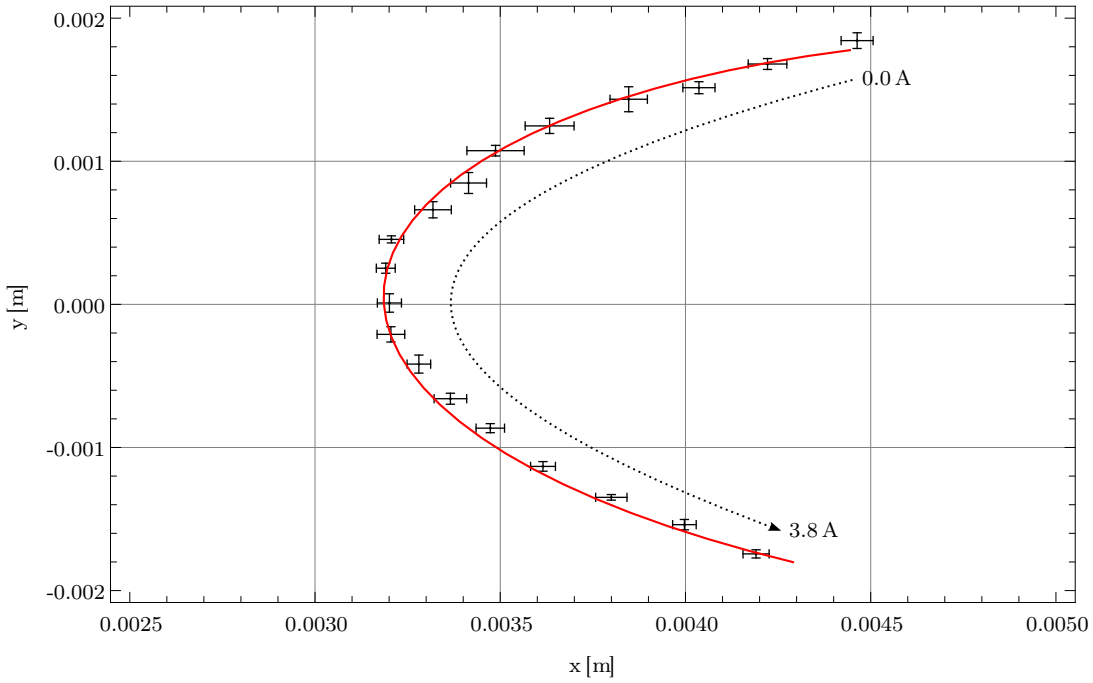

Figure 6.10: Fit to determine the offset and tilt of the single solenoid at REGAE.

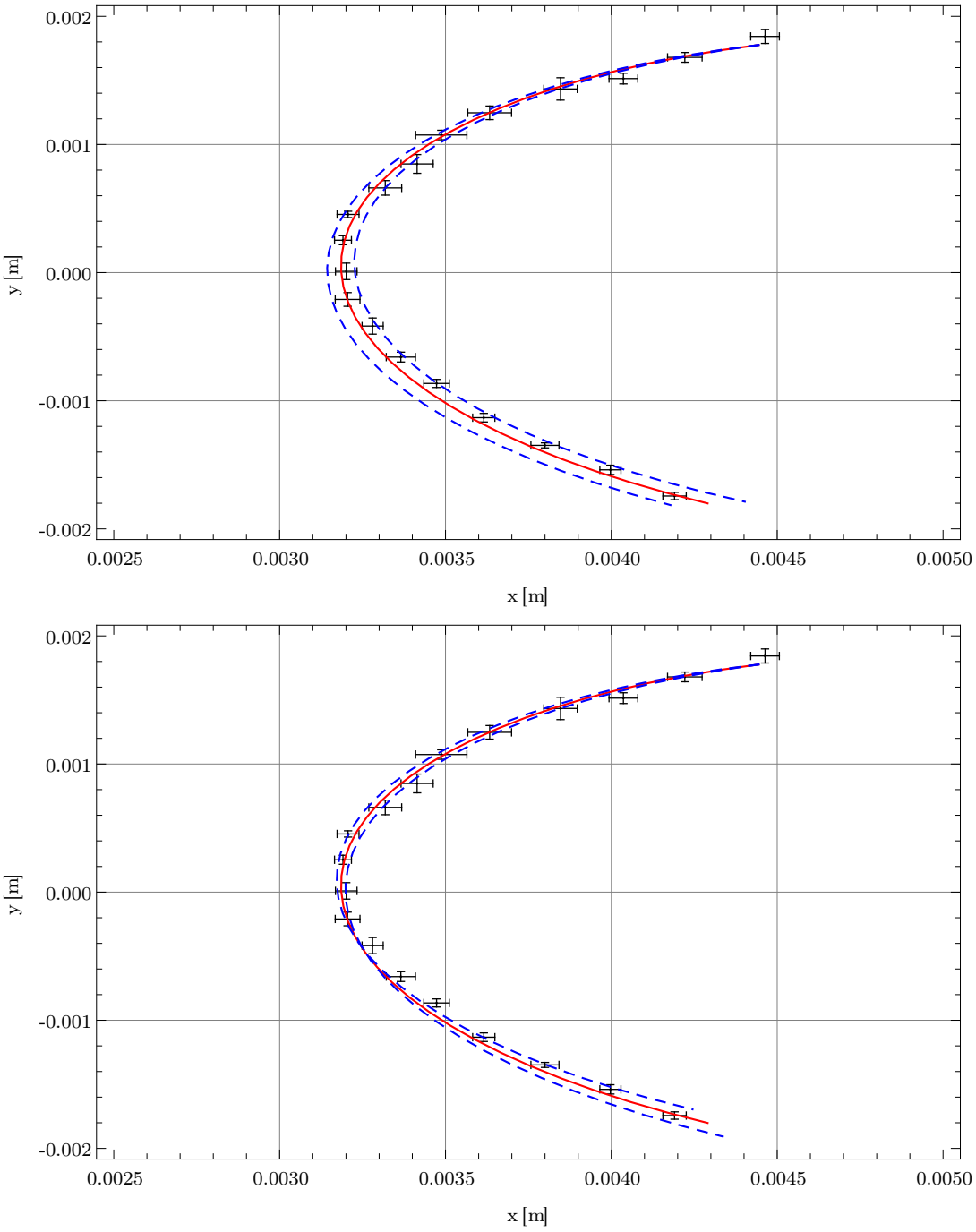

Figure 6.11: Solenoid model with fitted parameters (continuous line) and model with slightly different offset (upper plot) and tilt (lower plot) parameters (dashed line).

6.4.2 Double solenoid

A double solenoid at REGAE can be thought of as two connected single solenoids. But the magnetic fields are of opposite direction. As a consequence the Larmor angle - defined in 2.38 - is zero.
If we assume a constant beam size in the vicinity of the solenoid it is also possible to handle it as a thin lens. Therefore the trajectory of the center of mass of the beam can be easily described as

$$\begin{pmatrix} x \\ x' \end{pmatrix} = \mathbf{M}_{\text{drift}} \cdot \mathbf{M}_{\text{thin}} \cdot \begin{pmatrix} x_0 \\ x_0{}' \end{pmatrix}$$
$$\Rightarrow \quad x = -\frac{l_{\text{drift}}\, x_0}{f_{\text{thin}}(I_{\text{sol}})} \tag{6.18}$$

where f_{thin} is the focal length of the solenoid which depends quadratically of the solenoid current I_{sol} (6.8). This model can be used to describe the deflection of the beam and the resulting transversal beam motion on a detection screen. The measured data and the fit of a measurement of Sol45 (see fig. 5.1) are depicted in fig. 6.12. A comparison between the beam deflection due to the solenoid current before and after the alignment is shown in fig. 6.13.

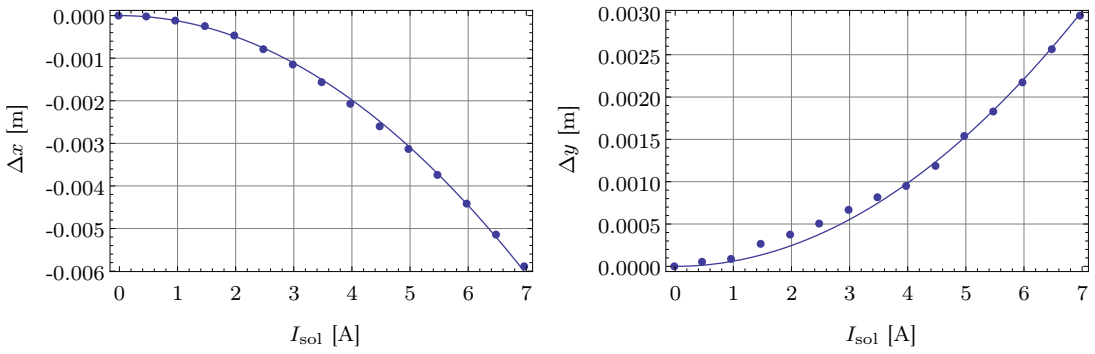

Figure 6.12: Alignment fits for Sol45 in x- and y-direction

The results of the fits are:

$$x_0 = (6.14 \pm 0.03)\,\text{mm}$$
$$y_0 = (-3.05 \pm 0.04)\,\text{mm}$$

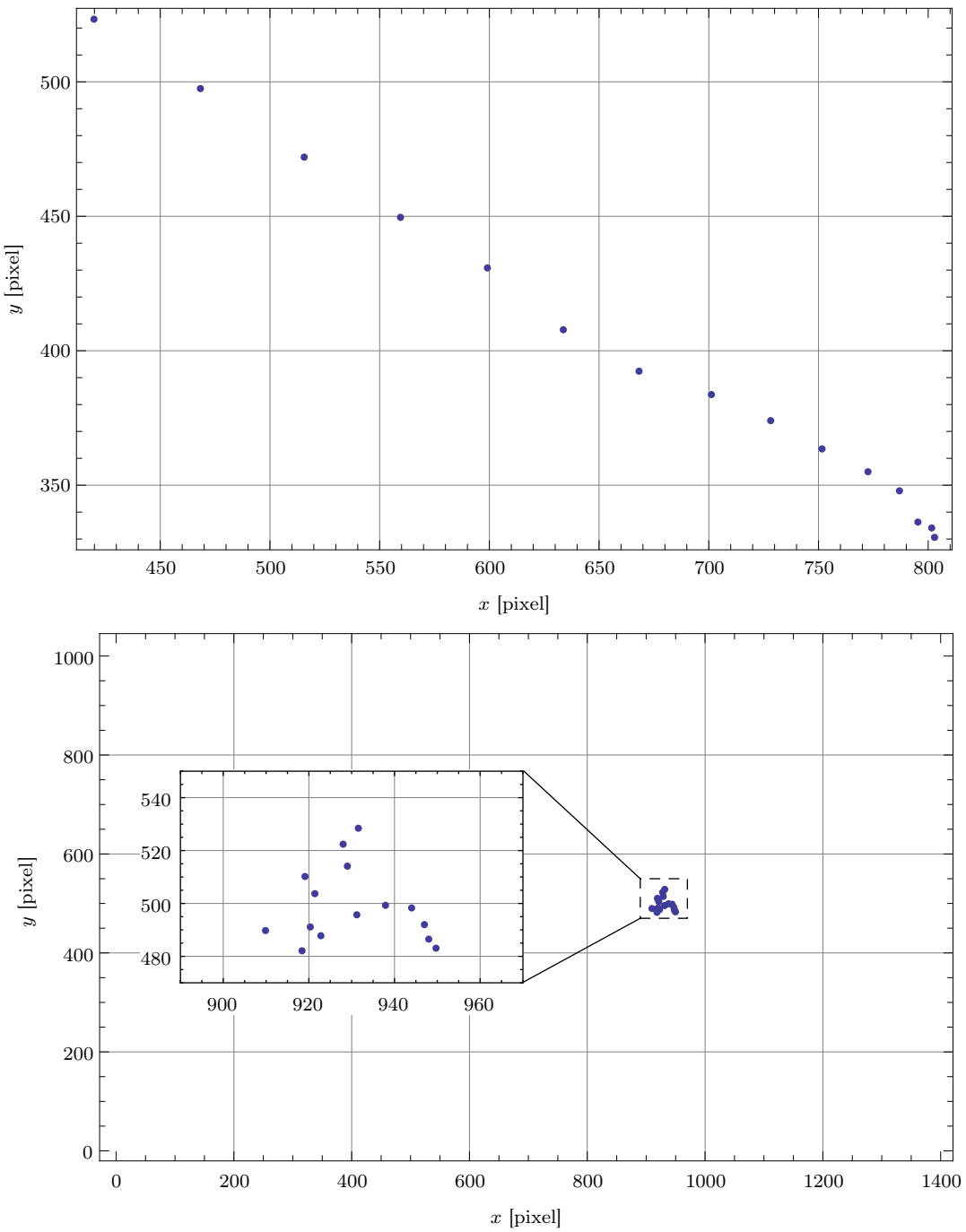

Figure 6.13: Sol45 scan on target screen before (upper) and after (lower) alignment.

with statistical errors obtained by the fit. The large offsets are due to the earth's magnetic field which acts over a free drift of $\sim 4\,\mathrm{m}$ before Sol45. The solenoid has been moved about 5.9 mm in x-direction and the measurement has been redone. Instead of a deflection in positive x-direction the beam moved slightly in negative direction after the alignment. The remaining horizontal and vertical offset were corrected with the steerers behind the buncher (see fig. 5.1) only since an accurate alignment was not possible without compensation of the earth's magnetic field. The third solenoid was aligned because this one is the favorite for an emittance measurement on detector. Without this alignment it is not possible to focus the beam on it. Even a small divergence generated by the solenoid causes a huge transversal deflection at the position of the detector so that a change in the focusing strength could result in the loss of the beam.
In section 3.1.2 a way to approximate the beam dynamical abilities of a double solenoid with higher accuracy has been introduced. It is called the double thin lens approximation. Instead of considering a double solenoid as one thin lens a pair of thin lenses describes the beam dynamic more effectively. In case of the solenoid alignment the normal thin lens approximation has been applied. The double thin lens could be used to determine, beside the offset, the tilt of a double solenoid.

7

Emittance measurements

In this section two measurements, the first (19th of September) was taken with the first gun installed at REGAE, the second (12th of October) was taken after gun and incoupling mirror were exchanged are presented. The principal measurement proceeds as described in section 3. To fit these measurements the analytical fit method from section 3.2.1 and a numerical fit based on the space charge model from section 3.1.2 have been used. The correction of a possible beam tilt is done by rotating the whole coordinate system (see sec. 3.1.3). In these new coordinates an improved determination of the emittance is possible. But first of all an uncorrected measurement is shown in fig. 7.1 (upper plot). Besides data points the fit curves of both transversal directions are included. The results of the analytical and numerical fit with space charge are depicted in tab. 7.1 (upper table). Note that errors are calculated without considering the covariance, because it is presently not possible to measure the beam size, the solenoid current and all other magnet currents or RF signals with the required temporal synchronization. And hence a correlation e.g. between the solenoid current jitter and the beam size jitter cannot be noticed. This fact increases the errors so that the indicated errors are the upper limit of the statistical error. In addition a systematical error caused by the signal evaluation algorithm has to be taken into account (see sec. 4.2). It is proportional to the absolute beam rms value. The statistical as well as the systematic beam size errors are considered in fig. 7.1 and 7.2. They are depicted as vertical error bars. Another error which has to be considered for the calculations is the systematic error of the mean beam energy measurement (see sec. 6.2.1). The mean beam

energy has been measured to be

$$E_{\mathrm{kin}} = 3.64 \pm 0.04\,\mathrm{MeV}.$$

The charge was determined to be 1.15 pC. Effects by the space charge are expected like demonstrated in section 3.1.2.

A rotation corrected measurement is shown in fig. 7.1 (lower plot) and the results of the fits can be looked up in tab. 7.1 (lower table). The emittances differs only slightly from the uncorrected results. It is a consequence of the large emittance which dominates the beam envelope in the beam line section of the measurement. This overwhelming contribution to the beam envelope leads to vanishingly low space charge effects.

The large emittance could be a reason of unfavorably chosen laser properties on the photo cathode. A large laser spot yields a large thermal emittance while a too small laser spot increase the space charge effects at the cathode. A trade-off for the laser spot size has to be found in order to optimize the initial emittance. Another reason could be the low mean beam energy which corresponds to a small field gradient inside the gun. A higher gradient would reduce space charge effects. The second measurement with the new gun and incoupling mirror yields better results. The emittance product is 2.4 times smaller. The beam was extremely stable what is noticeable by the small errors of the beam size measurement in fig. 7.2. The mean beam energy was 2.65 ± 0.03 MeV with a bunch charge of 1.05 pC.

The relatively large $\tilde{\chi}_y^2$ for the second measurement is caused by the initial conditions. The source size $y_{0,rms}$ is already small at the position of Sol45 and cannot be reduced anymore. This explains the flat trend of the red curve of fig. 7.2. Even small deviations from the theoretical model obtains in combination with the small errors a large contribution to the χ^2-calculation and yields finally a large $\tilde{\chi}_y^2$.

Another reason for the deviation between the theoretical model and the measured data could be an unfortunate position of the beam on the detector screen. If the beam lies at the edge of the screen, the signal evaluation algorithm (see chap. 4) can cause a systematic error which would explain the deviation and the small error bars.

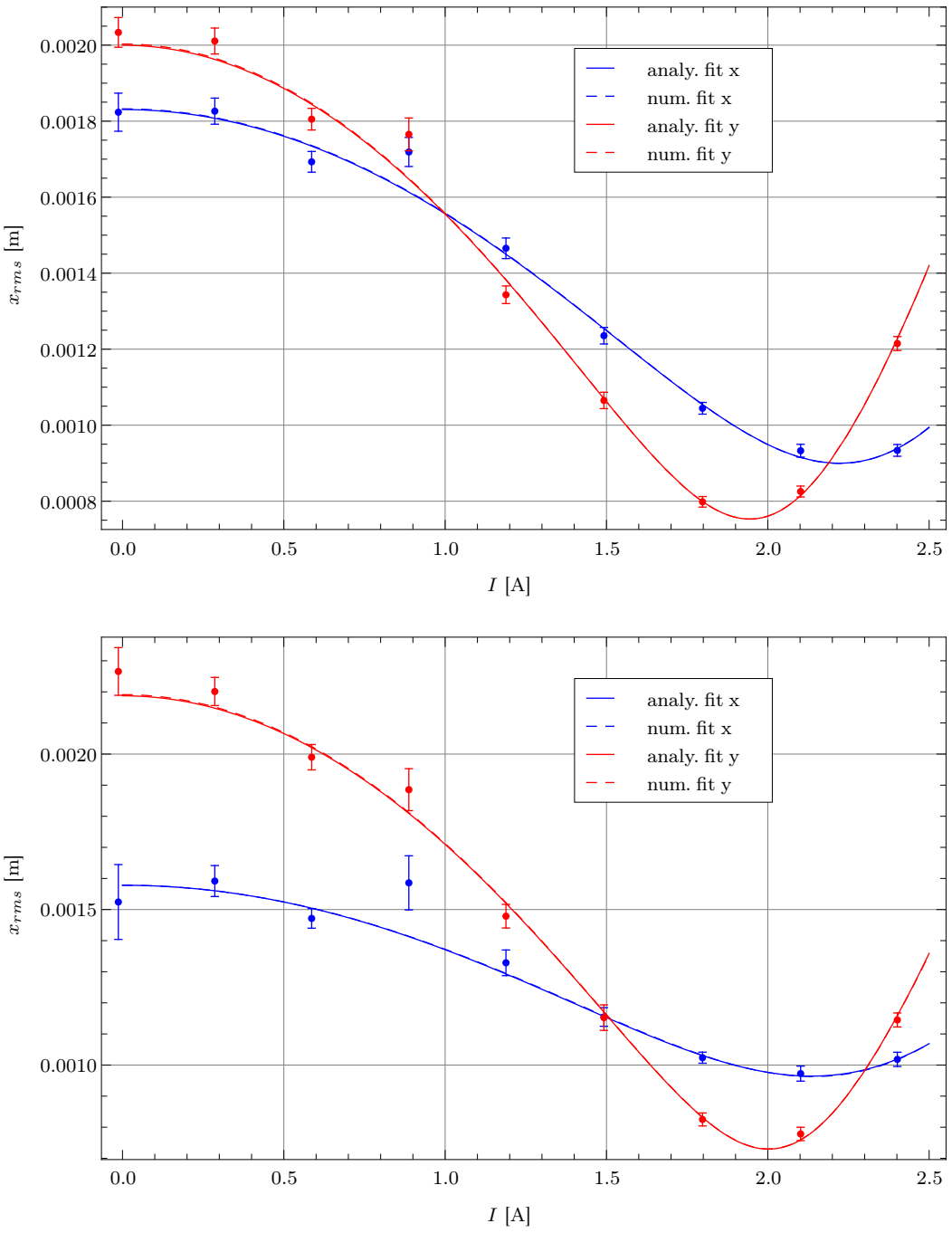

Figure 7.1: Solenoid scan data and emittance fit for x and y (measured on 19th of September). Upper figure without tilt correction. Lower figure represents the same calculation in a $\theta = 70.5°$ rotated Cartesian coordinate system.

Table 7.1: Fitted parameters for an analytical fit and a numerical fit considering the space charge model (measured on 19th of September). Upper table without rotation correction. Lower table represents the same calculation in a $\theta = 70.5°$ rotated Cartesian coordinate system.

Parameter	**Analy. fit**	**Num. fit (space charge)**
$x_{0,rms}$ [m]	$(1.5 \pm 1.8) \cdot 10^{-3}$	$1.5 \cdot 10^{-3}$
$(x_{0,rms})'$ [rad]	$(2.5 \pm 1.9) \cdot 10^{-5}$	$2.2 \cdot 10^{-5}$
$\epsilon_{n,x}$ [mm mrad]	2.4 ± 0.1	2.4
P	-	$8.9 \cdot 10^{-9}$
$\tilde{\chi}_x^2$	2.2	3.2
$y_{0,rms}$ [m]	$(2.3 \pm 0.6) \cdot 10^{-3}$	$2.3 \cdot 10^{-3}$
$(y_{0,rms})'$ [rad]	$(-8.6 \pm 1.2) \cdot 10^{-5}$	$-9.0 \cdot 10^{-5}$
$\epsilon_{n,y}$ [mm mrad]	3.1 ± 0.3	3.1
P	-	$3.8 \cdot 10^{-8}$
$\tilde{\chi}_y^2$	2.6	3.9
$\epsilon_{n,x} \cdot \epsilon_{n,y}$ [(mm mrad)^2]	7.4	7.4

Parameter	**Analy. fit**	**Num. fit (space charge)**
$x_{0,rms}$ [m]	$(1.2 \pm 2.7) \cdot 10^{-3}$	$1.3 \cdot 10^{-3}$
$(x_{0,rms})'$ [rad]	$(-2 \pm 22) \cdot 10^{-6}$	$-3.0 \cdot 10^{-6}$
$\epsilon_{n,x}$ [mm mrad]	2.2 ± 0.1	2.2
P	-	$9.3 \cdot 10^{-9}$
$\tilde{\chi}_x^2$	1.1	1.7
$y_{0,rms}$ [m]	$(2.4 \pm 2.0) \cdot 10^{-3}$	$2.4 \cdot 10^{-3}$
$(y_{0,rms})'$ [rad]	$(-6.5 \pm 1.4) \cdot 10^{-5}$	$-6.9 \cdot 10^{-5}$
$\epsilon_{n,y}$ [mm mrad]	3.1 ± 0.3	3.1
P	-	$1.3 \cdot 10^{-8}$
$\tilde{\chi}_y^2$	1.2	1.7
$\epsilon_{n,x} \cdot \epsilon_{n,y}$ [(mm mrad)^2]	6.8	6.8

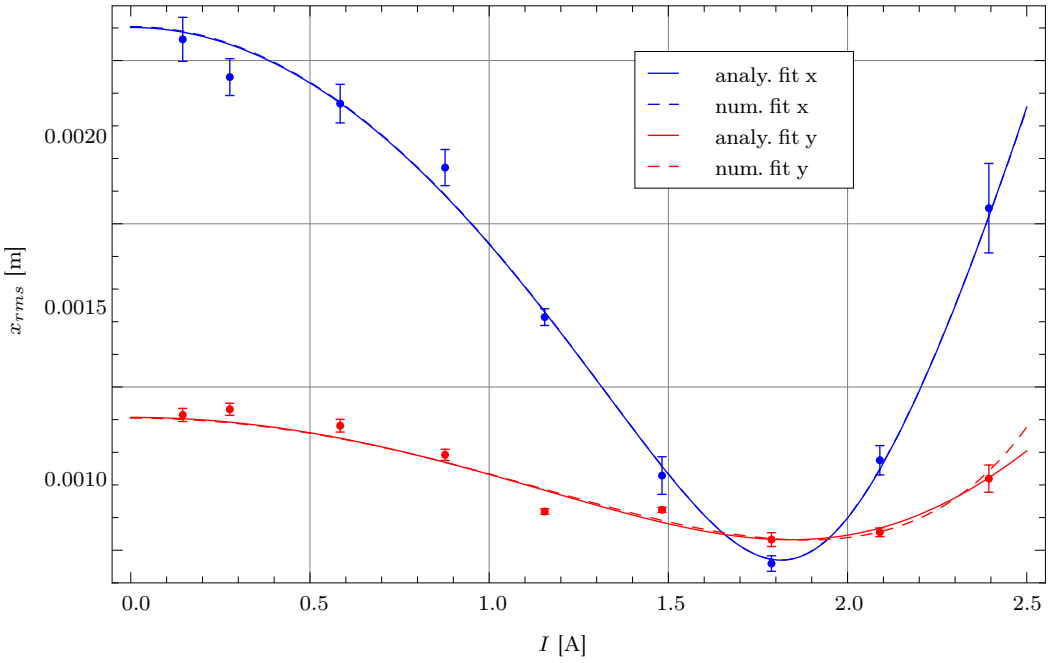

Figure 7.2: Rotation corrected solenoid scan data and emittance fit for x and y (measured on 12th of October).

Table 7.2: Fitted parameters for an analytical fit and a numerical fit considering space charge model with rotation correction ($\theta = -15.1°$) (measured on 12th of October).

Parameter	**Analy. fit**	**Num. fit (space charge)**
$x_{0,rms}$ [m]	$(2.0 \pm 0.3) \cdot 10^{-3}$	$2.0 \cdot 10^{-3}$
$(x_{0,rms})'$ [rad]	$(1.2 \pm 0.2) \cdot 10^{-4}$	$1.1 \cdot 10^{-4}$
$\epsilon_{n,x}$ [mm mrad]	2.6 ± 0.3	2.6
P	-	$8.5 \cdot 10^{-9}$
$\tilde{\chi}^2_x$	1.3	2.0
$y_{0,rms}$ [m]	$(7.6 \pm 2.6) \cdot 10^{-4}$	$7.5 \cdot 10^{-4}$
$(y_{0,rms})'$ [rad]	$(4.9 \pm 1.6) \cdot 10^{-5}$	$4.6 \cdot 10^{-5}$
$\epsilon_{n,y}$ [mm mrad]	1.06 ± 0.03	1.05
P	-	$6.3 \cdot 10^{-9}$
$\tilde{\chi}^2_y$	13.3	19.5
$\epsilon_{n,x} \cdot \epsilon_{n,y}$ [(mm mrad)^2]	2.8	2.7

8

Conclusion and outlook

What has been reached in this diploma thesis and what tasks remains for the future? Most of the aims could be fulfilled. Beam based alignment procedures for different magnetic lenses has been developed and partly tested. The same applies to the emittance measurement. It was possible to measure the transverse emittance. The experimental procedure works fine and with help of the theoretical models and the analytical as well as numerical fitting routines a reasonable emittance could be measured. In order to simplify the measurement procedure it would be useful to have a "one-klick" tool which performs the emittance measurement and evaluates it afterwards. This is under developing and not ready yet for operating.
Especially the theoretical description of the trajectory of a charged particle through a single solenoid and the development of a space charge envelope model for electron bunches was successful. The trajectory description could be cross checked in the context of a single solenoid beam based alignment measurement. The space charge model shows a good coincidence with simulations. Unfortunately the beam at the considered beam line section was emittance dominated and hence space charge effects were vanishingly low. So the accordance with experimental data has to be proved.
For the evaluation of the beam based alignment measurement of a single solenoid as well as for the emittance calculations with the space charge model a numerical fitting routine was necessary. It has been developed by myself and yields good results for both cases. It is useful in every case where analytical methods fail.
An important task for the future is a more precise emittance measurement under better machine conditions. The lower limit of the transverse emittance is set at

the photo cathode right after a bunch is emitted. A transversal smaller laser pulse and a higher field gradient inside the gun would improve the emittance. If design parameters are assumed, an emittance measurement is much more challenging. As shown measurements are only possible for certain machine parameters (see section 5.2). An even higher precision can be achieved by a synchronized data acquisition which would allow to correlate the data. With the covariance error propagation it is possible to reduce the errors caused by correlated values like the beam size and the solenoid current. If these correlations are considered a high precision emittance measurement is achievable.
Another important issue is the discussed mean beam energy measurement with a steerer. It has the potential to become an easy and highly accurate procedure but requires a better calibration of the steerer magnets.

Bibliography

[Bev69] Philip R. Bevington. *Data reduction and error analysis for the physical sciences*. McGraw-Hill book company, 1969.

[Buo90] J. Buon. Beam phase space and emittance. In S. Turner, editor, *CERN accelerator school*, volume 91-04. CERN, 1990.

[Com94] Michele Comunian. *Emittance Measurements in Compact Linear Collider Test Facility*. Draft version of the phd thesis, Università degli studi di Padova, 1994.

[DH12] Hossein Delsim-Hashemi. Imaging detector for relativistic-electron-microscope regae. Technical report, DESY, 2012. Draft Version 15.10.2012.

[DHE+06] Jason R. Dwyer, Christoph T. Hebeisen, Ralph Ernstorf, Maher Harb, Vatche B. Deyirmenjian, Robert E. Jordan, and R. J Dwayne Miller. Femtosecond electron diffraction: 'making the molecular movie'. *Philosophical Transactions of the royal society*, 364:741–778, January 2006.

[Flö10] Klaus Flöttmann. Design and performance of printed circuit steering magnets for the flash injector. In *IPAC'10, Kyoto, Japan*, 2010.

[Flö11a] Klaus Flöttmann. *ASTRA - A Space Charge Tracking Algorithm*, 3 edition, October 2011.

[Flö11b] Klaus Flöttmann. Beam dynamics in RF guns and injectors. Draft Version 25.01.2011, January 2011.

[Geh12] Tim Gehrke. In preperation. Master's thesis, Universität Hamburg, 2012.

[HK96] P. W. Hawkes and E. Kasper. *Principles of Electron Optics*, volume 1: Basic Geometrical Optics. ACADEMIC PRESS, INC., 1996.

[Jol05] Simon Jolly. Focusing properties of a solenoid magnet. UK Neutrino Factory R&D at Imperial College meeting, May 2005.

[Len51] Friedrich Lenz. Berechnung der elektronenoptischen Kenngrößen eines speziellen magnetischen Linsenfeldes ohne numerische Bahnintegrationen. *Annalen der Physik*, 444, Issue 5:245–258, 1951.

[Löh05] Florian Löhl. Measurements of the transverse emittance at the VUV-FEL. Diploma thesis, Universität Hamburg, 2005.

[Lio38] Joseph Liouville. Sur la théorie des Êquations transcendantes. *Journal de Mathématiques Pures et Appliquées*, 3:337–354, 1838.

[MZ03] M.G. Minty and F. Zimmermann. *Measurements and Control of Charged Particle Beams*. Springer-Verlag Berlin Heidelberg New York, 2003.

[Nav06] Gerhard Navratil. Ausgleichrsrechung - Die Anwendung statistischer Methoden in Vermessungswesen und GIS. Ein Skriptum zu den Lehrveranstaltungen Ausgleichungsrechnung I + II, Institut für Geoinformation und Kartographie, Dezember 2006.

[RS92] J. Rossbach and P. Schmüser. Basic course on accelerator optics. `adweb.desy.de/~rossbach/uni/Cern.pdf`, 1992.

[RSW82] G. Ripken, K. Steffen, and A. Wrulich. Thin magnet matrix representation of a solenoid. DESY M-VM 82/15, DESY, 1982.

[Sac70] Frank J. Sacherer. RMS envelope equations with space charge. In *4th IEEE Particle Accelerator Conference, Chicago, IL, USA, 1-3 Mar 1971*, pages 1105–1107, 1970.

[WR88] F. Willeke and G. Ripken. Methods of beam optics. Desy 88-114, DESY, 1988.

Acknowledgments

Firstly I would like to thank Klaus Flöttmann, my supervisor, who gave me the opportunity to develop this diploma thesis at REGAE and helped me with words and deeds.
In addition I owe thanks to Frank Mayet who spend a lot of time to discuss ideas and supported me to accomplish my measurements.
Furthermore I would like to thank the whole REGAE team and the MSK DESY group keeping the machine running during my beam time. Especially I would like to mention Hossein Delsim-Hashemi and Shima Bayesteh for their work on the diagnostics and Dongfang Zhang for his help concerning all kind of laser subjects.

Erklärung

Hiermit versichere ich, dass ich die vorliegende Arbeit selbstständig und nur unter der Verwendung der angegebenen Quellen und Hilfsmittel verfasst habe.
Ferner bin ich mit der Ausleihe meiner Arbeit einverstanden.

Hamburg, den 17. Mai 2012

Max Hachmann